This is to certify that the

dissertation entitled

BOYCE MILTON HUMPHRIES

presented by

A STUDY OF MASSIVE ELECTRON
PAIRS AND ASSOCIATED PARTICLES
PRODUCED AT THE CERN ISR

has been accepted towards fulfillment
of the requirements for

Ph.D degree in Physics & Astron.

Bernard G Pope
Major professor

Date 13 May 1991

A STUDY OF MASSIVE ELECTRON PAIRS AND ASSOCIATED PARTICLES PRODUCED AT THE CERN ISR

By

Boyce Milton Humphries

A DISSERTATION

Submitted to
Michigan State University
in partial fulfillment of the requirements
for the degree of

DOCTOR OF PHILOSOPHY

Department of Physics and Astronomy

1991

ABSTRACT

A STUDY OF MASSIVE ELECTRON PAIRS AND ASSOCIATED PARTICLES PRODUCED AT THE CERN ISR

By

Boyce Milton Humphries

A total of $105e^+e^-$ events, $9e^+e^+$ and $1e^-e^-$ with an invariant mass greater than $11GeV/c^2$ produced in pp collisions at a center-of-mass energy of $62.3GeV$ have been observed. Lead-scintillator shower counters measured the energy of the electrons. Their momenta were measured by a drift chamber array inside a 1.4 T superconducting solenoid.

Cross sections are presented as a function of mass, transverse momentum and rapidity. The quantity $sd^2\sigma/d\sqrt{\tau}dy|_{y=0}$ is expected to be a function of $\tau = (m^2/s)$ only rather than a function of both m and s for the Drell-Yan model. Comparison in this quantity with data at a lower energy ($\sqrt{s}$) confirms this prediction. A mean transverse momentum of 2.20 ± 0.20 GeV/c was found. The average transverse momentum, taken from several experiments, was shown to increase linearly as a function of $\sqrt{s}$.

The tranverse component of the vector sum of associated particles is seen to increase with rising transverse momentum. The multiplicity of associated particles was found to be constant as a function of mass. As a function of p_T, the multiplicity rises from 5 at 0.5 GeV/c to 8 above 3.0 GeV/c .

ACKNOWLEDGEMENTS

I would like to thank the many people who provided the help and support that made this thesis possible. I would like to thank my advisor Bernard Pope for many years of support and guidance. I would also like to thank Jim Linnemann, Stuart Stampke, Bernard Pope and Carlos Salgado for the many weekly meetings that were so important to this research.

To the members of the CMOR collaboration, I am very grateful for their advice and ideas. Special thanks to Leslie Camilleri, Christoph Von Gagern, Timothy Cox, Hans-Jurgen Besh, David Hanna, Mike Tannenbaum and Giuseppe Basini. I would also like to thank Marie Anne Huber, our group secretary, who made our stay in Geneva so pleasant.

Contents

List of Tables

List of Figures

Chapter 1

Introduction

1.1 The Quark Model

Today there are several hundred known "elementary" particles, so it is helpful to begin with some classification of them. There are three major groups; hadrons, leptons, and gauge bosons. The leptons and gauge bosons are at present considered to be elementary: at energies available at today's accelerators, no evidence for structure has been detected in leptons or gauge bosons. Hadrons, on the contrary are composite particles. Several hundred hadrons are known to exist as compared with three lepton families.

In 1964 Gell-Mann[1] and Zweig proposed that hadrons were composed of quarks. These quarks would be spin 1/2 fermions, carry charge +2/3 and -1/3, and have a baryon number of 1/3. Baryons such as the proton and neutron are composed of three quarks. Mesons such as the π^+ and π^- are composed of a quark and an antiquark. In 1964, only three flavors of quarks were needed to account for all the observed hadrons. Today there is evidence for five quarks and a sixth is expected.

Since quarks are fermions they must obey the Pauli exclusion principle. Yet there are certain baryons such as the Δ^{++} and Ω^- that have three quarks with the same charge, baryon number and flavor. It is therefore necessary to add another quantum number to quarks called color. Quarks come in three colors (red, green, and blue). But when quarks combine to make hadrons they do so in a way such that their net

color is zero. That is, hadrons are colorless.

In the 1960's high energy electron beams were used in deep inelastic lepton-nucleon scattering. It was found that the electrons were scattered with large transfer of momentum more frequently than had previously been expected. This suggested that the nucleon has internal structure, in analogy to Rutherford scattering.

Consider an incident electron with energy E being scattered by an angle θ with a final energy E'. These inelastic collisions are generally described in terms of the energy transfer ν and momentum transfer q where

$$\nu = E - E' \quad \text{and} \quad q_\mu = p_\mu - p'_\mu.$$

The general form of the cross section is

$$\frac{d\sigma}{dq^2 d\nu} = \frac{E'}{E}\frac{4\pi\alpha^2}{q^2}\{2W_1(\nu, q^2)\sin^2\frac{\theta}{2} + W_2(\nu, q^2)\cos^2\frac{\theta}{2}\}$$

where $\alpha = 1/137$ is the fine structure constant. It was discovered that at large values of ν and q^2, νW_2 depended only on the ratio q^2/ν. This phenomenon, predicted by Bjorken[2], is known as Bjorken scaling and suggest that the structure observed in the nucleons is "pointlike".

1.2 The Drell-Yan Model

In 1970 Drell and Yan[3] proposed that lepton pairs seen in hadron-hadron collisions[4] were produced by quark-antiquark annihilation to a virtual photon and its decay.

$$h_a + h_b \rightarrow l^+ l^- + X$$

The Drell-Yan model was important in that it made precise predictions. The total cross-section could be predicted with the knowledge of the colliding hadrons' parton distributions $f_i^a(x)$ and $f_i^b(x)$ where x is the quark's fraction of total momentum of the hadron.

$$\frac{d^2\sigma}{dM dx_F} = \frac{8\pi\alpha^2}{9M^3(x_1 + x_2)}\sum_i^{flavor} e_i^2\{f_i^a(x_1)f_i^b(x_2) + f_i^a(x_1)f_i^b(x_2)\}$$

The Drell-Yan model also makes a prediction for the angular distribution of the dileptons

$$\frac{d\sigma}{d\cos\theta} \propto 1 + \cos^2\theta$$

where θ is the angle between the quarks and leptons in the center of mass of the virtual photon.

The "naive" Drell-Yan model also makes predictions about the distribution for transverse momentum of the electron pair, p_T. The p_T of lepton pairs should be zero. However this assumes that the quarks have no initial transverse momentum. From the Heisenberg uncertainty principle the quarks are expected to have an average $p_T \approx 0.3$. It turns out that the data have a higher average p_T that increases with beam energy, which is not predicted by the model. Another problem with the Drell-Yan model is that it predicts a cross-section that is lower than that observed. This discrepancy is usually expressed as the ratio of the measured cross-section to the predicted cross-section and is known as the K factor. These two failures of the Drell-Yan model are generally attributed to the absence of strong interactions in the model.

1.3 Quantum Chromodynamics

Today QCD is regarded as the most likely candidate for a theory of strong interactions. The partons in QCD are quarks and gluons. The quarks come in 3 colors and have some non-zero mass. The gluons, which are massless, mediate the strong force. The gluons have a total of 9 color and anti-color combinations, but one is colorless, so there are 8 gluons that interact with a coupling constant α_s. Since gluons have color charge, they interact with each other. This interaction makes QCD a non-Abelian gauge theory which differs greatly from QED.

In QED an electric charge, because of the virtual electron-positron pairs, polarizes the vacuum. The charge density is higher near the charge and gives an effective

coupling constant α_E. This is given by

$$\alpha_E = \frac{\alpha(\mu)}{1 - \frac{\alpha(\mu)}{3\pi} log(\frac{Q^2}{\mu^2})}$$

where Q is related to the energy of the probe and μ is the lower cutoff energy.

In QCD a quark would be surrounded not only by virtual quark-antiquark pairs but also virtual gluon pairs as well. If there were only quark-antiquark pairs, QCD would behave in much the same way as QED. But the quark can surround itself with gluon-pairs which tend to decrease α_s closer to the quark. The virtual gluons have the greater effect and α_s decreases nearer the quark. More quantitatively

$$\alpha_s(Q) = \frac{12\pi}{(33 - 2n_f)\ln(\frac{Q^2}{\Lambda^2})}$$

where n_f is the number of quark flavors and Λ is the QCD scaling parameter. Note that as Q becomes large α_s approaches zero. This is known as asymptotic freedom. For this reason, perturbative methods can be used in QCD for predictions in high momentum transfer interactions. At lower Q^2 values α_s becomes large which helps explain why no isolated quarks have been observed. In fact, partons which interact through the color force are expected to be confined in such a way that they form color neutral hadrons. Because predictions from QCD based on perturbative theory rely on α_s being small, little is known about the low energy limit of QCD. Unfortunately, the scattering of hadrons inevitably involves these "soft" interactions, as well as any "hard" collision that might occur. Since no one has been able to calculate the soft collisions, we must rely on measured and parameterized quark and gluon densities that describe the distribution of partons in initial state hadrons and fragmentation functions that describe how the final state partons evolve into hadron jets. It is not immediately obvious that this approach is valid. However Collins, Soper and Sterman [5] have proved the validity of factorization to all orders in perturbation theory for leading twist.

Factorization being valid, the Drell-Yan cross-section can be calculated as a perturbative theory series in $\alpha_s(Q^2)$,

$$\sigma = \sum_{k=0} \alpha_s^k(Q^2) A_k$$

where Q^2 plays the role of the momentum scale in the Drell-Yan process. At each order of perturbation the A_i coefficient can be expanded in a series of logarithms of Q^2/Λ^2.

$$A_n = B_{nn} \ln^n(Q^2/\Lambda^2) + B_{nn-1} \ln^{n-1}(Q^2/\Lambda^2) + ...$$

These logarithms arise from multiple hard collinear gluon radiation. Since $\ln(Q^2/\Lambda^2)$ is proportional to $1/\alpha(Q^2)$, summing over all the terms in the perturbation series is required if all terms proportional to some given power of $\alpha_s(Q^2)$ are to be taken into account. The leading log approximation (LLA) retains only the largest power of $\ln(Q^2/\Lambda^2)$ at each order of perturbation. The advantage of the leading log approximation is that it leaves the Drell-Yan cross section unchanged except that the quark densities acquire a Q^2 dependence, the same dependence as that of quark densities in deep inelastic scattering. Figure 1.1 shows the Feynman diagrams contributing to four different cross section. The diagrams for deep inelastic scattering, neutral currents and charged currents differ only by the initial boson (top left of each Feynman diagram), a photon for deep inelastic scattering, Z^0 for neutral currents and $W^{\pm}$ for charged currents. Otherwise the diagrams are the identical. While lowest order predictions agree well between deep inelastic scattering, and charged and neutral currents, predictions of the Drell-Yan cross section are about a factor of 2 below the measured values.

In a paper by Altarelli, Ellis and Martinelli [6] the cross section $d\sigma/dQ^2dx_F$ is calculated in QCD retaining all terms up to order $\alpha_s(Q^2)$. Expressed in terms of the bare quark and gluon distributions the cross section is given by

$$\frac{d\sigma^{DY}}{dQ^2}(AB \to l\bar{l}X) = \frac{4\pi\alpha^2}{9SQ^2} \sum_f e_f^2 \int_0^1 \frac{dx_1}{x_1} \int_0^1 \frac{dx_2}{x_2}$$

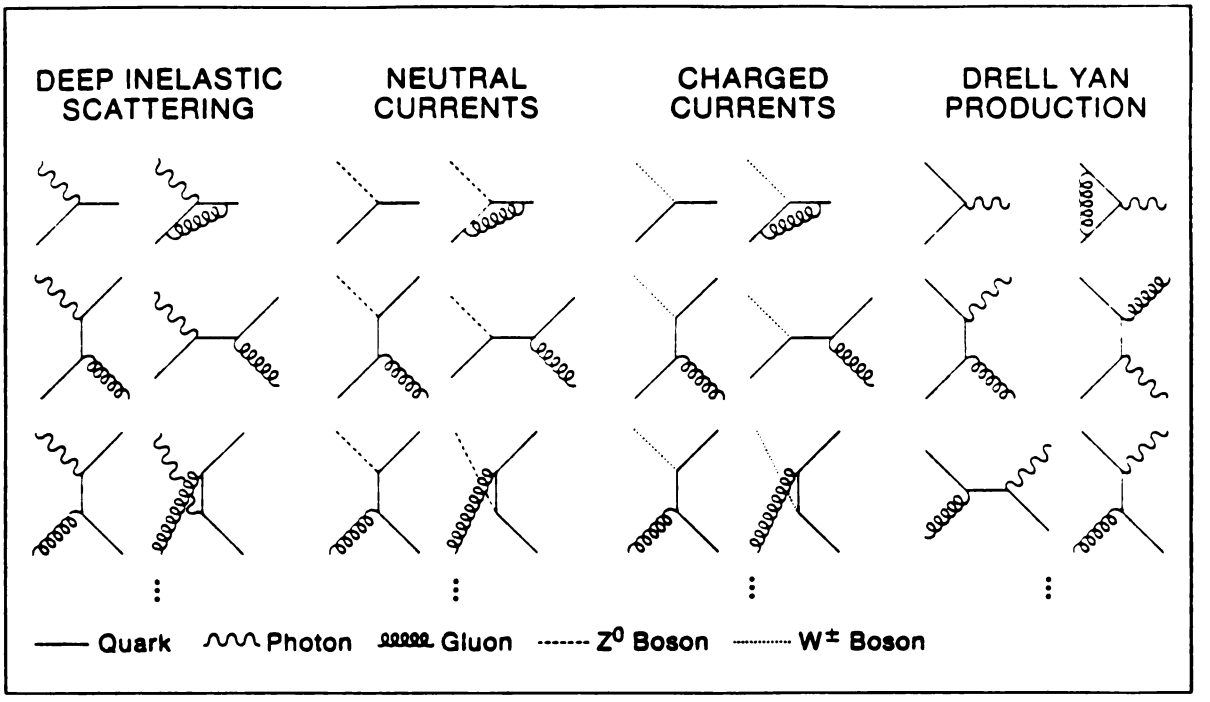

Figure 1.1: Comparison of Feynman diagrams for different processes.

$$\left\{\left[q_f^{[1]}(x_1)\bar{q}_f^{[2]}(x_2)+(1\leftrightarrow 2)\right]\left[\delta(1-z)+\theta(1-z)\left(\frac{\alpha_s(t)}{2\pi}2P_{qq}(z)t+\alpha_s(t)f_{q,DY}(z)\right)\right]\right.$$
$$\left.+\left[\left(q_f^{[1]}(x_1,t)+\bar{q}_f^{[1]}(x_1,t)\right)g^{[2]}(x_2)+(1\leftrightarrow 2)\right]\theta(1-z)\left[\frac{\alpha_s(t)}{2\pi}P_{qg}(z)t+\alpha_s(t)f_{g,DY}(z)\right]\right\}$$

where $z=\tau/(x_1x_2)=Q^2/s$ and $t=\ln Q^2/\mu^2$. $P_{qq}(z)$ and $P_{qg}(z)$ are respectively the quark-quark and quark-gluon splitting functions. The terms $\alpha_s f_{q,DY}(z)$ and $\alpha_s f_{g,DY}(z)$ are associated with the diagrams of figure 1.2b) and 1.2c), respectively. Because of infrared and collinear singularities in the terms $f_{q,DY}$ and $f_{g,DY}$ it is more convenient to express the cross section in terms of Q^2-dependent quark distribution functions which gives

$$\frac{d\sigma^{DY}}{dQ^2}(AB\rightarrow l\bar{l}X)=\frac{4\pi\alpha^2}{9SQ^2}\sum_f e_f^2\int_0^1\frac{dx_1}{x_1}\int_0^1\frac{dx_2}{x_2}$$
$$\left\{\left[q_f^{[1]}(x_1,t)\bar{q}_f^{[2]}(x_2,t)+(1\leftrightarrow 2)\right]\left[\delta(1-z)+\alpha_s(t)\theta(1-z)\left(f_{q,DY}(z)-2f_{q,2}(z)\right)\right]\right.$$

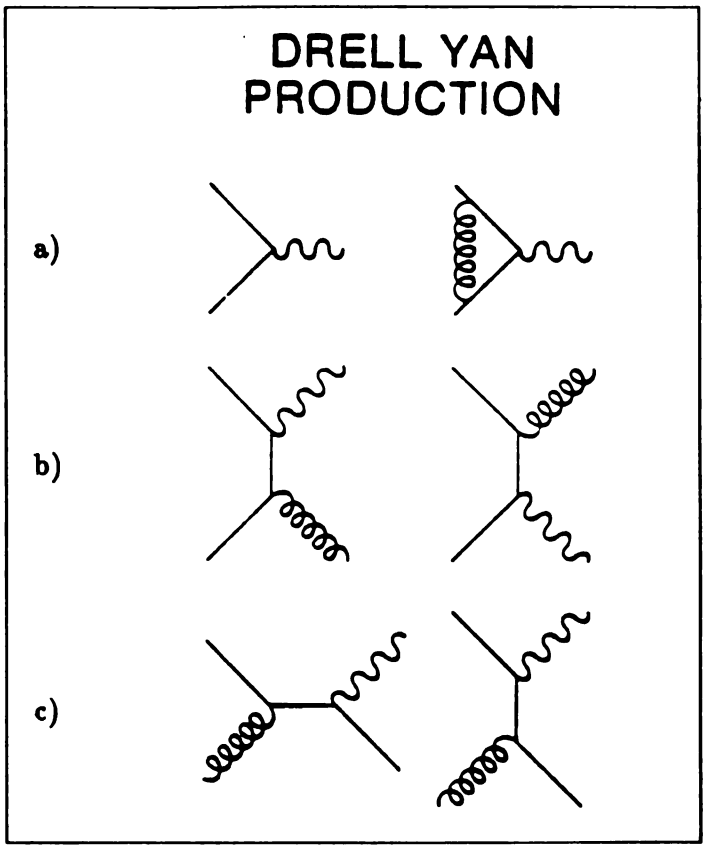

Figure 1.2: Feynman diagrams for electron pair production.

$$+\left[\left(q_f^{[1]}(x_1,t)+\bar{q}_f^{[1]}(x_1,t)\right)g^{[2]}(x_2)+(1\leftrightarrow 2)\right]\alpha_s(t)\theta(1-z)(f_{g,DY}(z)-f_{g,2}(z))\Big\}$$

The terms $\alpha_s f_{q,2}(z)$ and $\alpha_s f_{g,2}(z)$ are associated with the diagrams of figure 1.3b) and 1.3c), respectively. Therefore the contributions of order α_s in deep inelastic scattering have been subtracted out and replaced by contributions of order α_s from Drell-Yan. The two terms $(f_{q,DY}-2f_{q,2})$ and $(f_{g,DY}-f_{g,2})$ are free of singularities since the singularities in Drell-Yan cancel those in deep inelastic scattering.

$$\alpha_s(t)\left(f_{q,DY}(z)-2f_{q,2}(z)\right)=$$
$$\frac{\alpha_s(t)}{2\pi}\frac{4}{3}\left\{\frac{3}{(1-z)_+}-6-4z+2(1+z^2)\left[\frac{\ln(1-z)}{(1-z)}\right]_+ +\left(1+\frac{4\pi^2}{3}\right)\delta(1-z)\right\}$$

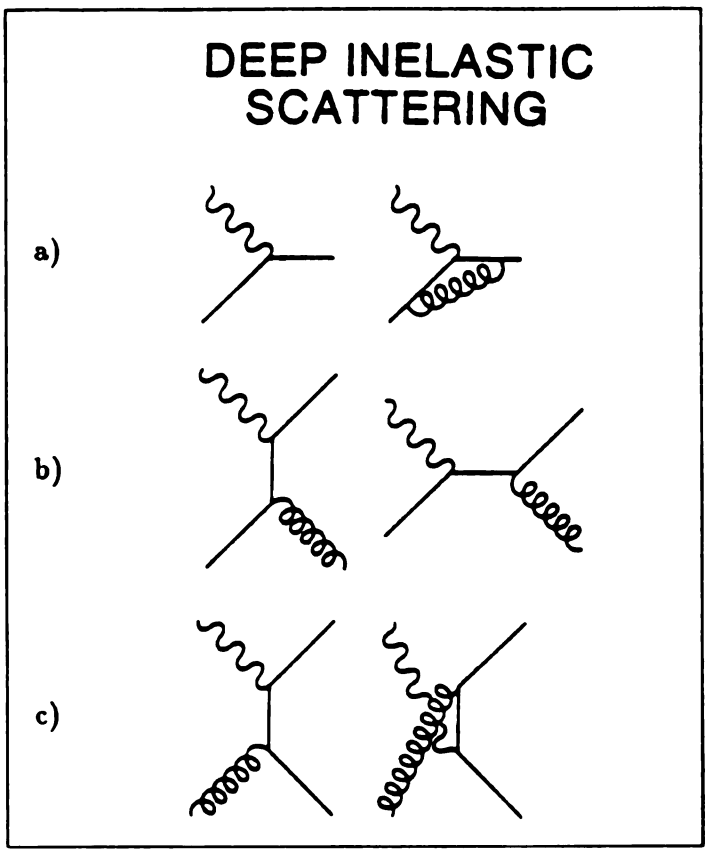

Figure 1.3: Feynman diagrams for deep inelastic scattering.

$$\alpha_s(t)\,(f_{g,DY}(z) - f_{g,2}(z)) = \frac{\alpha_s(t)}{2\pi}\frac{1}{2}\left\{[z^2 + (1-z)^2]\ln\frac{(1-z)^2}{z} + \frac{9}{2}z^2 - 5z + \frac{3}{2}\right\}. \tag{1.1}$$

At sub-asymptotic energies, the $(f_{q,DY}(z) - 2f_{q,2}(z))$ correction is large and positive. This is true for pp scattering (where the leading term is proportional to small sea densities) as well as for the (not so obvious case) of πp and $p\bar{p}$ scattering (valence-valence processes). In contrast, the correction due to the $(f_{g,DY}(z) - f_{g,2}(z))$ term is small and negative even for pp scattering.

One test of the QCD theory is the prediction of the q_T distribution. Initially only certain regions of the q_T were predicted, making comparison to data of limited use. But an expression for the distribution of q_T has been found [7]. This expression for

the q_T distribution satisfies the following requirements:

1. The $O(\alpha_s)$ perturbative distribution coming from one-gluon emission is recovered at large q_T.

2. Soft gluon resummation is performed at leading double logarithmic accuracy in the $q_T \ll Q$ region.

3. Only terms corresponding to the emission of soft gluons are resummed.

4. The integral of the q_T distribution reproduces the known results for the $O(\alpha_s)$ total cross sections.

5. The average value of q_T^2 is also identical with the perturbative result at $O(\alpha_s)$.

6. All quantities are expressed in terms of precisely defined quark distribution functions at a specified scale.

To perform the calculations the cross section is split into two pieces.

$$\frac{d\sigma}{dQ^2 dq_T^2 dy} = X(q_T^2, Q^2, y) + Y(q_T^2, Q^2, y) \tag{1.2}$$

The X term is an integrable distribution but is singular at $q_T = 0$. The Y term is finite as $q_T \to 0$. By performing a Fourier transform of X into impact parameter space the collinear singularities can be factored into the parton distribution functions of deep inelastic scattering. After a resummation is performed in impact space, a second Fourier transform returns X back to q_T space. As a result the equation for the Drell-Yan cross section is

$$\frac{d\sigma}{dQ^2 dq_T^2 dy} = N\left(\int \frac{d^2\mathbf{b}}{4\pi} e^{-i\mathbf{q_T}\cdot\mathbf{b}} R(b^2, Q^2, y) e^{S(b^2,Q^2,y)} + Y(q_T^2, Q^2, y)\right) \tag{1.3}$$

where $N = 4\pi\alpha^2/9Q^2S$,

$$S(b^2, Q^2, y) = \int_0^{A_T^2} \frac{dk^2}{k^2} \frac{4\alpha_s(k^2)}{3\pi} [J_0(bk) - 1] \left\{[1 + D\alpha_s(k^2)] \ln(Q^2/k^2) - \frac{3}{2}\right\} \tag{1.4}$$

and

$$
\begin{aligned}
R(b^2,Q^2,y) &= H(x_1^0,x_2^0,P^2)\left[1+\frac{\alpha_s(t)}{2\pi}\frac{4}{3}\left(-3\ln\frac{A_T^2}{Q^2}-\ln^2\frac{A_T^2}{Q^2}\right)\right] \\
&+\frac{\alpha_s(t)}{2\pi}\frac{4}{3}\left[\int_{x_1^0}^1\frac{dz}{z}f_q(z)H(x_1^0/z,x_2^0,P^2)+\int_{x_2^0}^1\frac{dz}{z}f_q(z)H(x_1^0,x_2^0/z,P^2)\right] \\
&+\frac{\alpha_s(t)}{2\pi}\frac{1}{2}\left[\int_{x_1^0}^1\frac{dz}{z}f_g(z)K_2(x_1^0/z,x_2^0,P^2)+\int_{x_2^0}^1\frac{dz}{z}f_g(z)K_1(x_1^0,x_2^0/z,P^2)\right].
\end{aligned}
\tag{1.5}
$$

Other expressions needed for the calculation are

$$
A_T/\sqrt{S}=[(1+\tau)^2/4ch^2(y)-\tau]^{1/2} \tag{1.6}
$$

and

$$
2\pi D=(\frac{67}{6}-\frac{1}{2}\pi^2-\frac{5}{9}n_f). \tag{1.7}
$$

The Y term can be split into the $q\bar{q}$ annihilation term and the Compton scattering term.

$$
Y(q_T^2,Q^2,y)=\frac{\alpha_s(t)}{2\pi}\frac{4}{3}Y_q(q_T^2,Q^2,y)+\frac{\alpha_s(t)}{2\pi}\frac{1}{2}Y_g(q_T^2,Q^2,y), \tag{1.8}
$$

The annihilation term is given by

$$
\begin{aligned}
Y_q(q_T^2,Q^2,y) &= -\frac{2}{S}\left[\int_{\sqrt{\tau_+}e^y}^1\frac{dx_1}{(x_1-x_1^+)}\frac{H(x_1,x_2^*)}{x_1x_2^*}\int_{\sqrt{\tau_+}e^{-y}}^1\frac{dx_1}{(x_2-x_2^+)}\frac{H(x_1^*,x_2)}{x_1^*x_2}\right] \\
&+\frac{1}{q_T^2}\left\{\int_{\sqrt{\tau_+}e^y}^1\frac{dx_1}{(x_1-x_1^+)}\left[H(x_1,x_2^*)\left(1+\left(\frac{\tau}{x_1x_2^*}\right)^2\right)-2H(x_1^0,x_2^0)\right]\right. \\
&+\int_{x_1^0}^1\frac{dx_1}{(x_1-x_1^0)}\left[H(x_1,x_2^0)\left(1+\left(\frac{x_1^0}{x_1}\right)^2\right)-2H(x_1^0,x_2^0)\right] \\
&+\int_{\sqrt{\tau_+}e^{-y}}^1\frac{dx_2}{(x_2-x_2^+)}\left[H(x_1^*,x_2)\left(1+\left(\frac{\tau}{x_1^*x_2}\right)^2\right)-2H(x_1^0,x_2^0)\right] \\
&+\int_{x_2^0}^1\frac{dx_2}{(x_2-x_2^0)}\left[H(x_1^0,x_2)\left(1+\left(\frac{x_2^0}{x_2}\right)^2\right)-2H(x_1^0,x_2^0)\right] \\
&\left.+H(x_1^0,x_2^0)\ln\frac{(1-x_1^+)(1-x_2^+)}{(1-x_1^0)(1-x_2^0)}\right\}
\end{aligned}
\tag{1.9}
$$

while Compton scattering gives

$$
\begin{aligned}
Y_g(q_T^2,Q^2,y) \;=\; & \left\{ \frac{1}{q_T^2}\int_{\sqrt{\tau_+}e^y}^1 \frac{dx_1}{(x_1-x_1^+)} K_1(x_1,x_2^*)\left[\frac{x_2^* x_1^+ - \tau}{x_1 x_2^*} - \frac{2\tau(x_2^* x_1^+ - \tau)^2}{(x_1 x_2^*)^3}\right] \right. \\
& + \frac{1}{q_T^2}\int_{\sqrt{\tau_+}e^{-y}}^1 \frac{dx_2}{(x_2-x_2^+)} K_1(x_1^*,x_2)\left[\frac{x_2 x_1^+ - \tau}{x_1^* x_2} - \frac{2\tau(x_2 x_1^+ - \tau)^2}{(x_1^* x_2)^3}\right] \\
& - \frac{1}{q_T^2}\int_{x_2^0}^1 \frac{dx_2}{x_2} K_1(x_1^0,x_2)\left[1 - 2\frac{x_2^0}{x_2}\left(1-\frac{x_2^0}{x_2}\right)\right] \\
& + \frac{1}{S}\left[\int_{\sqrt{\tau_+}e^y}^1 \frac{dx_1}{(x_1-x_1^+)} K_1(x_1,x_2^*)\frac{x_1 x_2^+ - \tau}{(x_1 x_2^*)^2}\right. \\
& \qquad \left. + \int_{\sqrt{\tau_+}e^{-y}}^1 \frac{dx_2}{(x_2-x_2^+)} K_1(x_1^*,x_2)\frac{x_1^* x_2^+ - \tau}{(x_1^* x_2)^2}\right] \\
& \left. + (1 \leftrightarrow 2)\right\}. \qquad (1.10)
\end{aligned}
$$

The product of the quark-quark distribution functions is defined as

$$H(x_1,x_2,Q^2) = \sum_f e_f^2 \left\{ q_f^{[1]}(x_1,Q^2)\bar{q}_f^{[2]}(x_2,Q^2) + (1 \leftrightarrow 2)\right\} \qquad (1.11)$$

and the products of the quark-gluon distribution functions are given by

$$K_1(x_1,x_2,Q^2) = \sum_f e_f^2 \left[q_f^{[1]}(x_1,Q^2) + \bar{q}_f^{[1]}(x_1,Q^2)\right] g^{[2]}(x_2,Q^2) \qquad (1.12)$$

and

$$K_2(x_1,x_2,Q^2) = \sum_f e_f^2 \left[q_f^{[2]}(x_2,Q^2) + \bar{q}_f^{[2]}(x_2,Q^2)\right] g^{[1]}(x_1,Q^2). \qquad (1.13)$$

The expression in equation 1.3 for the q_T distribution was initially derived for the production of the W and Z bosons. Only the definitions for H, K_1 and K_2 differ for Drell-Yan. The numerical result for the q_T distribution for p-p scattering as well as data can be found in reference [8]. Comparison between these predictions and the final data of this experiment are found in figure 4.11 of this thesis. The q_T distribution of the prediction are determined using the parton densities given by Duke and Owens with acceptable values of the QCD scale Λ. No other free parameters were used, nor any intrinsic transverse momentum.

Chapter 2

The ISR and the R110 Detector

2.1 The Intersecting Storage Rings

The ISR, the first large proton-proton storage ring accelerator, consisted of two concentric rounded squares with one rotated by 45° with respect to the other (see figure 2.1). There were 8 intersection regions with the beams making a crossing angle of 14.7°. The rings were usually filled with protons which circulated in opposite directions. The ISR was filled by two lines, one for each ring, connected to the CERN Proton Synchrotron. Usually the PS accelerates protons to 26 GeV. The protons were then extracted from the PS through a transfer line and injected into a ring of the ISR where they were accumulated by stacking. This continued until the ring was filled. Then the second ring would be filled.

2.1.1 Beam Energies and Currents

Although the ISR usually ran with beam energies of 31 GeV it also ran with beam energies of 15, 22, and 26 GeV. Typical beam currents during the later years of the ISR were 32 Amps in each ring. The ISR was also capable of running with particles other than protons. Data from protons on antiprotons, proton on deuteron, deuteron on deuteron, proton on alpha and alpha on alpha were all collected from runs at the ISR.

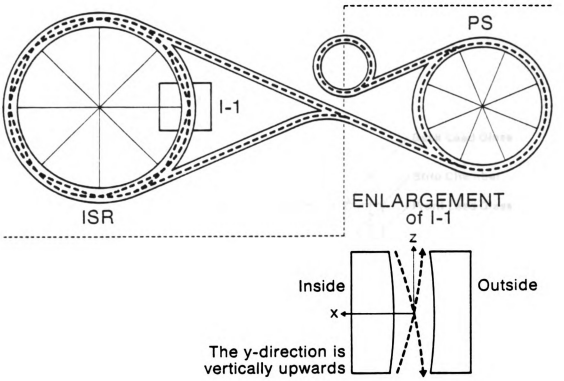

Figure 2.1: The ISR and PS.

2.2 The Coordinate System

The system of coordinates used in this experiment (see figures 2.1, 2.2 and 2.3.) are a right handed Cartesian set (x, y, z) with the origin at the center of the solenoid, x pointing towards the center of the ISR rings, y vertically up and z along the solenoid axis in the direction of ISR intersection region 8. When spherical coordinates (r, ϕ, θ) are used, $\phi = 0$ is in the x-z plane and $\theta = 0$ is along the $+z$ axis.

2.3 The Detector

2.3.1 Solenoid

A uniform 1.4T magnetic field was produced by the superconducting solenoid. The 2000 amps of current needed to generate this field were conducted through niobium-titanium wires embedded in a copper matrix. This matrix was then wrapped around

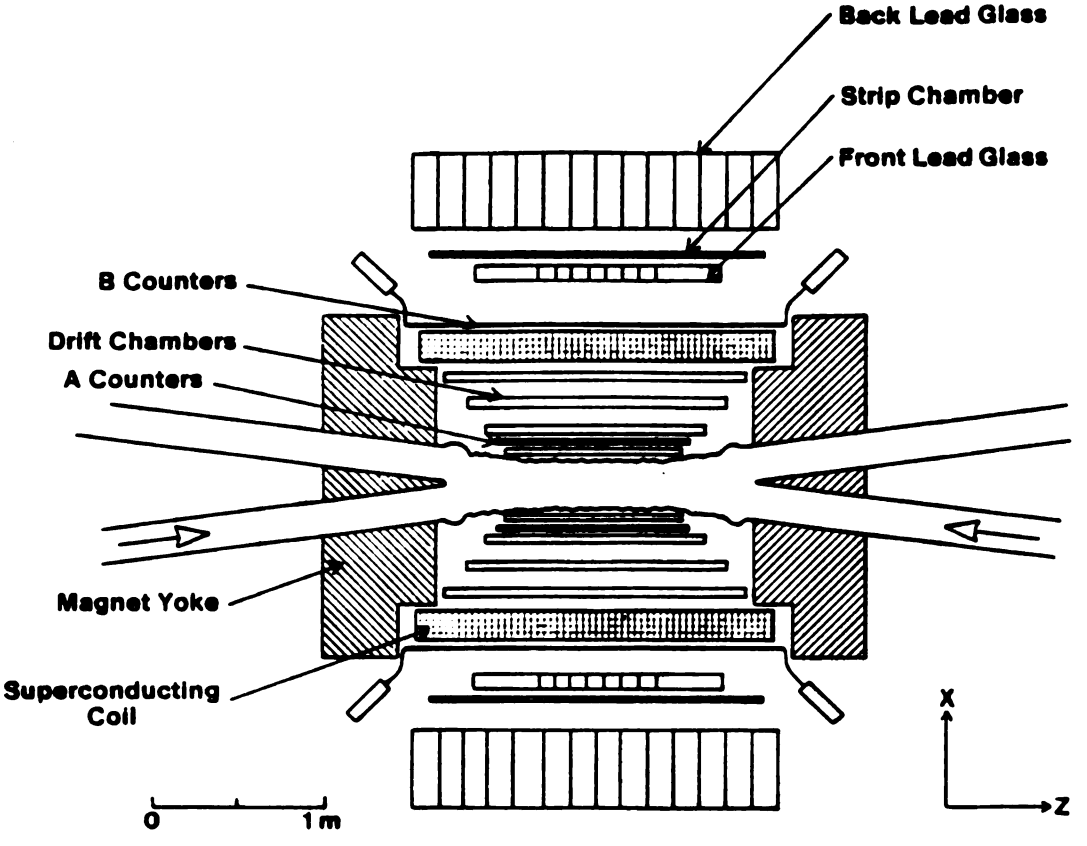

Figure 2.2: The plan view of the R110 detector

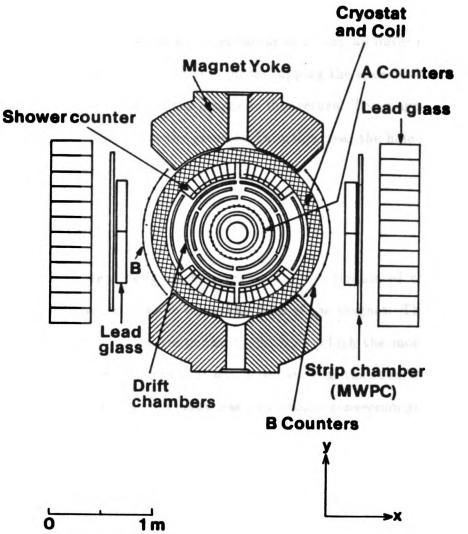

Figure 2.3: The end view of the R110 detector

a stainless steel core to provided the needed strength. Strips of pure aluminum surrounded this matrix and provided a current path and thermal sink in the event of the magnet going normal.

This was one of the first large superconducting solenoids built for a high energy physics experiment. The coil had an inner radius of 70 cm, an outer radius of 89 cm and was 170 cm in length. Soft iron pole pieces capping the ends of the solenoid and a yoke, also of soft iron, provided the magnetic flux return. The magnetic field had a uniformity to within 1.5%, with the greatest distortion near the hole in the iron end pieces provided for the beam pipe.

2.3.2 Drift Chambers

The drift chambers were designed to measure the momentum of charged particle tracks over the full azimuth in the solenoidal field of the magnet. This was done by measuring the radius of curvature of the track, from which the momentum can be found if the magnetic field is known. It was necessary that the chambers be rigid and yet be low in mass for minimum energy loss and photon conversion and that they be able to resolve tracks nearby in a space in the face of high track multiplicity.

The chambers were constructed in self contained sectors. These sectors combined to form cylindrical layers. Three layers were complete cylinders (DCM1, DCM2, & DCM3), and two others (DCM4, & DCM5) were inserted between DCM2 and DCM3 or placed within the acceptance of the lead glass. Each sector consisted of two 6 mm thick gaps, inner and outer. Sense wires and field wires were mounted axially and the position of these two were exchanged between the two gaps. The sense wires were 20μm gold plated tungsten wires strung at a tension of 40g. Field wires were 100μm of copper beryllium, with 100g of tension. The sense wires were held 3 mm from the cathode planes by 3 mm $\times$ 3 mm $\times$ 6 mm glass beads every 50 cm. The time recorded from the sense wires and the wire's position provided the azimuthal

Table 2.1: Description of drift chamber modules

Module	DC1	DC2	DC3	DC4	DC5
Mean Radius (cm)	20.0	34.0	49.2	63.8	49.0
Length (cm)	80.0	103.0	127.0	150.0	150.0
Sense-Field wire pitch(cm)	1.28	1.49	1.91	2.20	2.20
Sense-Field dist.	13	15	19	22	22
Number of Sense Wires	96	144	160	64	96
Number of Sectors	4	6	8	4	6
Cathode Lines per Cell	16	20	24	28	28

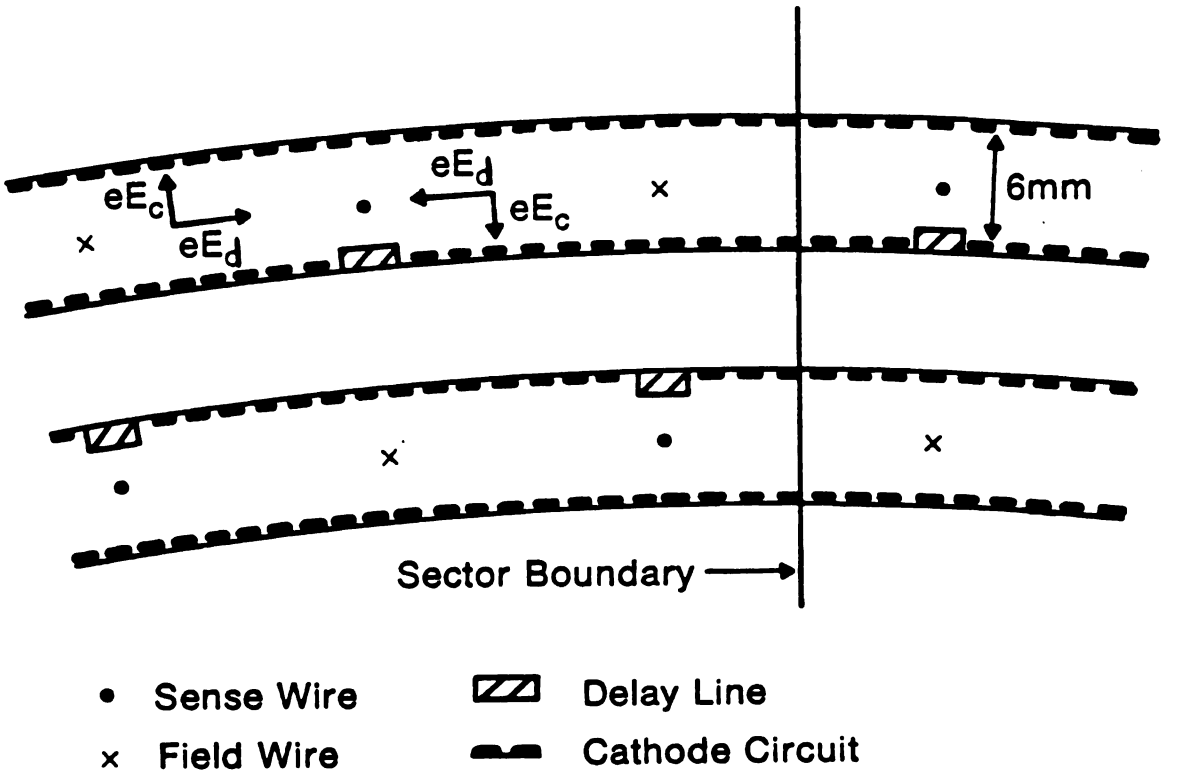

Figure 2.4: Electric field in drift chambers

and radial coordinate of a particle hit. To measure the z coordinate, delay lines were glued to the cathode running parallel to the sense wires. These delay lines were read out on both ends and the time of the arrival of the pulse recorded. The difference between the two times gives the z coordinate. The average spatial resolution was measured to be σ_z= 0.8 cm. Because of the high impedance (see table 2.2) the noise was kept low while low R/Z kept resistance losses down.

To compensate for the Lorentz force of the magnetic field, two components for the E field were needed, E_c and E_d (see figure 2.4). This was done by adjusting the individual cathode strips to give the resulting field pattern in both angular E_d and radial E_c components. The resulting field values were $E_d = 1.0 \frac{kV}{cm}$ and $E_c = 1.2 \frac{kV}{cm}$. Unfortunately, it was impossible to maintain a uniform drift field near the field wires. For this reason a polyatomic gas was used to reduce the dependence in the time-distance relation on the field. This is possible because there is a velocity plateau above some critical E field. Argon was added then to prevent the polymerization that occurs in a high radiation environment. The result was 50-50% mixture of argon-ethane with a typical drift velocity of 50 $\frac{\mu m}{ns}$. The sense wires were held nominally at a voltage of +1.7kV. The delay lines were at ground.

Tests at the CERN Proton Synchrotron (PS) test showed the linear time-distance relationship to be constant to 1% and gave a position resolution as good as 170μm. A survey of the drift chambers were made each time the solenoid was opened. Cosmic ray data were taken with the magnet on but the beams off using the $Y \bullet A \bullet A \bullet Y$ trigger (see section 2.3.3 and 2.3.7 for a discussion on the A and Y counters) and used for positional information of the drift chambers. The cosmic ray tracks had the advantage of having twice the number of points and three times the lever arm of normal beam data. To determine the track, a fit was made to minimize the residuals using the position of the drift chambers and the simple time-distance relation. This was an iterative process with the the survey value being the initial values. Thereafter the center of curvature of the chambers was constrained and parameters being fit for were left out of the corresponding fit. The distance from a sense wire was given by a quadratic in time multiplied by a small angle dependent factor to allow different drift properties of the electron when the track was not normally incident. Different constants for each side of each gap were required. The best position resolution with beam on was found to be 400μm rms, with uncertainties being in the time-distance

relationship and the exact shape of the chambers. In order to find the momentum resolution, a Monte Carlo program was used that generated tracks with known momentum and points with the measured resolution. These points were then supplied to the usual track fitting routine. The momentum was found to be

$$\begin{aligned} \Delta p_T/p_T &= 3\%\ p_T(\text{ GeV }) \quad \text{for tracks with all 8 points} \\ \Delta p_T/p_T &= 15\%\ p_T(\text{ GeV }) \quad \text{for tracks with only 5 points} \\ \Delta p_T/p_T &= 7\%\ p_T(\text{ GeV }) \quad \text{for overall average} \end{aligned}$$

These numbers agree fairly well with those obtained from tracks fitted from the two halves of cosmic ray tracks.

Table 2.2: Characteristics of drift chamber signals

Delay	2.3 $\frac{ns}{cm}$
Impedance, Z	550 Ω
DC Winding Resistance, R	110 Ω/m
Attenuation of Chamber	2.5 db/m
Line-to-Line Variations in Delay and Impedance	3% rms
Internal Reflections (Typical)	<1%
Length (Depending on Module)	80 – 150 cm

Drift Chamber Read Out

The electronic readout for the drift chambers handled 580 sense wires and 1160 delay lines. The delay lines were amplified by a factor of 10 by a hybridized emitter follower circuit. Signals from 580 sense wires and 1160 delay lines were led out of the solenoid by 3m of RG174 cable, amplified by a factor of 160 and clipped to a 60 ns pulse length. The signals were then connected to the counting room by 35m of RG58 cable. They were discriminated and then fed into the time-digitizing system. The same system digitized times for the scintillation counters and back lead glass signals (see section 2.3.10 for a discussion of the lead glass). The dead time of the discriminators was ~60ns.

2.3.3 A Counters

The "A" counters consisted of 32 scintillators forming a barrel hodoscope. Located between the DC1 and DC2 drift chambers at a radius of 26.5 cm each counter was 87.5 cm long, 4.8 cm wide and 0.6 cm thick. The counters were read out at both ends, giving a total of 64 A counter signals. Light guides were used at both ends of the counters to direct the signal outside the solenoid. A second set of light guides, connected to the first through the air gap in the magnetic endcaps, channeled the light to Mullard XP2230 phototubes. These phototubes were chosen because of their short rise time of 1.6 ns and their high gain. The short rise time was necessary because they are used as the reference time zero of the event. The high gain is needed to boost the weak signal from the thin A counters, made weaker by the long light path. These phototubes were mounted on the return yoke of the magnet and encased in μ metal shields to minimize the magnetic field.

2.3.4 B Counters

The "B" counters were positioned just outside the solenoid at a radius of 87.5 cm and covered the area between the iron yokes on both sides of the magnet. They formed two hodoscopes of 12 scintillator counters each. Each counter was 184 cm long, 11.2 cm wide, 1 cm thick and was read out on both ends. Short light guides directed light from the B counter to 56AVP phototubes. The signal from the phototubes was then split, with one part going to discriminators and timers and the other part going to LeCroy 2249 ADC's for digitization. The B counters were used to detect electromagnetic showering in the coil by electrons and photons.

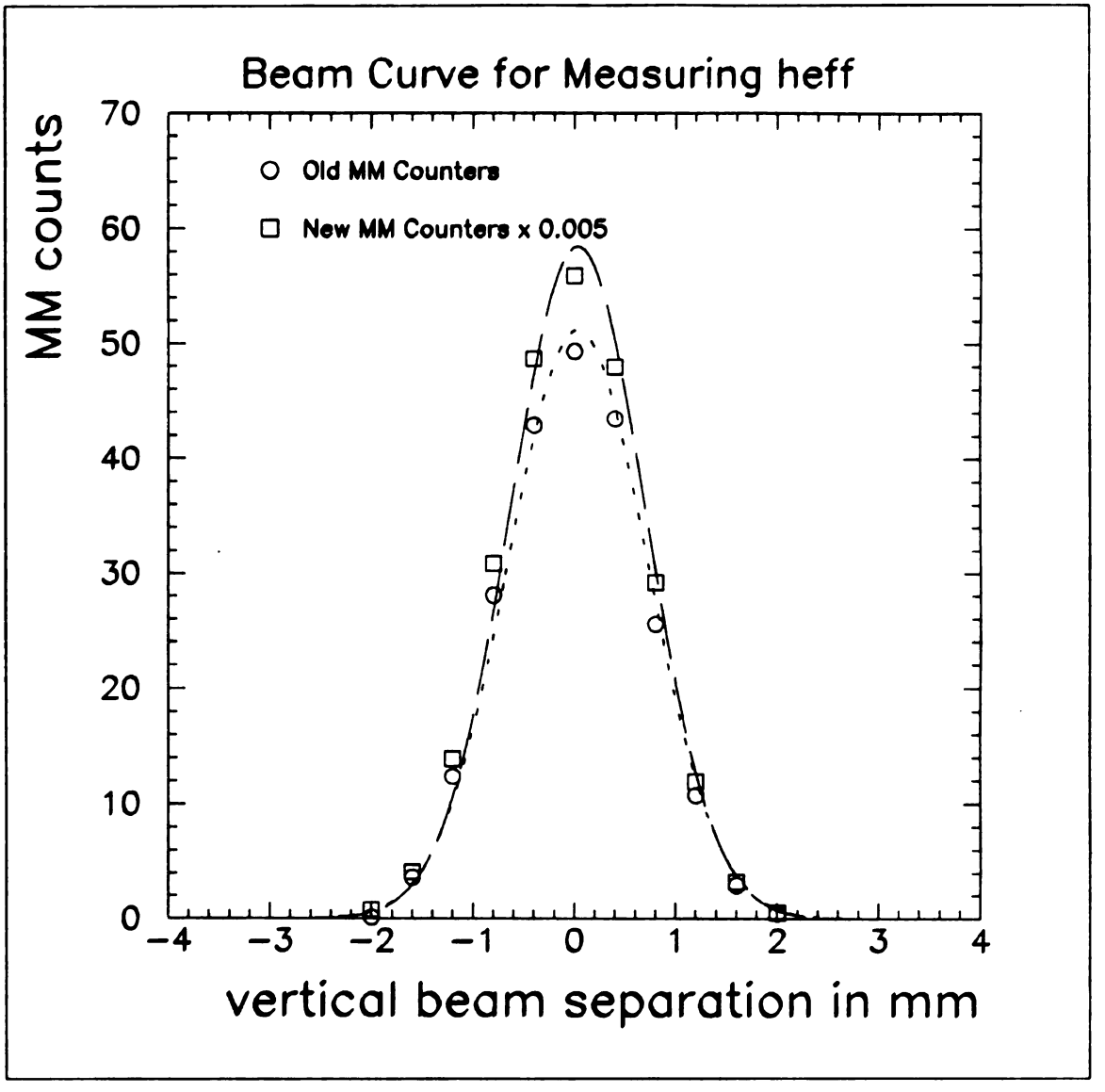

Figure 2.5: The beam curve

The beam curve was used to obtain the effective height of the intersection of the two beams. The two beam curves above come from the two sets of counters used to measure the luminosity, the "old" and "new" MM counters.

2.3

Lur

In

lon

lur

bo

cer

an

wr

Th

in

β

Va

one

To

thu

2.3.5 Luminosity and the MM Counters

Luminosity is defined as the counting rate per unit cross section or

$$\mathcal{L} = \frac{1}{\sigma}\frac{dN}{dt}. \tag{2.1}$$

In order to detect rare events it is necessary to have either a high luminosity or a long running time.

In order to measure the luminosity at the ISR another equation is needed for the luminosity. Consider the case of two crossing rectangular beams in the lab frame, both with width w, and height h. Furthermore the density in particles per cubic centimeters for each beam is n_1 for beam one, and n_2 for beam two. The crossing angle is α and the particle's velocity is v for both beams. The luminosity can be written as

$$\mathcal{L} = \frac{1}{\sigma}\left(\frac{\text{interactions}}{\text{traversal}}\right)\cdot(\text{lab traversal rate}). \tag{2.2}$$

The number of interactions per traversal is Lorentz invariant and is easier to consider in the rest frame of beam two. The relative velocity of the two frames is given by β as a fraction of the speed of light. The variable γ is the usual $\gamma = (1-\beta^2)^{-1/2}$. Variables in this frame will be primed. Consider the traversal of one particle in beam one. Then

$$\frac{\text{interactions}}{\text{traversal}} = \text{rate}\cdot\text{traversal time} \tag{2.3}$$

$$= \sigma n_2' v_1' \frac{w'}{v_1' \sin\alpha'}. \tag{2.4}$$

To get back to the lab frame use is made of the two equations

$$\sin\alpha' = \frac{\tan\frac{\alpha}{2}}{\gamma}\frac{1}{\sqrt{1+\frac{\tan^2\frac{\alpha}{2}}{\gamma^2}}} \approx \frac{\tan\frac{\alpha}{2}}{\gamma} \tag{2.5}$$

$$n_2' = n_2/\gamma \tag{2.6}$$

thus

$$\frac{\text{interactions}}{\text{traversal}} = \frac{\sigma n_2 w}{\tan\alpha/2} \tag{2.7}$$

The lab traversal rate is simply

$$\text{lab traversal rate} = n_1 w h v_1. \tag{2.8}$$

Combining equations 2.2, 2.7 and 2.8 gives

$$\mathcal{L} = \frac{\sigma n_1 n_2 w^2 h c}{\tan(\alpha/2)} \tag{2.9}$$

The currents in beam one and beam two are

$$I_1 = e n_1 w h v \tag{2.10}$$

$$I_2 = e n_2 w h v \tag{2.11}$$

respectively. A substitution to replace the width and density dependence with a current dependence gives

$$\mathcal{L} = \frac{1}{ce^2} \frac{I_1 I_2}{h \tan(\alpha/2)} \tag{2.12}$$

Since the beams were not rectangular h is replaced by h_{eff} for the more general equation

$$\mathcal{L} = \frac{1}{ce^2} \frac{I_1 I_2}{h_{\text{eff}} \tan(\alpha/2)} \tag{2.13}$$

where

$$h_{\text{eff}} = \frac{\int \rho_1(z)dz \cdot \int \rho_2(z)dz}{\int \rho_1(z)\rho_2(z)dz} \tag{2.14}$$

and where $\rho_i(z)$ are the beam vertical densities.

Since the currents are usually well known, only h_{eff} is yet to be found. This is accomplished by measuring the beam curve [9] (see figure 2.5). The rate of interactions measured by the set of "MM" counters (see section 2.3.5) is related to the beam densities by the equation

$$R(\Delta z) = k \int \rho_1(t + \frac{\Delta z}{2}) \rho_2(t - \frac{\Delta z}{2}) dt. \tag{2.15}$$

where Δz is the beam separation distance and $R(\Delta z)$ is known as the beam curve. This equation shows that the denominator of equation 2.14 is proportional to

$R(\Delta z)_{max}$ if h_{eff} is chosen to be minimum. Integrating equation 2.15 over the beam separation distance and rearranging gives

$$\int R(\Delta z)d(\Delta z) = k\int\int \rho_1(t+\frac{\Delta z}{2})\rho_2(t-\frac{\Delta z}{2})dtd(\Delta z) \quad (2.16)$$

$$= k\int\int \rho_1(t+\frac{\Delta z}{2})\rho_2(t-\frac{\Delta z}{2})d(t+\frac{\Delta z}{2})d(t-\frac{\Delta z}{2}) \quad (2.17)$$

$$= k\int \rho_1(z_1)dz_1 \int \rho_2(z_2)dz_2 \quad (2.18)$$

which is proportional to the numerator in equation 2.14. So, h_{eff} can be rewritten as

$$h_{eff} = \frac{\text{(Area Under Curve)}}{(dN/dt)_{max}}. \quad (2.19)$$

If the beam curve is Gaussian then

$$h_{eff} = 2\sqrt{\pi}\sigma_{beam} = \sqrt{2\pi}\sigma_{beamcurve} \approx 1.062 \times FWHM_{beamcurve}. \quad (2.20)$$

Since the luminosity can be calculated the constant, κ, that converts the rates in the luminosity counters to the luminosity can be found by the equation

$$\kappa = \frac{(dN/dt)_{max}}{\mathcal{L}}. \quad (2.21)$$

Old MM Counters

The "MM" counters were used to measure the luminosity. They consisted of eight scintillator sheets measuring 43 cm by 20.5 cm mounted in pairs on the four corners of the magnet not shielded by the return yoke. From the interaction region and looking inwards they appeared top right and bottom left. Looking outwards they were top left and bottom right. Therefore an interaction producing back to back particles would have to hit two sets of "MM" counters, a top set and a bottom set. A coincidence of four scintillators in this combination was used to define one real event.

New MM counters

The interaction rates of the old MM counters were too low to measure the luminosity of $\bar{p}$-p stacks. So the new MM counters were designed to be high rate counters. This

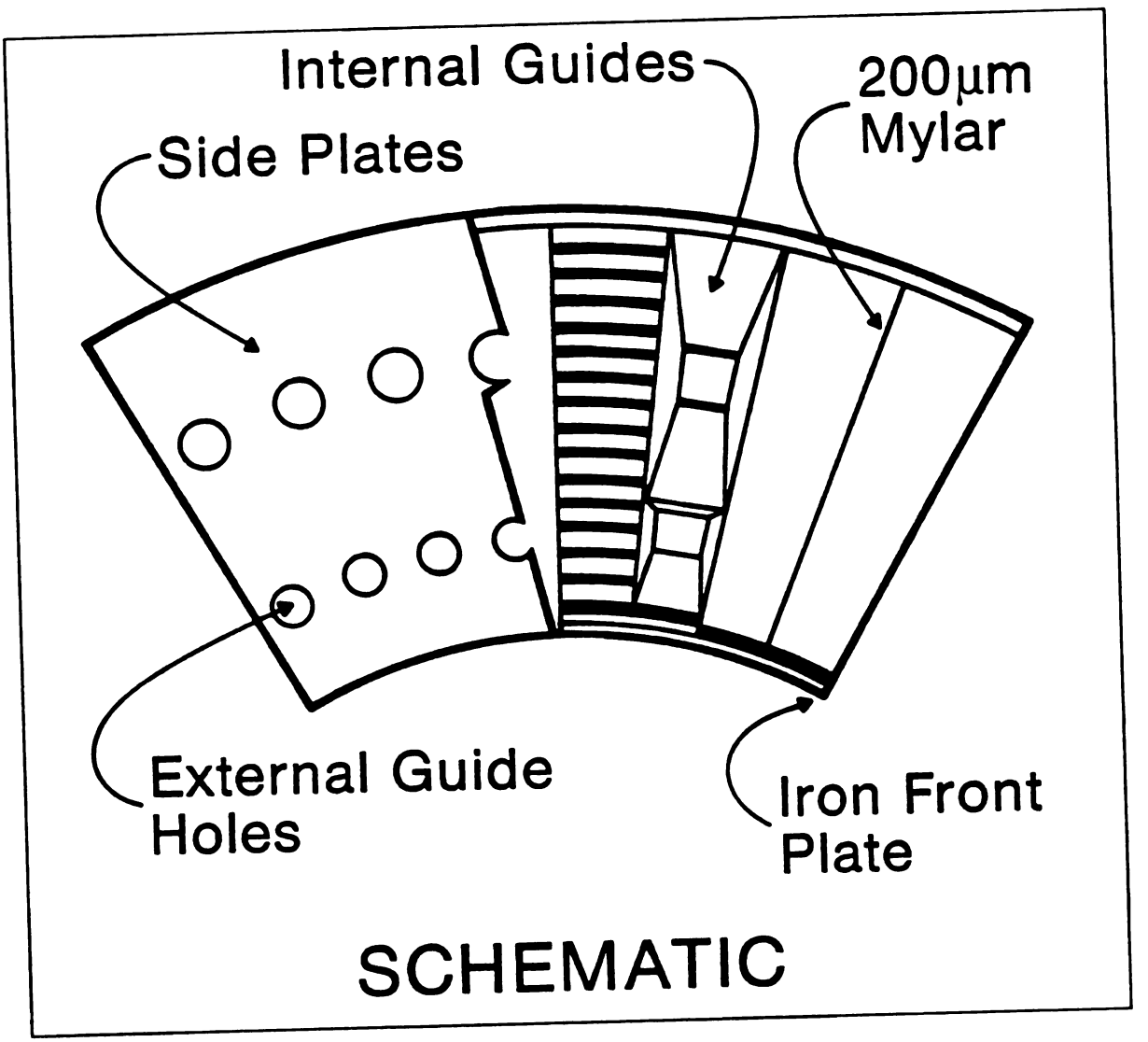

Figure 2.6: Shower counter modules

A Sh
lator
piece

was

teles

35mr

old

by le

show

2.3.6

In or

used.

at CE

count

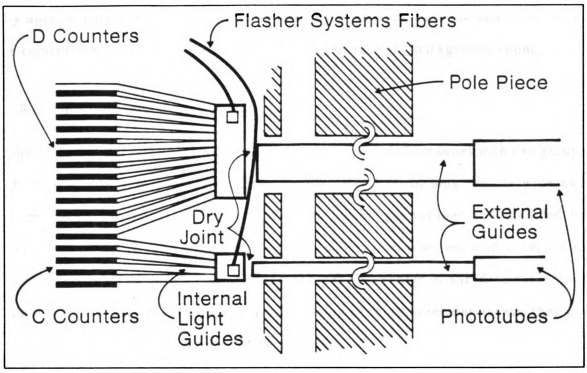

Figure 2.7: A shower counter segment

A Shower Counter Segment. Each segment was comprised of 16 layers of lead and scintillator. Internal light guides directed light through the shower counter box and the iron end piece to external light guides connected to phototubes.

was done by placing them close to the beam. These scintillation counters formed four telescopes pointing to the interaction diamond, where the beams cross, and start at 35mrad from the beam. Rates for the new counters were 200 times higher than the old MM counters. Measurements of h_{eff} by the old and new MM's usually differed by less than 2%. The beam curve as measured by the old and new MM counters is shown in figure 2.5.

2.3.6 L Counters

In order to monitor the beam condition a set of counters called the "L" counters were used. These scintillation counters were maintained and operated by the ISR division at CERN but a copy of the signal was supplied to the R110 counting room. The L counters were located in pairs about 10m upstream of the detector and were separated

by

A c

2.3

The

of t

1 cr

LeC

A co

these

very

2.3.8

There

sectio

7.5 cm

they c

deposi

muons

Cerenk

check.

2.3.9

The sho

(see figu

These se

the mod

by approximately 3m. Each counter was 25.5 cm long, 21 cm wide and 1 cm thick. A coincidence in a pair of the counters would generate one background count.

2.3.7 Y Counters

The "Y" scintillation counters covered the return yokes of the magnet with two groups of three counters on each yoke. Each counter was 120 cm long, 15 cm wide and 1 cm thick. The counters were connected to 56AVP phototubes and digitized by LeCroy 2249ADC's. The trigger of diagonally opposite Y counters with at least two A counters selected cosmic rays passing through the center of the detector. Since these cosmic rays have a track length twice a long as those in regular events, they are very useful in alignment of the drift chambers.

2.3.8 ST Counters

There was one "ST" scintillation counter located behind each back glass array (See section 2.3.10 for a discussion of the lead glass). These counters were 190 cm long, 7.5 cm wide and 1 cm thick, and were hung vertically. Provided with remote control they could be moved behind any column of the back glass array. A trigger on energy deposited in the ST counters gave a data sample with an enhanced proportion of muons and noninteracting pions. Since muons deposit a characteristic amount of Cerenkov light in the blocks of lead glass their signals could be used as a calibration check.

2.3.9 Shower Counters

The shower counters consisted of four modules each with eight segments 150 cm long (see figure 2.2). Each module covered 0.88 radians and was referred to as a sextant. These sextants were enclosed in a steel box (see figure 2.6). Segments making up the modules were comprised of a wedge-shaped sandwich of 16 layers of lead and

The
form.

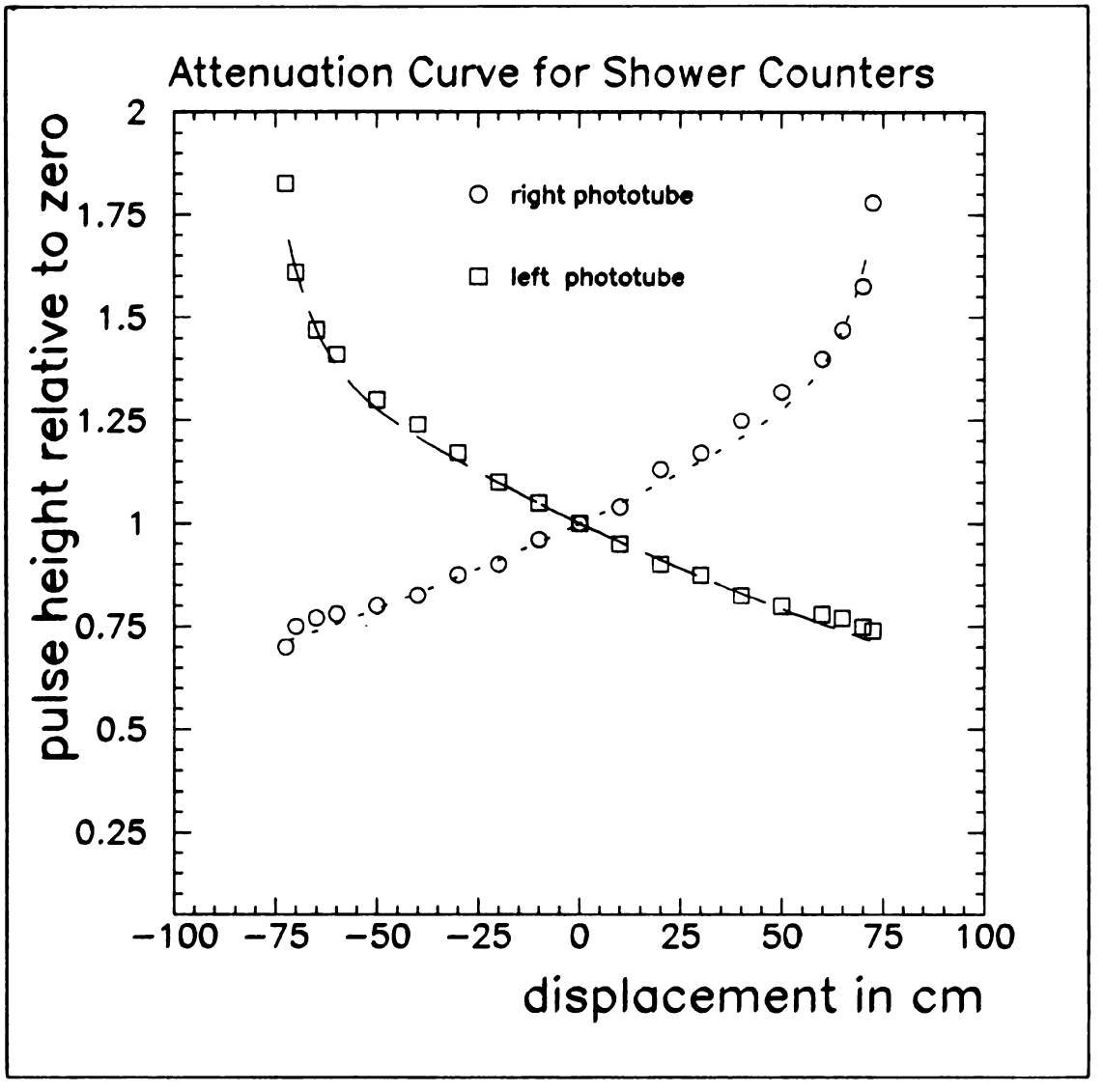

Figure 2.8: Attenuation curve for scintillator light

The attenuation curves for scintillator light in the shower counters have an exponential form.

Fraction
a functi

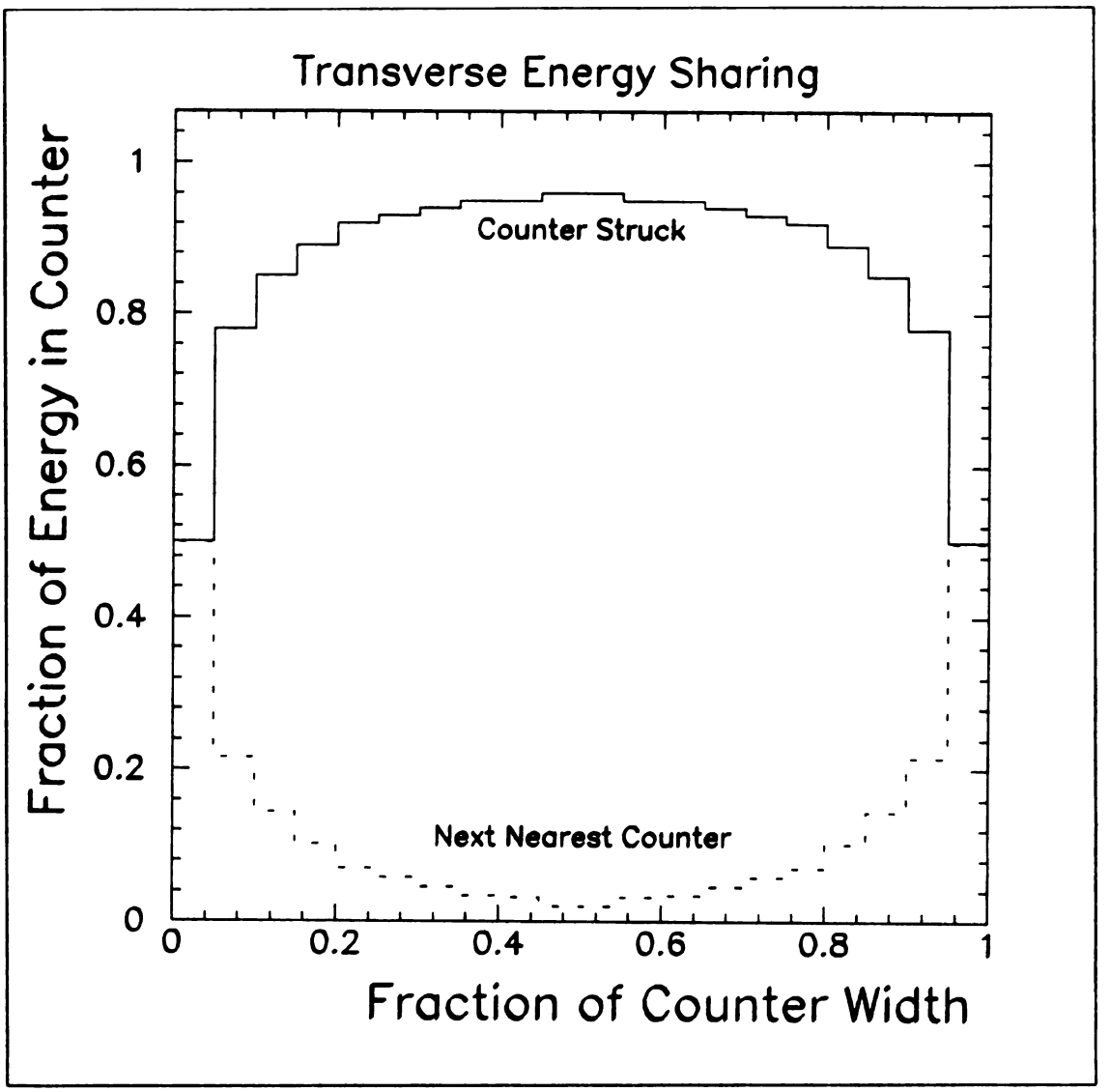

Figure 2.9: Energy sharing in shower counters

Fraction of energy a particle deposits in the counter struck and the next nearest counter as a function of its position in the counter.

scintillator (see figure 2.7). The lead layers were 0.5 cm thick and the scintillator layers were 0.43 cm thick. Each segment was individually wrapped in aluminum foil and separated from other segments by two layers of 100μm thick mylar. A 0.6 cm iron plate for the two upper modules and a 0.3 cm iron plate for the two lower modules provided support. Both ends of the scintillator layers were attached to internal light guides which grouped the first 4 layers into a "C counter" and the remaining 12 layers into a "D counter". Light guides 85 cm long protruded through the steel box and the iron end piece to the C and D phototubes outside the solenoid and its strong magnetic field. The connection of the internal light guides and the external guides was made through a dry joint maintained by mechanical pressure. Since both ends of a segment were read out, and there were two compartments per segment, a total of 32 phototubes was used per sextant.

The Flasher System

A "flasher system" was used in the calibration of the shower counters. The source of light for the flasher system came from EG&G KN22 krytron tubes. Since the spectrum was too low in blue light, a filter was used to shift the spectrum. A fixed fraction of this light was channeled into the C and D counters via optical fibers while another fraction was went to the "reference counter" phototube. Light that went to the shower counter was fed in independently at each end through light guides specifically shaped to mimic the light distribution expected for real particles.

Electrons and photons that struck the shower counters lost most of their energy in the counters. Typically the light generated in the scintillators is proportional to the energy of the incident particles. A consistency problem occurs when this light is converted to an electrical pulse by the phototubes. The pulse height is determined not only by the light reaching the phototube but also by the voltage supplied to the tube, the temperature of tube and the surrounding magnetic field as well as effects from

The
of i
the
Sinc
mod

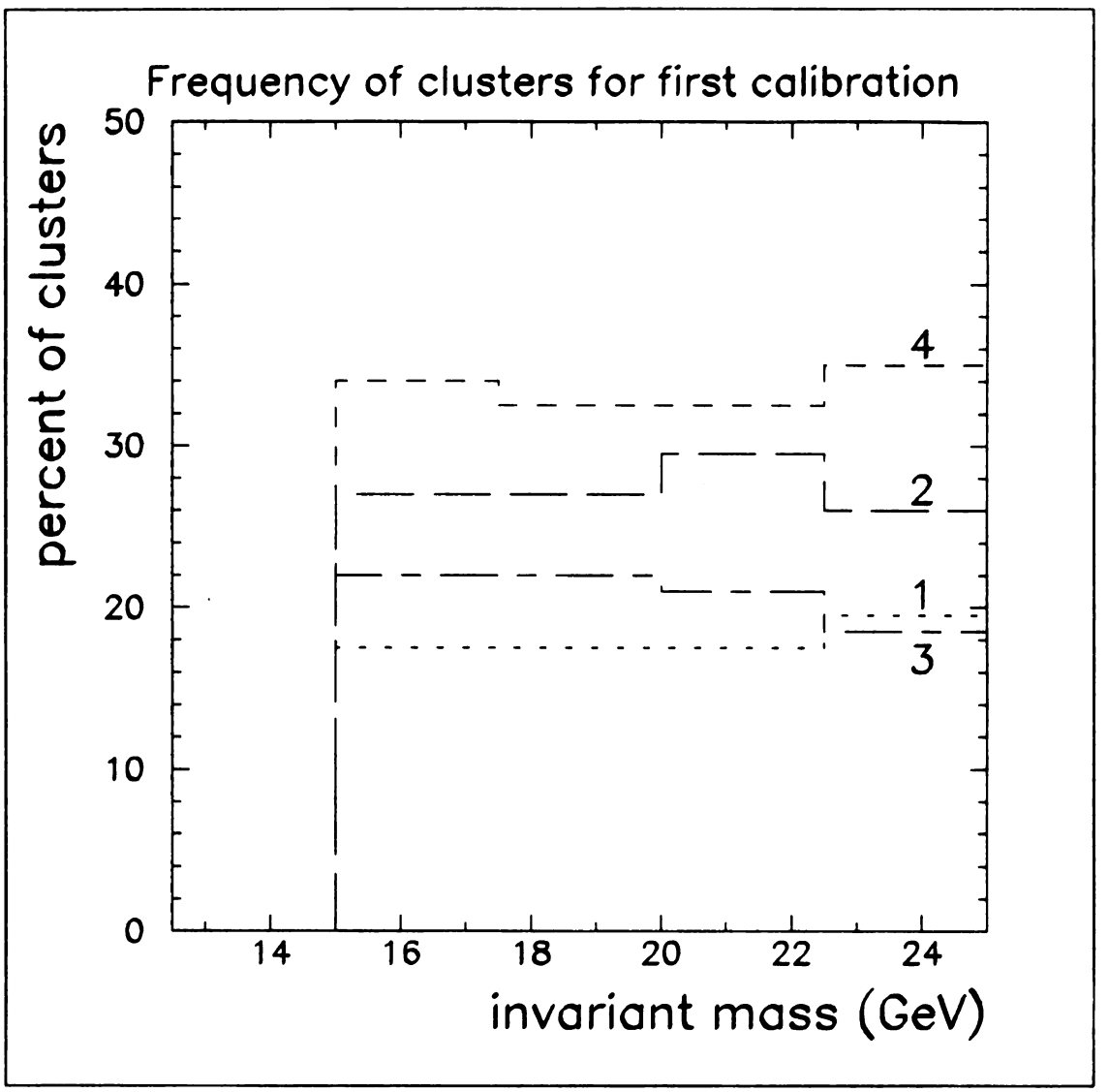

Figure 2.10: Cluster frequency for 1st calibration

The frequency of clusters in the shower counters for the four sextants is shown as a function of invariant mass using the original calibration constants. Both modules 3 and 4 are in the direction of the Lorentz boost and are expected to have the same frequency of clusters. Since modules 1 and 2 are away from the boost their frequency should be lower than both modules 3 and 4. This is clearly not true.

The fr
of inv
invari
modul

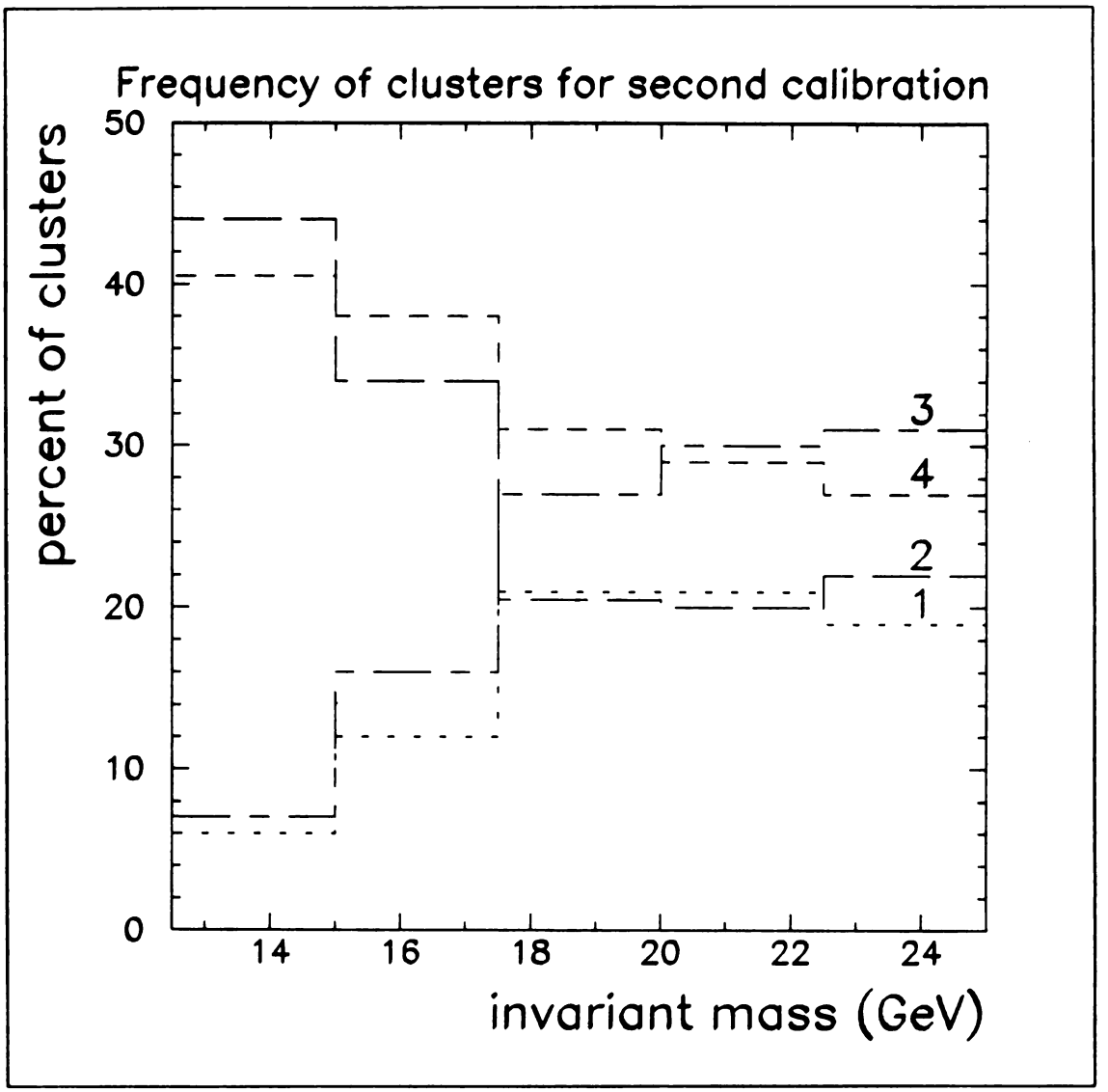

Figure 2.11: Cluster frequency for 2nd calibration

The frequency of clusters in the shower counters for the four sextants is shown as a function of invariant mass using the second calibration constants. At values significantly above the invariant mass threshold, modules 3 and 4 agree with a higher frequency of clusters than modules 1 and 2.

The a
iron p
thicke
than e

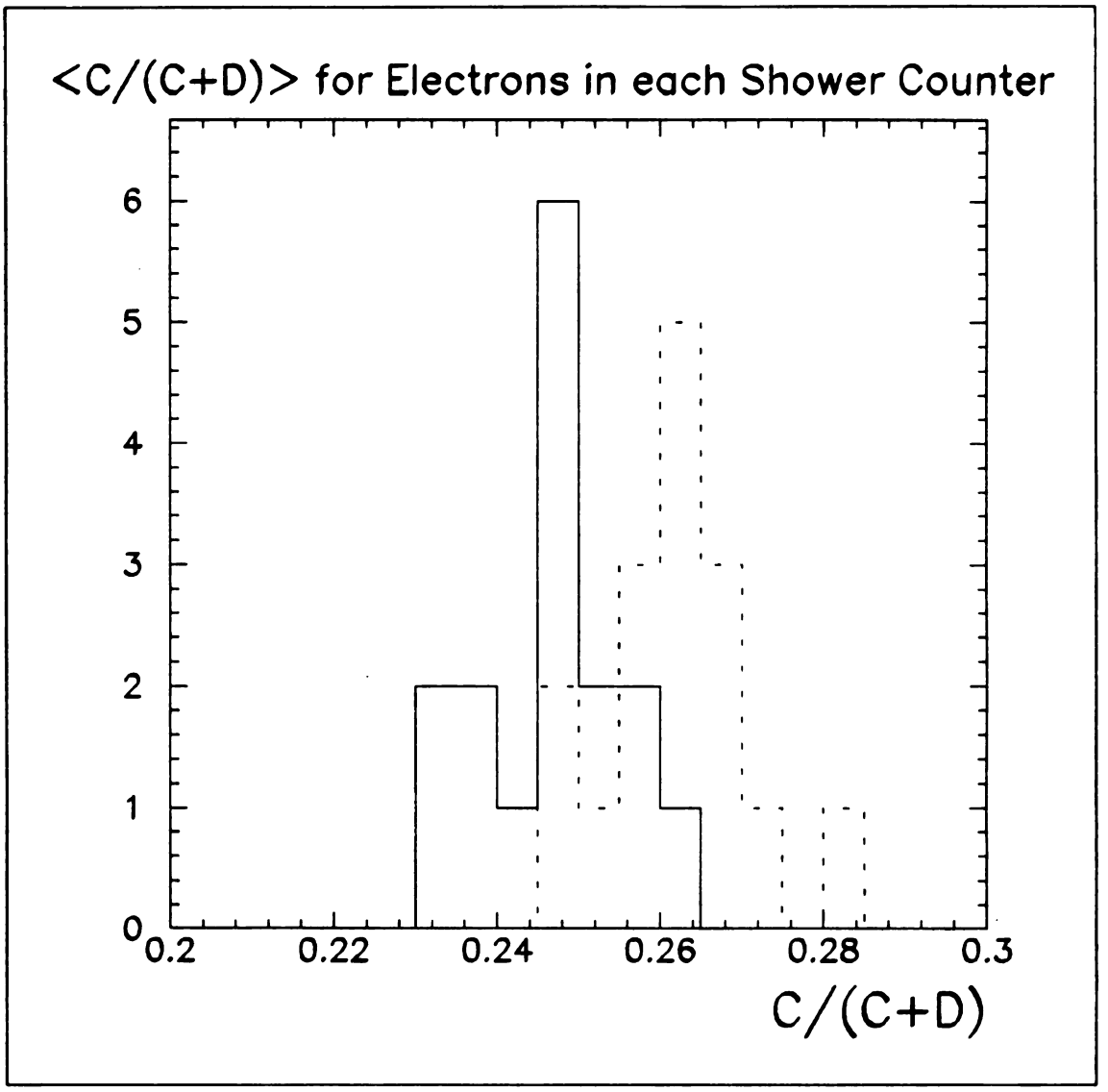

Figure 2.12: C/(C+D) for electrons

The average value of $C/(C+D)$ for the 16 lower shower counters (counters with a 3mm iron plate at the front) is shown plotted as the solid line. The upper counters which had a thicker 6mm iron plate is shown as a dashed line. The spread for sets of counter is larger than expected.

The di
shower
figure

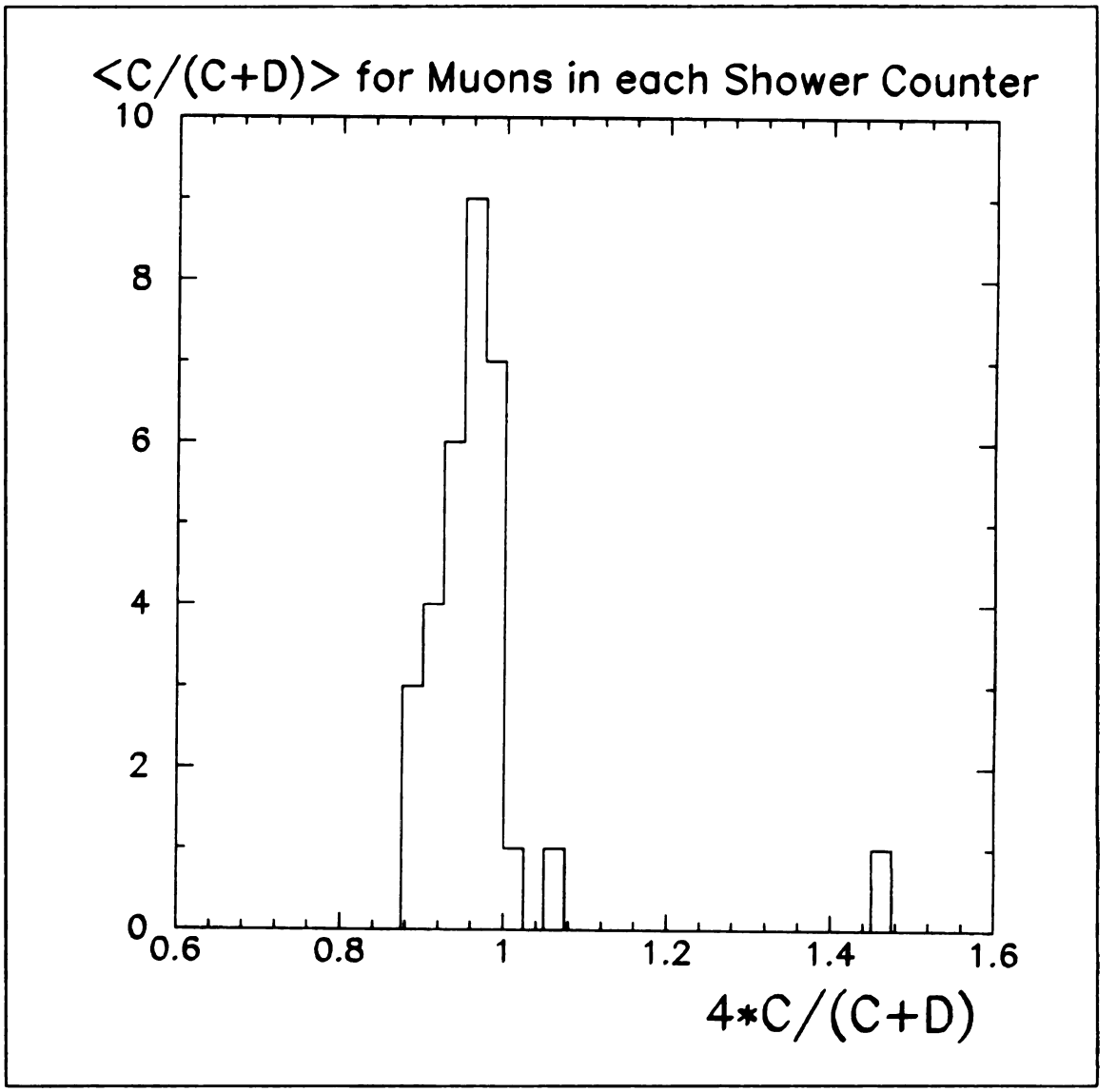

Figure 2.13: C/(C+D) for muons

The distribution of 4.0 C/(C+D) was found for muons. Since the total thickness of the shower counters is 4 times as thick as the C compartment the mean should be at 1.0. This figure shows the C counters were initially underweighted.

ageing. The method used to overcome this problem was to supply a known amount of light to the phototube through the flasher system. Since a fixed fraction of light went to the phototubes and the reference counter phototube the amount of light reaching the phototubes could be determined by measuring the pulse height at the reference counter phototube. The problem of consistency was thus shifted to reference counters. Again this problem was overcome by supplying a known amount of light. This time a sodium iodide crystal with an americium source provided a constant distribution of light to the reference counter phototube. The shower counters were calibrated in an electron beam at the PS. The NaI to flasher ratio in the reference counters and the flasher to 4 GeV electron ratio in each counter was found. The ratio of energy deposited in the C and D counters fluctuates from shower to shower. Advantage of this fluctuation was taken in order to find the correct balance of C and D counters, by minimizing the resolution of the total energy over a large number of showers subject to the constraint that the mean equal the energy of the incident particle.

A detailed position scan was made along one of the counters (see figure 2.8). The result was an exponential form for the attenuation curve for each end. For each of the other counters five positions were measured and its attenuation curve determined. The energy sharing between counters was determined by a scan across the width of a counter. Figure 2.9 shows the fraction of energy deposited in the counter struck by the particle and the next nearest counter. This information was used in both the analysis program and the Monte Carlo program.

Light leakage from the D to the C counters were also investigated by pulsing a light diode into the D counter light guides. Light that leaked into the C counters was measured to be less than 1 part in 1500.

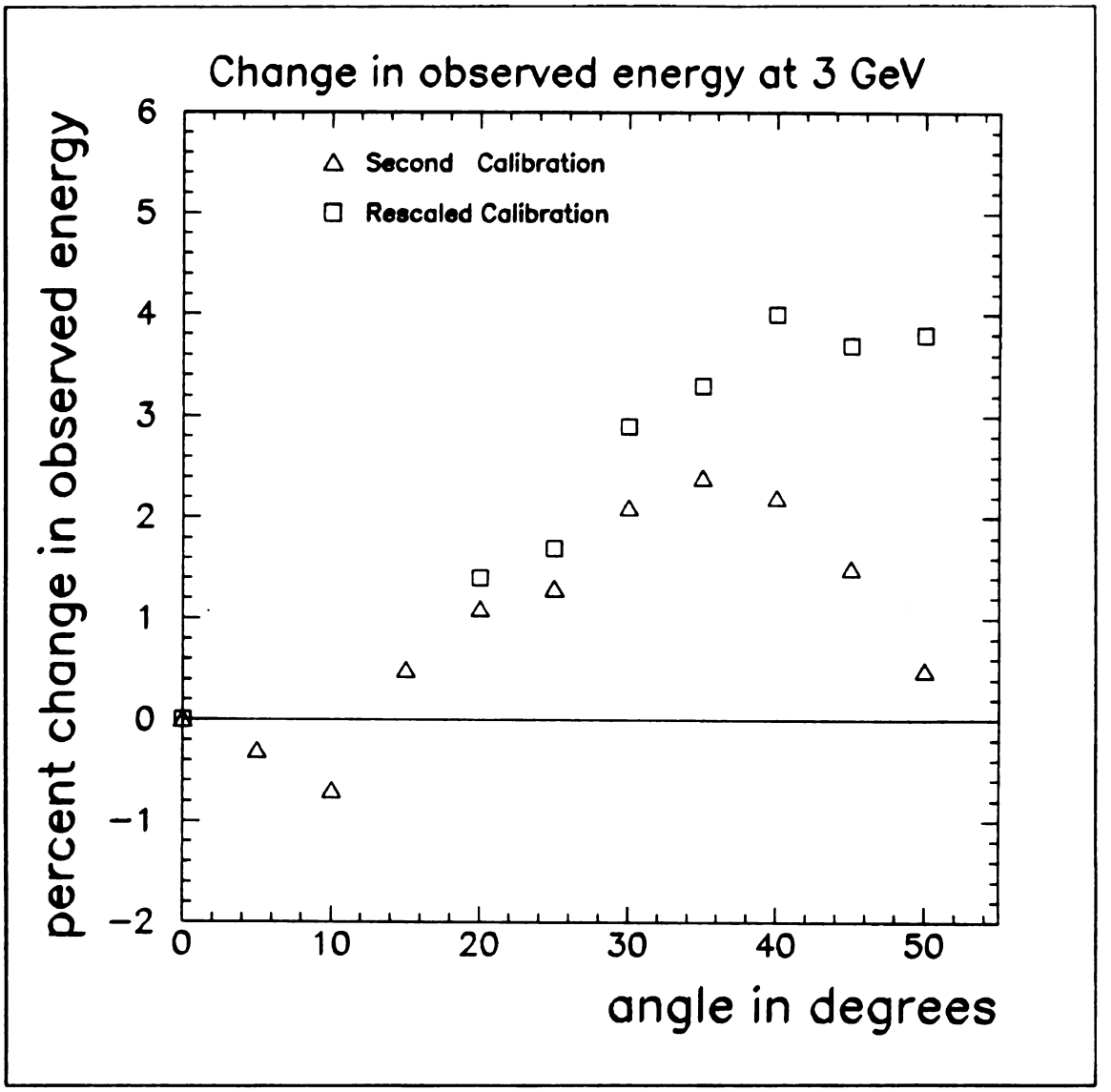

Figure 2.14: Percent change of observed energy in angle scan for 3 GeV electrons. A small amount of the shower leaks out the back of the shower counters for a normally incident particle. As one increases the angle of incidence the leakage is expected to decrease until the shower is completely contained. If the C and D counters are weighted correctly, the observed energy should rise until a plateau is reached. This is observed for the rescaled calibration, but not the second calibration. The drop in the second calibration would be explained if C counters were under-weighted.

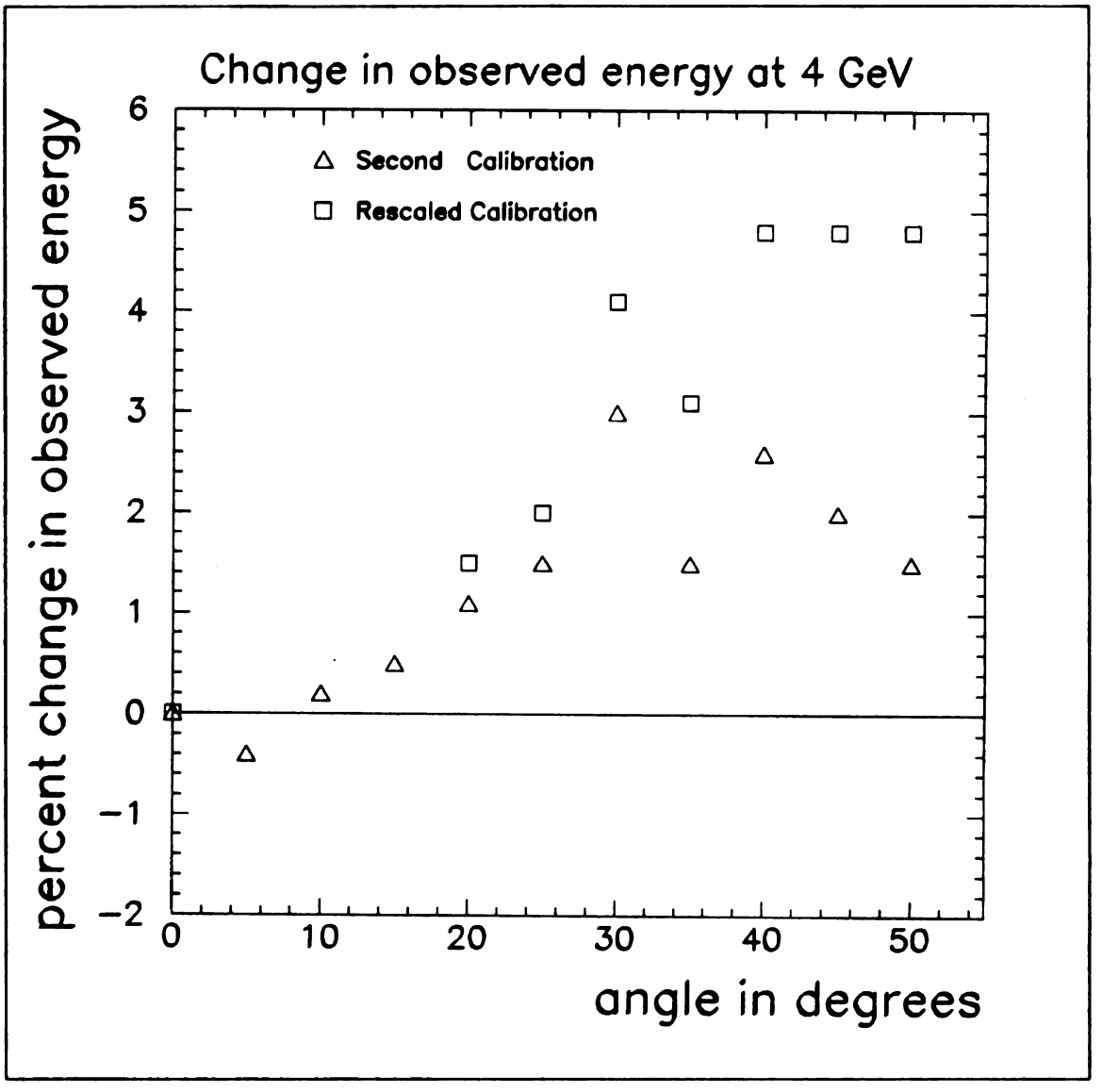

Figure 2.15: Percent change of observed energy in angle scan for 4 GeV electrons. The observed energy is expected to rise until reaching a plateau as the angle increases if C and D counters are weighted correctly.

Complications in the Calibration

The original calibration was performed in Sept 1979 at the PS in a 4 GeV beam of electrons. Data were then taken from Nov 1979 to Oct 1980. A second calibration was then performed from Oct to Nov 1980 which gave significantly different calibration constants. Some of the data taken between the calibrations required two clusters (see section 3.2.5) in the apparatus. The frequency of clusters in each sextant is shown in figures 2.10 and 2.11 as a function of the invariant mass. The inside sextants 1 and 2 (away from the Lorentz boost) were expected to be the same as were the outside sextants 3 and 4. The original calibration clearly disagreed with this reasoning while the second calibration was in agreement at the higher masses. Since the threshold for collecting the data was set using the original calibration the disagreement at the lower masses could be expected. The inaccuracy of the original calibration might have been due to the glue drying or the shower counters settling. It was known that external pressure on the counters could alter the observed pulse heights. After the calibration had been performed using the method of resolution minimization, the measured ratio of energy deposition in C counter to the total deposition (usually referred to as $C/(C+D)$) was found to disagree with the EGS Monte-Carlo predictions. It was also observed that the spread in $\langle C/(C+D)\rangle$ was large. Some of the counters differed from the mean by as much as 10%. The $\langle C/(C+D)\rangle$ ratio for the 4 GeV electrons is shown in figure 2.12 after calibration. The counters are split into two categories according to the thickness of the iron plate at the front of the counters. A third indication that the C counters were under-weighted came from the $\langle C/(C+D)\rangle$ ratio for muons (see figure 2.13). Since the amount of energy deposited by a muon is expected to be proportional to its track length $4\langle C/(C+D)\rangle$ should be equal to 1. Further evidence for under-weighting can be seen in figures 2.14 and 2.15 where the observed energy is shown as a function of the angle of incidence. One would expect the observed energy to increase with the angle until reaching a plateau (corresponding to maximum containment

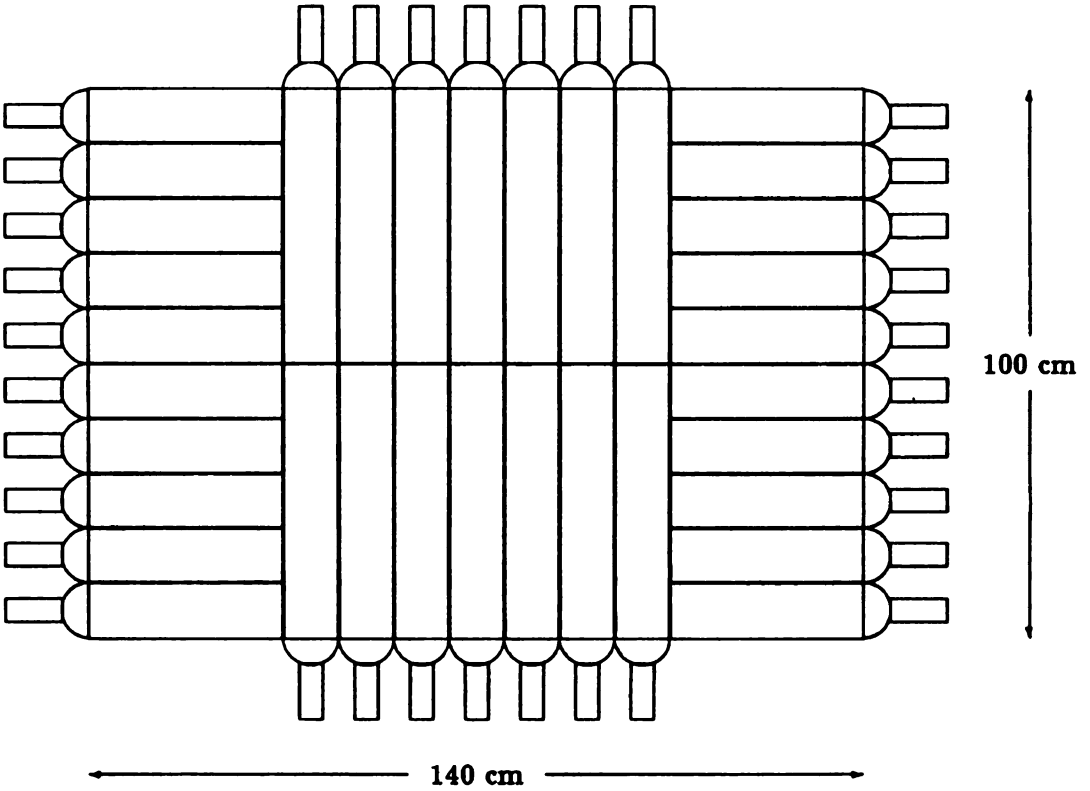

Figure 2.16: Front glass arrays

of the shower). Instead the energy is observed to increase and then decrease (the triangular points). By applying a renormalization equivalent to an 8% increase in the weighting of the C counter weight the data (now given by the square points) become consistent with the expected behavior. For more information see reference [10].

Table 2.3: Characteristics of lead glass SF-5.

Radiation Length	2.36 cm
Density	4.08 g/cm^3
Critical Energy	15.80 MeV
Threshold Momentum	0.38 MeV/c
Index of Refraction	1.67(at 5890 $\AA$)
Angle of Total Internal Reflection	36.8°

2.3.10 Lead Glass

There were a total of four lead glass arrays used in this experiment, a front and back array for each side of the detector. Because excessive radiation could cause yellowing in the lead glass, these arrays were mounted on a train and withdrawn from the interaction while the ISR rings were being filled. The arrays were made of blocks of

Table 2.4: SF-5 lead glass composition by weight.

SiO_2	39.2%
Na_2O	1.8%
K_2O	3.9%
PbO	55.1%

SF-5 glass manufactured by Schott Glaswerk. The characteristics of this glass are given in table 2.3 and its composition is given in table 2.4. For a discussion on the calibration of the lead glass the reader is directed to reference [11]

Front Glass

The front glass arrays consisted of 34 lead glass blocks which covered an area of 100 cm vertically by 140 cm horizontally (see figure 2.16). Each block had a width and thickness of 10 cm (4.2 radiation lengths). The length of the horizontal blocks was 35 cm, while those which extended vertically were 50 cm long.

Back Glass

The back glass consisted of a 12 × 14 array of 15 cm × 15 cm lead glass blocks (the 15 cm includes wrapping with aluminized mylar, soft iron foil and an outer mylar layer for electrical isolation) with a total height of 180 cm and a width of 210 cm (see figure 2.17). The length of each block was 40 cm except for the outermost blocks which were only 35 cm long. Each block had a five inch RCA 8055 photomultiplier tube glued to it using Kodak HE-10. The tube was surrounded by a μ-metal shield. Further protection from the fringe field of the solenoid was provided by an iron box with a front face 3 mm thick and sides 6 mm thick that enclosed the lead glass array.

2.3.11 Strip Chambers

The strip chambers were multi-wire proportional chambers (MWPC) which were sandwiched in between the front and back glass arrays. Each had an active area of 180 cm vertically by 210 cm horizontally. The two cathode planes, which were read out, enveloped the anode plane which was powered to 4.5 kV . There was a 1 cm separation between the anode and cathode planes. The anode plane was composed of 1000 gold-plated 20μm tungsten wires. Each wire was strung vertically with a 2 mm pitch and held at 3 places along its length by insulated support wire strung horizontally.

The cathode plane nearest the intersection region contained 160 cathode strips

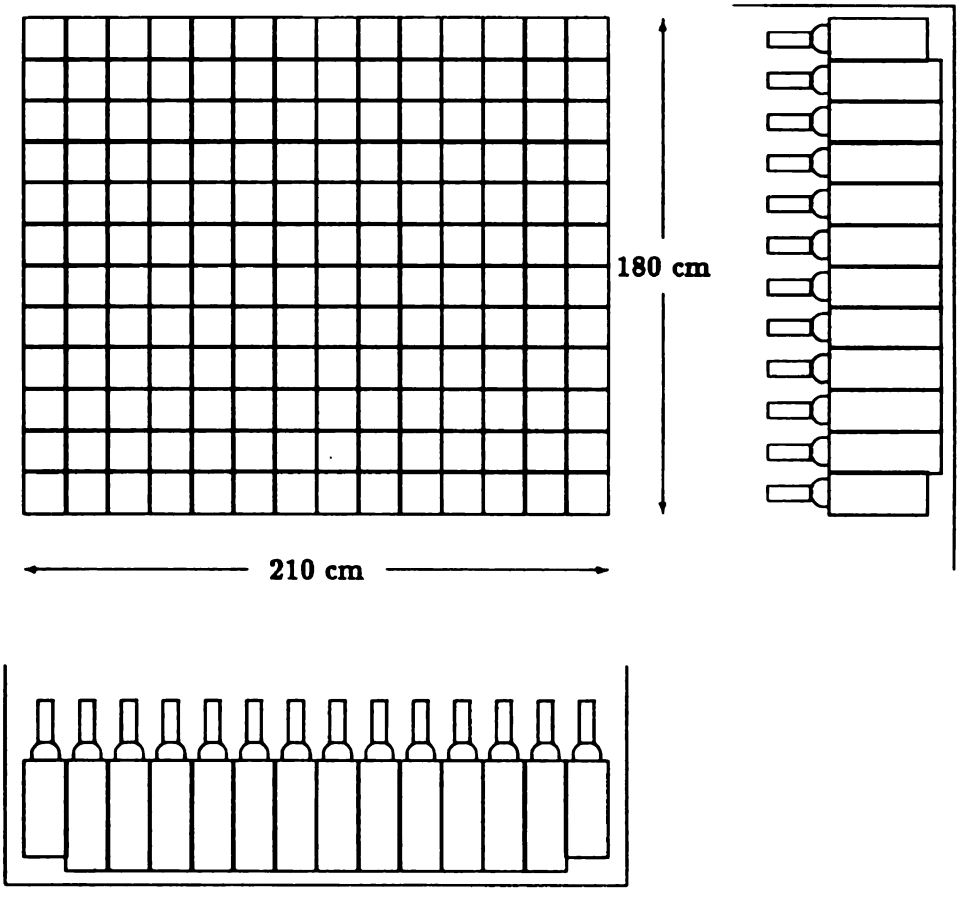

Figure 2.17: Back glass arrays

which ran horizontally, while the second cathode plane had 192 strips that ran vertically. This provided projections in y and z of the shower. The cathode strips were 0.8 cm wide, 35 μm thick copper etched on a 75 μm thick Kapton board with a regular spacing of one strip per centimeter (This included the 0.2 cm etched gap). The strip chambers were constructed of 0.9 cm thick styrofoam to which the cathode boards were glued. The gas used in the chambers was 70-30% mixture of argon and ethane with an additional 0.1% of freon [11].

Chapter 3

Event Selection

In this chapter the selection of events is described, starting with the trigger requirements and ending with final cuts of the analysis program.

3.1 The Trigger

The data were collected at the ISR starting from the beginning of 1980 and finally ending with the closing of the ISR in December 1983. In that time an integrated luminosity of 249 pbarns^{-1} were collected while an electron pair trigger was in operation. The data were collected on over 3000 raw tapes. Each raw tape held an average of about 7000 events. There were several triggers used during data taking, concentrating on different physics analyses. Triggers included the pairs trigger, the singles trigger, the glass pairs, double sextant, total energy, gamma inside and gamma outside.

3.1.1 Hardware Thresholds

The pairs trigger was used to collect the data of this thesis. Shower counter roads were defined as the sum of all eight phototubes of the C and D counters for two adjacent counters. Roads were not formed across sextants since there is a gap between the sextants. The formation of roads in the back glass was more complex, but was designed to select on energy concentrated in 3 $\times$ 3 block arrays. Up to six roads per

glass sextant could be formed. The requirement for the pairs trigger was two roads with more energy than a given threshold in two nonadjacent sextants. Furthermore, the total energy of these two roads was greater than a second threshold.

3.1.2 Software Filter

In addition to the trigger cuts, events were subject to filter requirements as well. For the shower counters, each sextant's road energy was calculated as the maximum two-counter combination, with the energies corrected for the z position. In the glass sextants, the software road energy was the maximum of the six hardware roads.

At least two roads were needed to pass the pairs filter. If four or more roads passed the roads filter the event was accepted. Otherwise the event must have some combination of non-adjacent sextants with roads passing the roads filter cut and the mass calculated from the two energies and the opening angle must be above the mass cut.

3.2 Cuts on the Data

There were three types of tapes which were handled by SOX, the R108-R110 analysis program. The first was the RAW tapes written by the on-line HP computer during runs at the ISR. The second was the DST (Data Summary Tape) which was a result of processing the RAW tapes using SOX. The format of the DST was such that when parameters were changed, e.g. calibration constants, it was sufficient to have a DST type tape as input to SOX to produce a new DST type output tape.

The third type was the CON tape, which uses a condensed format. On CON tapes many of the direct measurements of the detector were replaced by higher level values. For example, the readout from the wires in the drift chambers was replaced by a list of track vectors and vertices.

3.2.1 RAW to DST

One of the advantages of converting RAW tapes to DST was the reduction in the number of tapes for a given analysis. This was because, when making a DST, usually events passing only a single trigger were considered whereas a RAW tape usually contained events from several triggers. Since calibration constants were known better at the DST level, some cuts could also be tightened.

3.2.2 DST to CON

Further reductions were made in the number of tapes when converting to CON tapes. Since the analysis program that used the CON tapes ran many times on the same data it was useful to have a large number of events on a single tape.

3.2.3 Good Electron Pair Candidates

The analysis program began each event by looping over the tracks. If the track was found to be good then an attempt was made to build a cluster where the track struck the shower counters. If there were two good tracks with good clusters then the event was considered an electron pair candidate. Table 3.1 lists the requirements for a good cluster and track and the number of events passing. The data were broken into four sets and were taken at different times.

3.2.4 Good Track Requirements

A track must have passed six requirements in order to have been considered a good track. First, in order that the measurement of the momentum from the track be reasonable, six points in the drift chambers were required. The track must have come within 5 cm of the z axis and its point of closest approach must have had an absolute value in z of less than 50 cm. This insured the track had passed through the interaction region. Tracks with momentum less than 1.5 GeV/c were discarded. A

Table 3.1: List of cuts

Cut Description	Old 80 Data	Old 81 and 82 Data	New Half Back Data	New Normal Geo. Data
Events passing preliminary filter	6841	5822	6886	4596
Tracks passing preliminary filter	83475	68910	82704	55667
Good Track Cuts				
number of tracks with more than 6 hits	66114	52352	63000	43412
tracks that come within 5 cm of z axis	55844	44242	52718	36886
track's closest approach to origin has a $z < 50$ cm	55797	44216	52674	36886
$p_{\text{track}} > 1.5$ GeV	18618	14548	16999	11744
χ^2/dof of track fit< 5.0	16617	12139	14237	10003
Web	16615	12136	14236	10002
Good Cluster Cuts				
track strikes shower counters	15591	11316	13283	9248
$E_{\text{seedcounter}} > 1.0$ GeV	14520	10504	12362	8671
$\lvert z_{\text{track}} - z_{\text{seed}} \rvert < 20$ cm	13559	9608	11310	7917
cluster < 3 counters wide	11763	7551	9203	6368
$E_{\text{cluster}} > 4$ GeV	9801	6066	7624	5247
$\lvert \phi_{\text{track}} - \phi_{\text{cluster}} \rvert < 0.06$ rad	7320	4075	5196	3533
$\lvert z_{\text{track}} - z_{\text{cluster}} \rvert < 15$ cm	6952	3724	4742	3255
number of events with at least 2 good tracks	1965	650	857	631
number of events with two good tracks pointing at nonadjacent sextants and $M_{ee} > 11 GeV$	715	263	442	301
X≡ number of events with $E_{\text{electron}_i} > 4.5$ GeV	615	229	369	259
Luminosity (pico barns)	102	40	66	41
X / Luminosity (events/pb)	6.0 ± 0.2	5.7 ± 0.4	6.0 ± 0.3	6.3 ± 0.4

further track quality cut was placed on the confidence level of the least-squares fit to the track (χ^2 per degree of freedom required to be less than 5). Finally tracks that struck the supports for the chamber were also removed.

3.2.5 Good Cluster Requirements

If an event had a good track and struck the shower counters, an attempt was made to construct a cluster around the position of the struck counters (see Table 3.1). Before a cluster was built a seed counter was found: the counter hit by the track if the counter had at least $1GeV$ or this failing, the next nearest counter to the track if it had at least 1 GeV. The cluster was then expanded outward until a counter was found to have had less than 50 MeV, a z position more 20 cm from the track's z position or more energy than the previous adjacent counter added to the cluster. If the cluster expanded in this manner was more than 3 counters wide it was discarded as an electron candidate along with the corresponding track. Thus a cluster consisted of from 1 to 3 counters, each with a z position that matched the z of the track to within 20 cm, and at least 50 MeV of energy. This cluster was also required to have had an energy weighted ϕ within 0.06 radians from the track's ϕ.

An energy weighted z was calculated for the cluster. Unlike the energy weighted ϕ, only counters with at least 1 GeV were used. The z for the track was always calculated at a radius of 60 cm from the z axis, which corresponded to the average position for showers with normal incidence. At normal incidence, the average depth at which energy was deposited in the shower counters is 5.8 cm. Since this depth would decrease as $\sin\theta$, where θ was the angle between the z axis and the particle track, z was extended by

$$\delta z = \frac{5.8}{\tan\theta}(1 - \sin\theta) \tag{3.1}$$

for a better comparison with the track. The corrected z of the cluster and the track were required to have agreed to within 15 cm. One further requirement for a good

cluster was that the cluster energy be greater than 4 GeV.

3.2.6 Two Good Matching Clusters & Tracks

When a good track and matching cluster was found, a four momentum was formed for the electron candidate, assuming the candidate was massless and had an energy equal to the cluster energy. The direction of momentum was taken to be along the vector from the event vertex to the center of gravity of the cluster. Since the tracks of particles greater than 4 GeV were nearly straight this was reasonable even considering the solenoidal magnetic field. The four momenta for the candidates were then translated from the lab frame to the center-of-mass of the colliding protons. Events were rejected if they did not have a least two electron candidates with energy greater than 4.5 GeV, with showers in nonadjacent sextants. The mass found from the vector sum of the two candidates was required to be greater than 11 GeV, to reject Υ decays.

3.2.7 The Background Estimate

Events that had good tracks and matching clusters were classified as n_{++}, n_{--} or N_{+-} where the sign is given by the charge measured from the track. Drell-Yan events were of opposite sign while background events could have been either same sign or opposite sign. By making the assumption that the charge of a track for background events did not depend on the charge of the other member of the pair the expected background in the opposite sign events was found. First we make the following definitions.

Table 3.2: The final cuts

Cut Description		Old 1980 Data	Old 1981 & 1982 Data	New Half Back Data	New Normal Geo. Data
Events with two good tracks pointing to non-adjacent sextants with with $E_{electron} > 4.5$ GeV and $M_{ee} > 11$ GeV	all	615	229	369	259
	N_{+-}	331	117	186	136
	n_{++}	218	80	124	90
	n_{--}	66	32	59	33
	Signal	91 ± 43	15 ± 27	15 ± 34	27 ± 28
Vertex Cut $\Delta_v xy < 1.3$ cm	all	518	180	272	198
	N_{+-}	289	92	139	107
	n_{++}	181	62	88	64
	n_{--}	48	26	45	27
	Signal	102 ± 39	12 ± 24	13 ± 29	24 ± 24
Vertex Cut $\Delta_v z < 2.5$ cm	all	514	180	270	197
	N_{+-}	285	92	137	107
	n_{++}	181	62	88	63
	n_{--}	48	26	45	27
	Signal	102 ± 39	12 ± 24	11 ± 29	25 ± 24
Momentum Energy Equality Cut -0.10< α <0.38	all	381	115	178	123
	N_{+-}	219	63	94	68
	n_{++}	136	34	52	43
	n_{--}	26	18	32	12
	Signal	100 ± 32	14 ± 18	12 ± 23	23 ± 19
Longitudinal Energy Deposition Cut $0.10 < \frac{C}{C+D} < 0.42$	all	215	70	92	71
	N_{+-}	134	43	54	45
	n_{++}	67	20	26	18
	n_{--}	14	7	12	8
	Signal	73 ± 23	19 ± 14	19 ± 16	21 ± 14
Transverse Energy Deposition Cut $R_e > 0.93$	all	157	53	63	48
	N_{+-}	110	34	40	34
	n_{++}	40	14	15	8
	n_{--}	7	5	8	6
	Signal	77 ± 19	17 ± 12	18 ± 13	20 ± 10
Invariant Mass Cut $m_{eT} > 0.145 GeV$	all	134	46	56	39
	N_{+-}	98	30	36	30
	n_{++}	31	12	15	7
	n_{--}	5	4	5	2
	Signal	73 ± 17	16 ± 11	19 ± 12	23 ± 9
Isolation Cut $p_J < 1.3 GeV$ with half angle cone size of 25°	all	59	19	26	16
	N_{+-}	54	16	22	16
	n_{++}	5	2	3	0
	n_{--}	0	1	1	0
	Signal	54 ± 7	13 ± 6	19 ± 7	16 ± 4
Minimum Depth Cut	all	57	16	26	16
	N_{+-}	53	14	22	16
	n_{++}	4	2	3	0
	n_{--}	0	0	1	0
	Signal	53 ± 7	14 ± 4	19 ± 7	16 ± 4

n_{++} ≡ number of events with two positive tracks
n_{--} ≡ number of events with two negative tracks
N_{+-} ≡ number of events with a negative and a positive track
all ≡ $N_{+-} + n_{++} + n_{--}$
p ≡ probability that a track will be positive
S ≡ Drell-Yan signal
B ≡ total number of background events
n_{+-} ≡ number of background events with opposite sign

It can be seen that

$$n_{++} = Bp^2 \tag{3.2}$$

$$n_{--} = B(1-p)^2 \tag{3.3}$$

$$n_{+-} = 2Bp(1-p) \tag{3.4}$$

$$= 2\sqrt{n_{++}n_{--}} \tag{3.5}$$

and thus the Drell-Yan signal was

$$S = N_{+-} - n_{+-} \tag{3.6}$$

$$= N_{+-} - 2\sqrt{n_{++}n_{--}}. \tag{3.7}$$

3.2.8 Final Event Selection

After the cluster requirements were made, the remaining events were mostly a combination of true electron pairs, π^0s with overlapping charged tracks, and a few Dalitz decay events. The final cuts were used to select electron pairs with as few π^0s, overlaps, etc. as possible. Table 3.2 list these cuts in the order they were applied, along with the number of N_{+-}, n_{++} and n_{--} events that passed the cut. Also given are the total number of events that passed and the signal as defined in the previous section.

Vertex Cuts

To insure that the tracks had a common vertex, the distance of closest approach of the two candidate electron tracks was required to be within 2.5 cm in the z direction.

The higher resolution in the xy plane allowed the tighter cut value of 1.3 cm for Δxy. This cut did little to enhance the signal over the background but was nevertheless expected of the true electron pairs.

Momentum-Energy Equality

The variable α

$$\alpha = \left(\frac{E_{\text{cluster}}}{p_{\text{track}}} - 1 \right) \frac{1}{E_{T\text{cluster}}} \tag{3.8}$$

was used to match the energy of a cluster with the momentum of the track pointing to it. For a perfectly measured electron α would have been zero. Because of resolution α had some distribution about zero. The resolution is dominated by the measurement of the momentum which is inversely proportional to the transverse momentum, hence the $1/E_{T\text{cluster}}$ factor.

A major source of background came from a track produced by a charged hadron pointing to a cluster produced by a γ from a π^0 decay. Because the energy threshold was high, these events usually had an α greater than zero. Single charged hadrons rarely deposit all their energy in the shower counter, so their α's would usually be less than zero. Figure 3.1 shows the distribution of α for electron candidates without any of the final cuts. The α cut was effective at removing background, but also removed some of the signal.

Longitudinal Energy Deposition

The C/(C+D) was found by dividing the energy deposited in the front C counters by the total energy of the cluster. A cut on this quantity was useful because the mechanism for energy deposition of electromagnetic showers from electrons and photons is very different from that of hadrons. Electromagnetic showers proceeded as a cascade with electrons that produced photons through bremsstrahlung radiation, and photons that created electrons through pair production. These showers usually

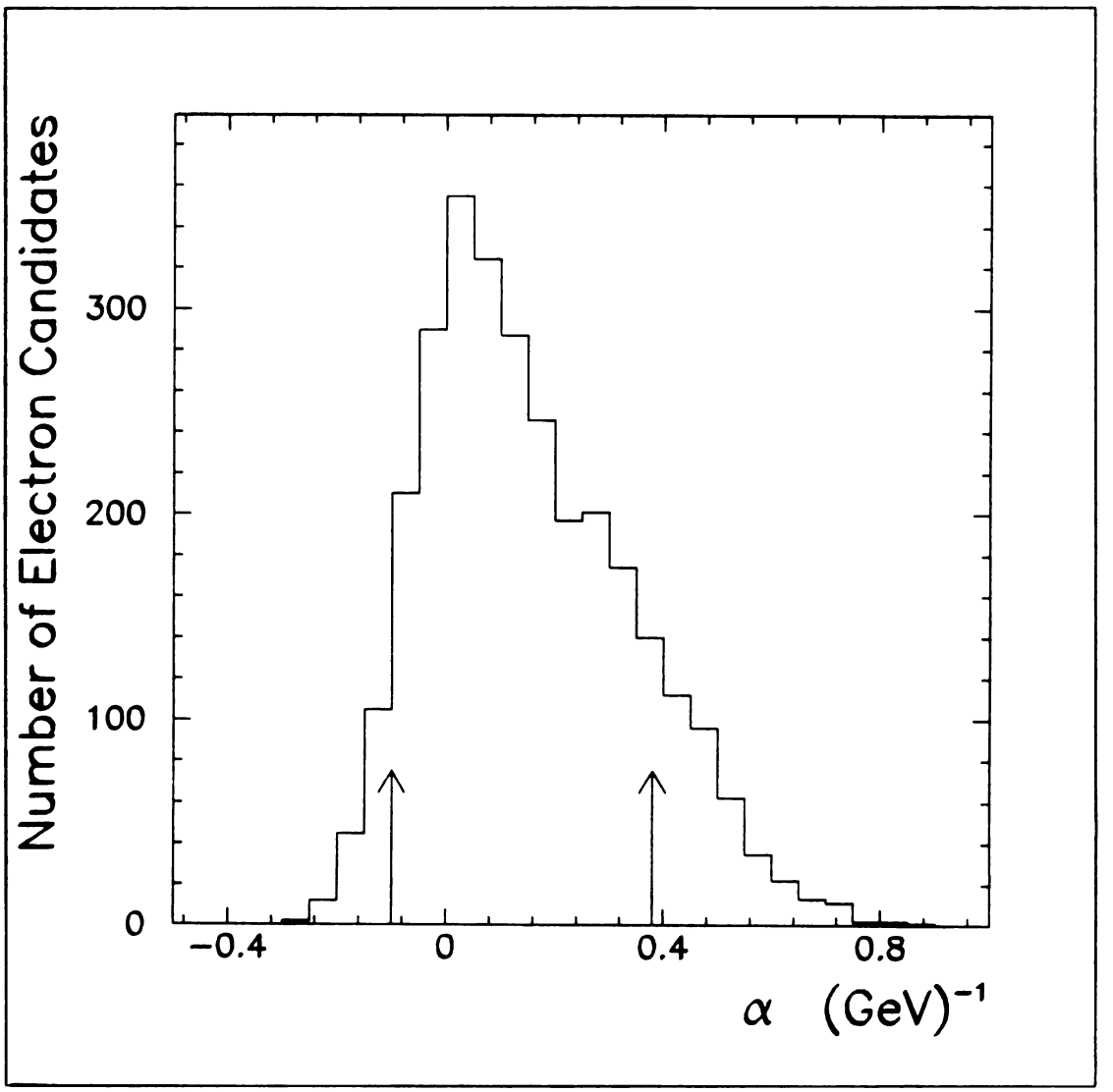

Figure 3.1: The α distribution

The distribution was from events with two good clusters and matching tracks. The arrows show where the low and high cuts were made.

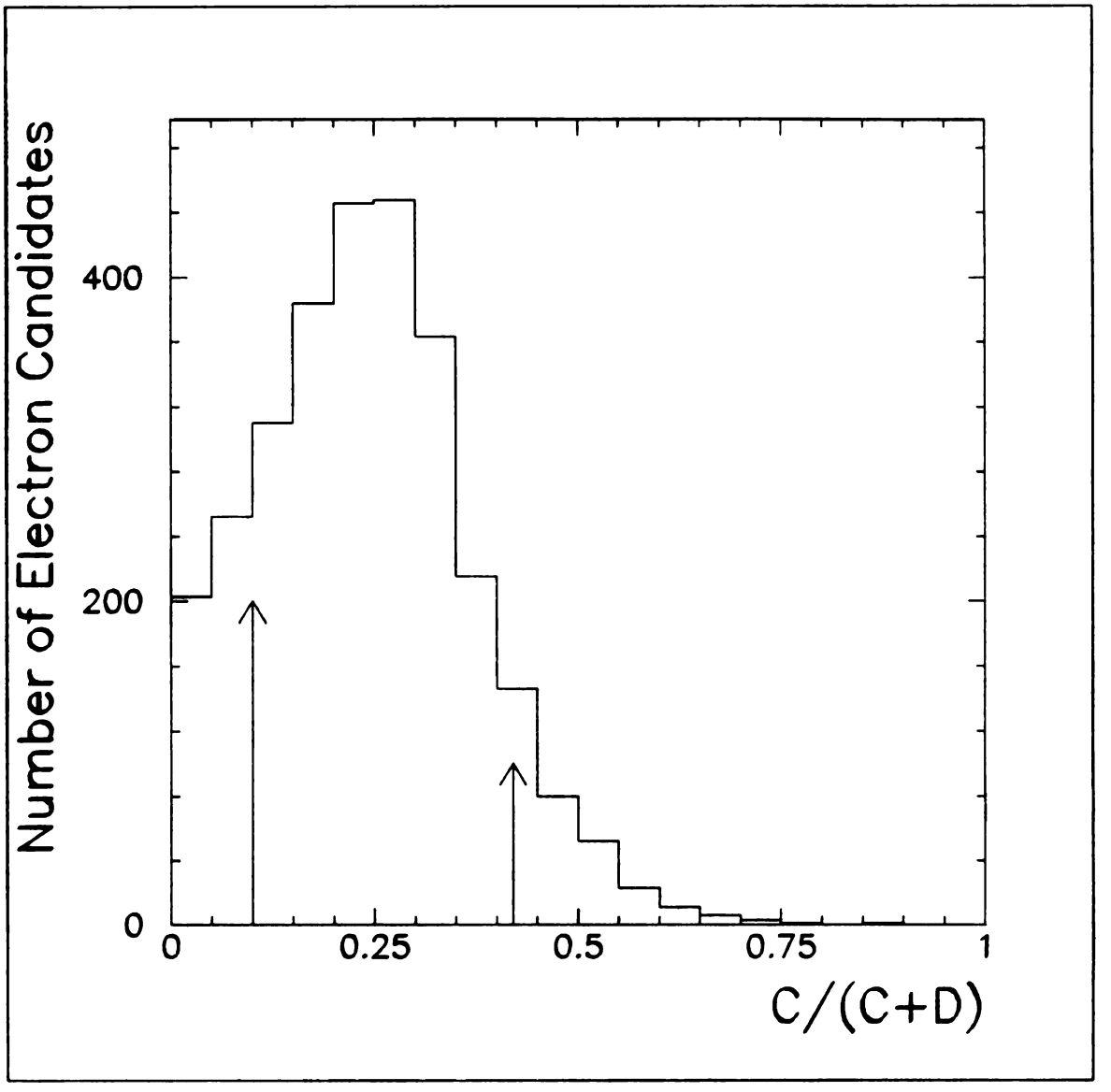

Figure 3.2: The C/(C+D) distribution

The distribution was from events with two good clusters and matching tracks. The arrows show where the low and high cuts were made.

started early in the shower counters, consisted of many particles and had a uniform shape. Hadronic showers were usually initiated from an interaction with a nucleus. These showers usually started later and were not contained in the shower counters. Therefore a cut on low C/(C+D) removed some of the charged hadronic background (see figure 3.2).

Overlaps of charged tracks with neutral particles, typically $\pi^0 s$, can produce clusters with large values of $C/(C+D)$. These clusters were removed with a cut on high $C/(C+D)$.

Transverse Energy Deposition

EGS3 Monte Carlo studies of the transverse spread of the electron showers in the shower counters showed that on average over 96% of the energy was deposited in only two counters in the cluster. The quantity R_c was defined as the ratio of energy in the two counters nearest the track over the energy of the cluster. Clusters in background events tended to be spread over several counters and therefore had lower R_c values. The distribution of R_c is shown in figure 3.3 before any of the final cuts were made. The R_c cut significantly enhanced the signal with high cut efficiency.

Invariant Mass Cut

One source of background was from Dalitz decays of π^0 which gave real electron-positron pairs. These events were removed by cutting on the invariant mass found by combining the four momentum from the candidate track with the four momentum of any other track in the event. The quantity m_{eT} for the candidate track was the smallest mass that could be formed from any of the tracks. Dalitz decays were removed by requiring that m_{eT} be greater the the π^0 mass (see figure 3.4).

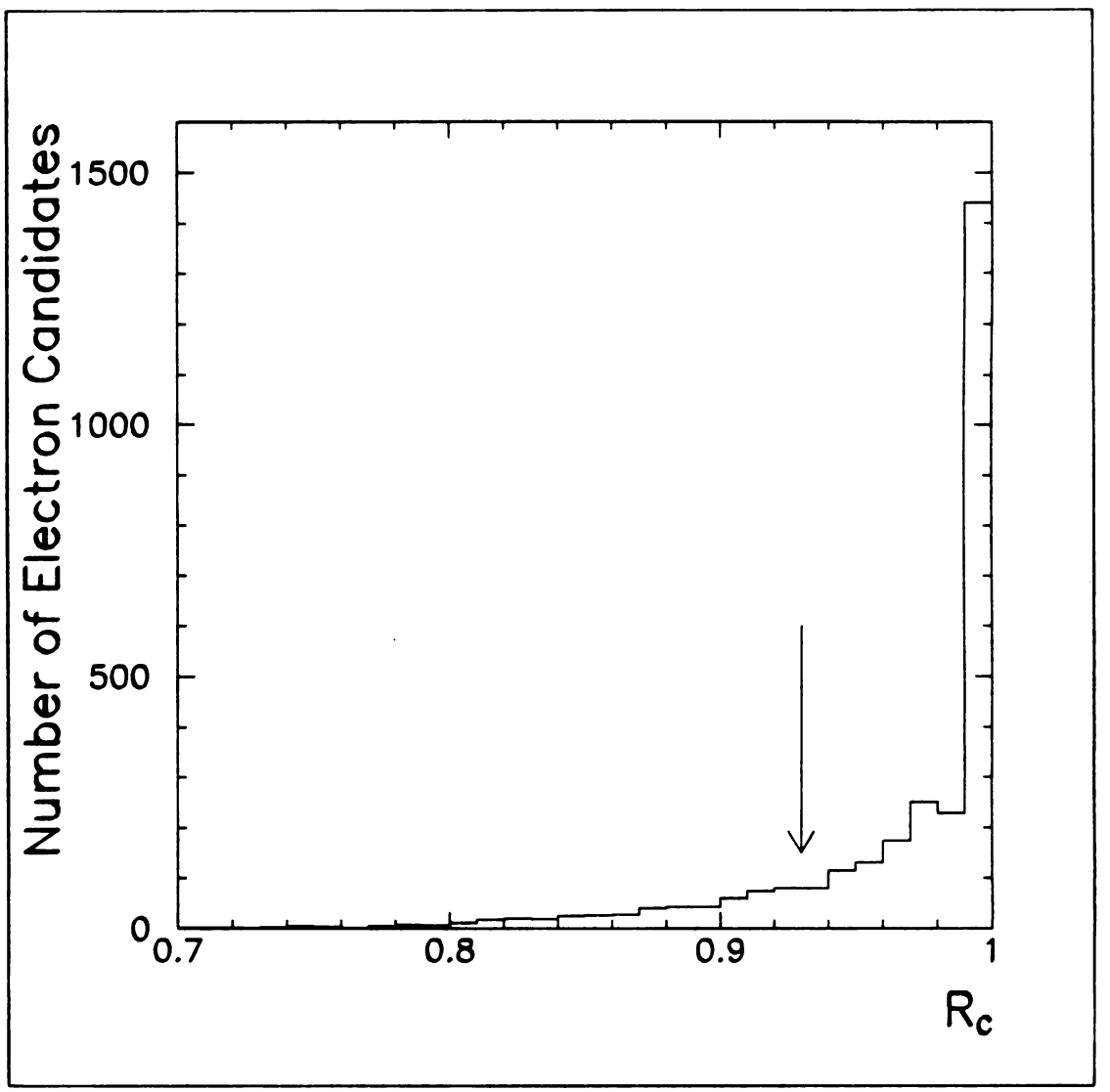

Figure 3.3: The R_c distribution

The distribution was from events with two good clusters and matching tracks. Only events with both R_c values above the arrow passed this cut.

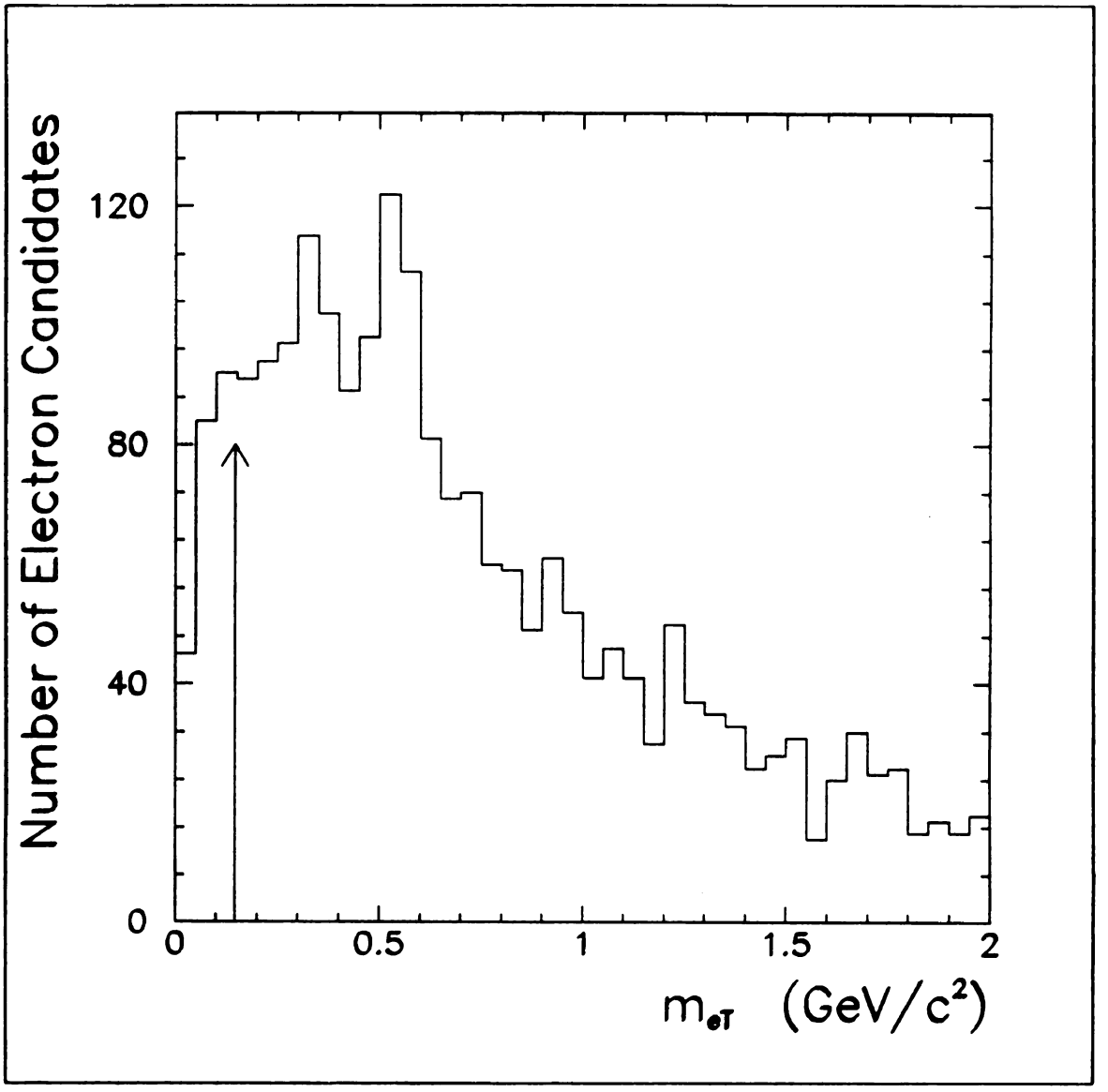

Figure 3.4: The m_{eT} distribution
The distribution was from events with two good clusters and matching tracks. Events to the left of the arrow were rejected.

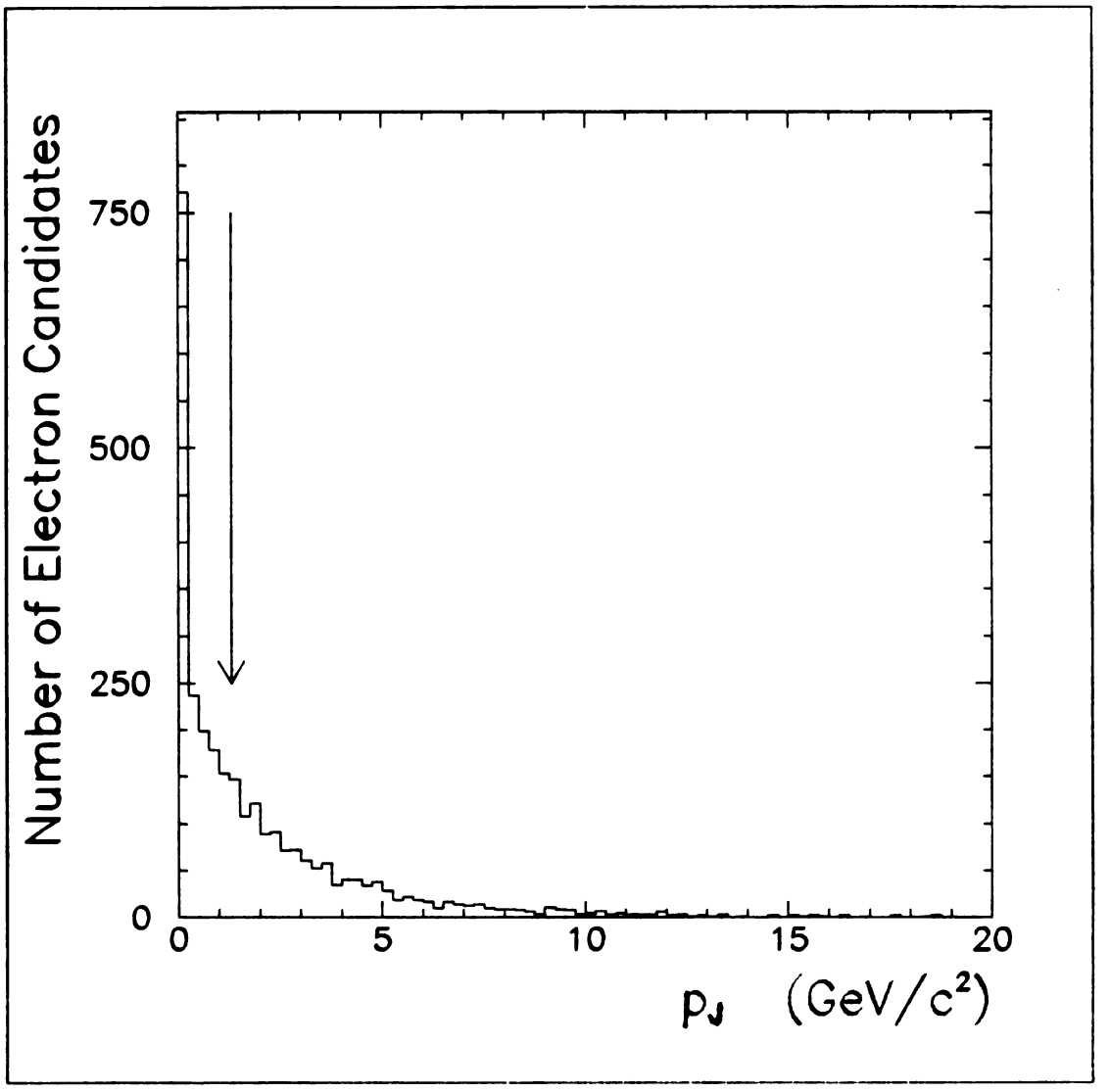

Figure 3.5: The p_J distribution

The distribution was from events with two good clusters and matching tracks. Events with entries to the right of the arrow failed were rejected.

Isolation Cut

A source of further background came from jet-like events composed of collimated charged and neutral particles. To determine if the candidate track was a member of a jet, the momentum from all particles within a 25° cone were projected onto the candidate track and summed. This quantity called p_J would been large for a track within a jet and nearly zero for isolated electron tracks. Since electron tracks were not always isolated and may have been overlapped by a jet, this cut had only a 77% efficiency when p_J cut was greater than 1.3 GeV. The distribution of p_J is shown in figure 3.5 before any of the final cuts were made.

Depth Cut

In order to know the energy of a particle it was required to pass through at least 13 radiation lengths of the shower counter. This was only relevant to particles hitting near the edge of the detector.

Cut Efficiencies

An estimate of the efficiency of a cut is found using the equation

$$\hat{\epsilon}_S = \frac{\hat{\mu}_S^A}{\hat{\mu}_S^B} = \frac{N_{+-}^A - 2\sqrt{n_{++}^A n_{--}^A}}{N_{+-}^B - 2\sqrt{n_{++}^B n_{--}^B}}$$

where the superscripts [1] determine whether values were to be taken before or after the cut (See figure 3.7a)). Since six values must be measured to obtain ϵ_S, determining the error in ϵ_S was not a completely trivial task. A Monte Carlo was used to model the fluctuations that could occur in determining $\hat{\epsilon}_S$.

Each pass of the Monte Carlo simulates performing the experiment under the same conditions of the real experiment (see figure 3.7c)). In each pass the number

[1] Superscripts are either A for after the cut or B for before the cut. Subscripts are either S for the true electron pair signal or B for background events. Little n's are used only for background events.

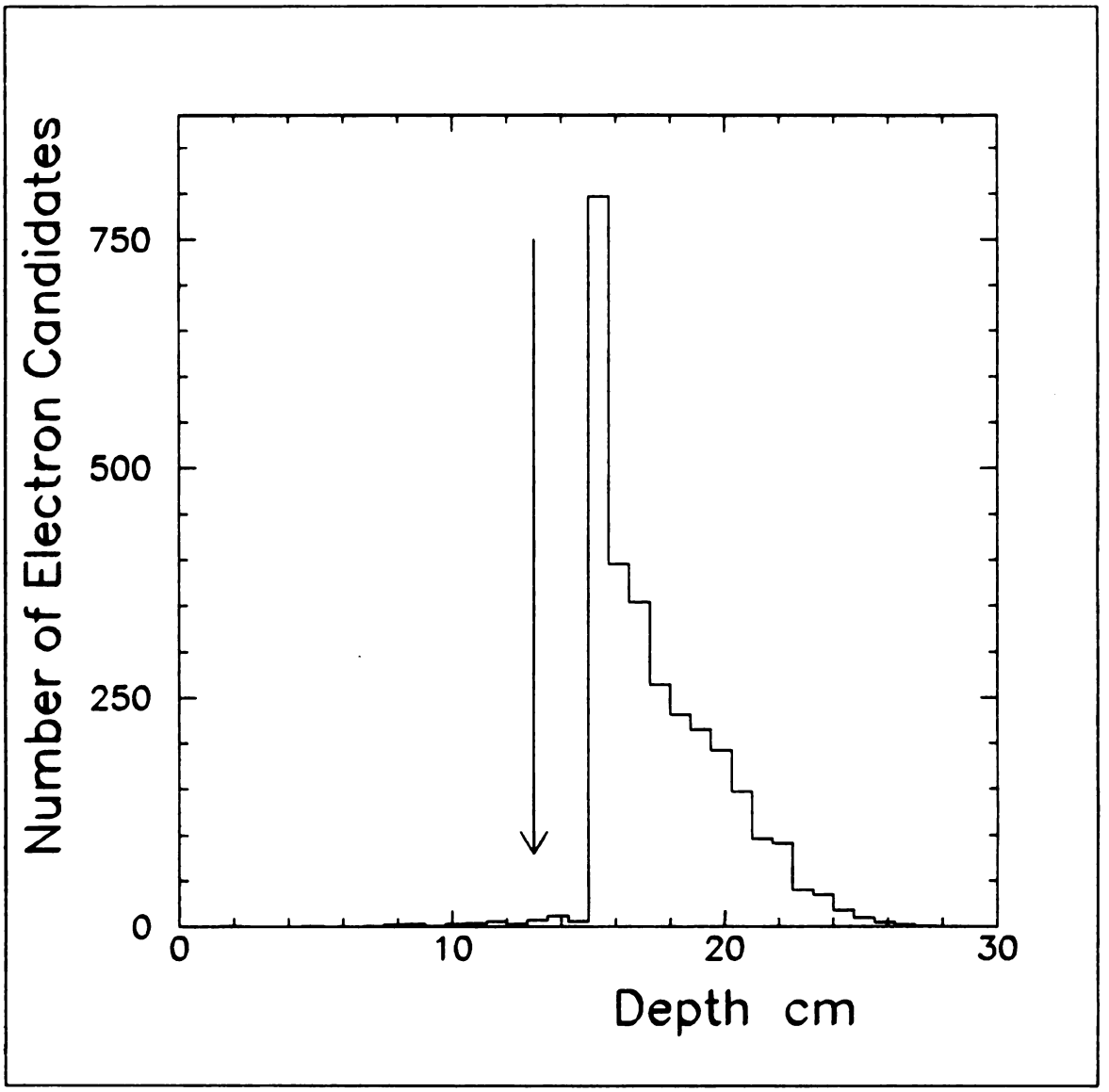

Figure 3.6: The depth distribution

The distribution was from events with two good clusters and matching tracks. Events with tracks passing through less than 13 cm of shower counters were rejected.

of true electron pairs, S^B, and background events, B^B, are generated from Poisson distributions $P(S^B|\hat{\mu}_S)$ and $P(B^B|\hat{\mu}_B)$.

The means of the two distributions $\hat{\mu}_S$ and $\hat{\mu}_B$ were determined from the data (see figure 3.7b)). Background events were then split up according to charge by the multinomial distribution

$$M(n^B_{+-}, n^B_{++}, n^B_{--}|B^B, \hat{p}(1-\hat{p}), \hat{p}^2, (1-\hat{p})^2)$$

in agreement with section 3.2.7. The selected number of events passing was chosen from binomial distributions with efficiencies $\hat{\epsilon}_S$ for the Drell-Yan signal and $\hat{\epsilon}_B$ for the background determined from the data. The same formula used to estimate the Drell-Yan signal in the data was applied in our simulation to estimate the signal before and after the cut. An estimate of the efficiency, ϵ_S was found using these values and stored in a histogram. A distribution for ϵ_S was then built up after many iterations. This distribution for the cuts can be seen in figure 3.8. Most of the cuts given in table

Table 3.3: Efficiency of cuts

Cut	Cut Efficiency
Δxy and Δz	> 0.90 with 90% confidence level
m_{eT}	> 0.91 with 90% confidence level
R_e	> 0.87 with 90% confidence level
$C/(C+D)$	> 0.78 with 90% confidence level
Depth	> 0.96 with 90% confidence level
α	0.87 ± 0.06
p_J	0.78 ± 0.08

3.3 are assumed to have perfect efficiency since estimates of their efficiency are equal to 1 within errors. The combined efficiency of the α and the p_J cut is found to be 0.68 ± 0.10. When all cuts are considered one single cut the estimate of the efficiency is 0.67 ± 0.14.

a)

	Number of Opposite sign events	Number of plus-plus events	Number of minus-minus events
Before the Cut	N^B_{+-}	n^B_{++}	n^B_{--}
After the Cut	N^A_{+-}	n^A_{++}	n^A_{--}

b) Input parameters to Monte Carlo

$$\hat{\mu}^B_S = N^B_{+-} - 2\sqrt{n^B_{++}n^B_{--}}$$

$$\hat{\mu}^B_B = n^B_{++} + n^B_{--} + 2\sqrt{n^B_{++}n^B_{--}}$$

$$\hat{p}^B_B = \sqrt{n^B_{++}/\hat{\mu}^B_B}$$

$$\hat{\epsilon}_S = \frac{N^A_{+-} - 2\sqrt{n^A_{++}n^A_{--}}}{N^B_{+-} - 2\sqrt{n^B_{++}n^B_{--}}}$$

$$\hat{\epsilon}_B = \frac{n^A_{++} + n^A_{--} + 2\sqrt{n^A_{++}n^A_{--}}}{n^B_{+-} + n^B_{--} + 2\sqrt{n^B_{++}n^B_{--}}}$$

c) Monte Carlo Scheme

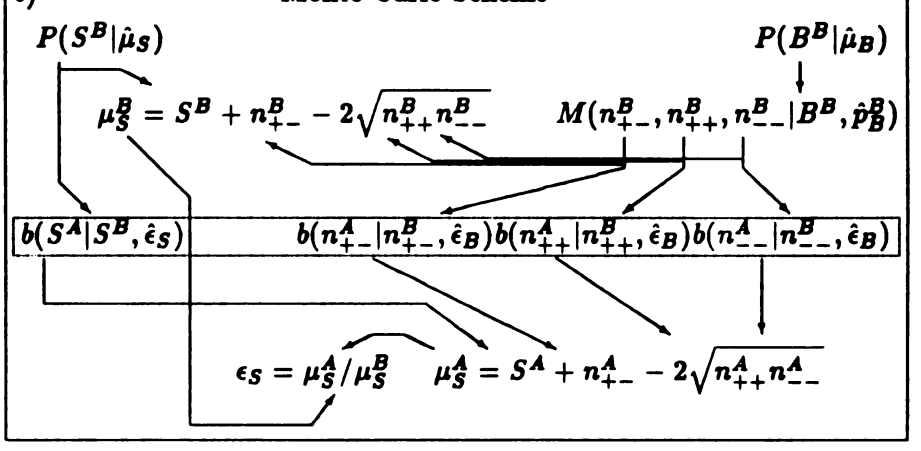

Figure 3.7: Error in efficiency of cuts

a)An estimate of error in the efficiency of a cut was made based on the number of opposite sign, N_{+-}, plus-plus, N_{++}, and minus-minus, N_{--}, events before and after the cut. b)From these numbers an estimate of the true electron pairs, $\hat{\mu}_S$, the total background, $\hat{\mu}_B$, the fraction of positive charged tracks in the background, $\hat{p}_B$, and the efficiency of the cut for both the signal, $\hat{\epsilon}_S$, and background, $\hat{\epsilon}_B$, were made. A Monte Carlo then modeled fluctuation as if the experiment had been performed repeatedly. In c) the scheme for a single pass is shown. The signal, S^B, and the background, B^B, before the cut were generated from Poisson distributions. The background was then split according to a multinomial distribution for the differing charged track combinations. Binomial distributions in the dashed box generated the number of events passing the cut. Finally an estimate of the true electron pair before, μ^B_S, and after, μ^A_S, the cut was used to estimate the efficiency of the cut ϵ_S. The estimated error in the efficiency of the cut was base the distribution of ϵ_S.

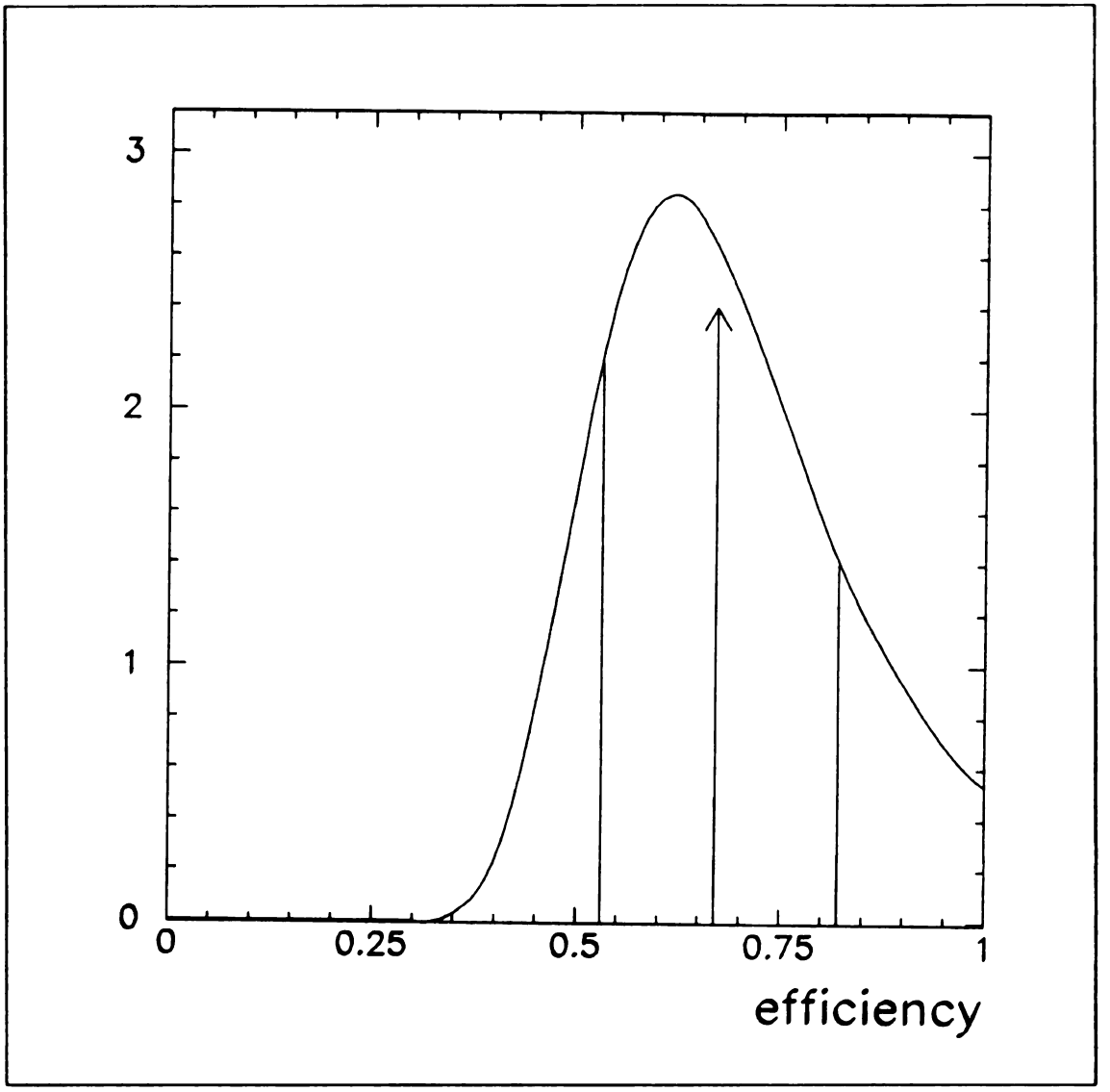

Figure 3.8: Efficiency error

All the final cuts are combined and considered as a single cut. The probability density distribution for efficiency of the signal is found using the Monte Carlo described in this section. The mean is given by the arrow with the two vertical lines one sigma away.

Chapter 4

Cross Section Extraction

4.1 The Monte Carlo Simulation

A Monte Carlo simulation was written to evaluate the efficiencies and acceptance of the R110 detector for measuring electron pairs. This Monte Carlo modeled the geometry and energy resolution of the detector. In it two types of events, Drell-Yan and Upsilon, were generated.

The Drell-Yan type event was picked and weighted according to an appropriate distribution. If the virtual photon of an event had a mass above 11 GeV and a rapidity (rapidity is defined as $y = tanh^{-1}(E/p)$) between -1.2 and +1.2, the "Monte Carlo In" histogram were filled with the event's weight. The 4-momenta of the pair of electrons were then found, and the part of the detector struck, if any, determined. If the shower counters were struck by both electrons, their observed energy was selected using the known resolution of the counters, and their observed momentum rescaled to match this energy. The positions of an electron's track and its cluster were also required to match. Differences between the two resulted when an associated particle overlapped the electron cluster, causing it to have a bad position in z. If the electrons passed the geometric requirements and had good track to cluster matching, cuts were made on their observed energy and the mass of the reconstructed virtual photon. Events passing all these cuts were used to fill the "Monte Carlo Out" histograms.

An Upsilon event went through the same set of steps as the Drell-Yan event, but was considered to be background and thus excluded from the "Monte Carlo In" histograms. It was generated by an experimentally determined distribution [12][13][14] appropriate to the upsilon family of resonances.

4.1.1 Distribution Thrown

Generating either a Drell-Yan or Upsilon event requires choosing 5 independent variables, the 4-momentum of the virtual particle plus the decay angle.

Drell-Yan Distribution

In generating the Drell-Yan event, 3 different reference frames were used. The first was the center-of-mass frame of the two initial protons. This will sometimes be referred to as the ISR reference frame. The second frame was the center of mass frame of the virtual photon. The third frame was the lab frame of the detector.

The first step in generating the Drell-Yan event was choosing the 4-momentum of the virtual photon. This was done by writing the general expression as a product of 2 simpler factors.

$$\frac{d^4\sigma}{dx_1 dx_2 dp_T d\phi} = \frac{1}{2\pi}\frac{d^2\sigma}{dx_1 dx_2}F(p_T) \tag{4.1}$$

Since there was no dependence in ϕ, only the x_1, x_2 and p_T dependence remains.

The cross-section in x_1, x_2 can be written as

$$\frac{d^2\sigma}{dx_1 dx_2} = \frac{4\pi\alpha^2}{9x_1x_2s}\sum_{i=1}^{n} e_i^2\{f_{q_i}(Q^2,x_1)f_{\bar{q}_i}(Q^2,x_2) + f_{q_i}(Q^2,x_2)f_{\bar{q}_i}(Q^2,x_1)\} \tag{4.2}$$

where f_{q_i} and $f_{\bar{q}_i}$ are the parton distributions for the initial hadrons, Q was the momentum transfer and the summation is over the quark flavors. The structure functions used here were Duke and Owens [15] set 1.

For the p_T distribution use was made of the empirical form [16]

$$F(p_T) = \frac{10^{\frac{p_T}{p_0}}}{(1+(\frac{p_T}{p_0})^2)^6}. \tag{4.3}$$

From

$$\langle p_T \rangle = \int_0^\infty dp_T p_T F(p_T) \tag{4.4}$$

it can be shown that

$$p_0 = \frac{256}{35\pi}\langle p_T \rangle. \tag{4.5}$$

The value of p_0 was obtained after an iterative procedure comparing MC_{out} with the data. The values for $\langle p_T \rangle$ have been found many times in this experiment in its various incarnations. In earlier data sets, values for $\langle p_T \rangle$ ranged from a fit value to acceptance corrected data of 1.9 GeV/c to an average value of the raw data of 2.7 GeV/c. Since then the size of the data set has increased, the Monte Carlo has been improved and the method of fitting has improved. Currently the value for the raw data is 2.0 GeV/c while the average of the acceptance corrected value is 2.2 GeV/c. Values from maximum likelihood fits of the empirical form (4.3) to the current data set after acceptance correction were made have been within the range of 2.10 to 2.45 GeV/c. Fitting was done using the maximum likelihood method. The "standard" Monte Carlo for this experiment ran using $\langle p_T \rangle = 2.3$ GeV/c for the input distribution. From the final version of the Monte Carlo the likelihood curve in figure 4.1 was generated. The best fit occurs with a Monte Carlo value for $\langle p_T \rangle = 2.2\ ^{+0.15}_{-0.2}$ GeV/c .

The next step was the decay of the virtual photon into the lepton pair. In the Drell-Yan model with quarks moving parallel to the incident hadrons the angular distribution of the lepton pair is $1 + \cos^2\theta$, where θ is the angle between the lepton momentum and the beam axis in the dilepton's center-of-mass frame. Because of large $\vec{Q_T}$, however, the incident hadrons are no longer collinear in the dilepton's center-of-mass system. This forces one to define a new z axis for this system. The usual choice is the Collins-Soper frame [17] where the z axis is chosen halfway between the two incident hadrons. The azimuth is measured from the plane formed by the intersection of the two incident hadrons. In the Monte Carlo, the generated photon's momentum

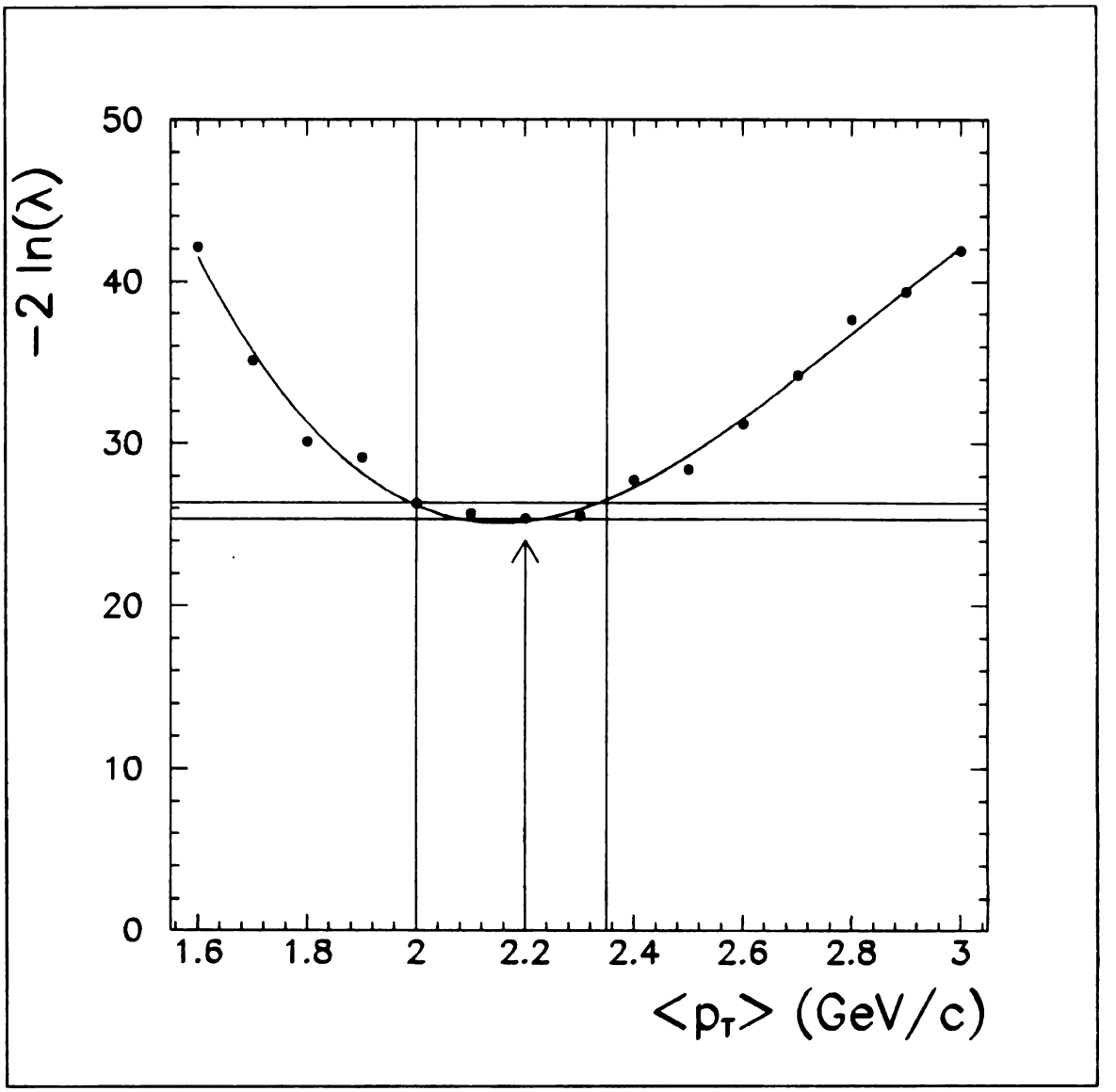

Figure 4.1: Likelihood curve for $\langle p_T \rangle$

The likelihood curve is found by running the Monte Carlo with different values of $\langle p_T \rangle$ for the input distribution. Using the normalized distribution of p_T out as the probability density function the likelihood, L. is found for each value of $\langle p_T \rangle$.

was t

distri

ϒ Di

The c

$\cos\theta$

ϒ′ ar

4.1.

The

in th

trac

13.0

Dri

Beca

the

cou

that

plan

was transformed to the Collins-Soper frame, where the photon decayed. The angular distribution had the form $1 + \alpha \cos^2\theta$ where α was normally set equal to 1.

Υ Distribution

The distributions of the upsilon resonances in mass [12], Feynman x [13], p_T^2 [13], and $\cos\theta$ [14] were empirical forms taken from several experiments. The resonances Υ , Υ' and Υ'' were included.

$$\sigma_\Upsilon + \sigma_{\Upsilon'} + \sigma_{\Upsilon''} = 14.5pb \tag{4.6}$$

$$\frac{d\sigma}{dm} \propto e^{-\frac{1}{2}(\frac{m-m_\Upsilon}{\Delta m_\Upsilon})^2} + 0.30e^{-\frac{1}{2}(\frac{m-m_{\Upsilon'}}{\Delta m_{\Upsilon'}})^2} + 0.15e^{-\frac{1}{2}(\frac{m-m_{\Upsilon''}}{\Delta m_{\Upsilon''}})^2} \tag{4.7}$$

$$\frac{d\sigma}{dx_F} \propto (1.0 - |x_F|)^{3.3} \tag{4.8}$$

$$\frac{d\sigma}{dp_T^2} \propto e^{-1.12p_T} \tag{4.9}$$

$$\frac{d\sigma}{d\cos\theta} \propto 1 + 0.31\cos^2\theta \tag{4.10}$$

4.1.2 Geometric Cuts

The two electrons, now given in the center of mass of the initial protons were boosted in the -x direction into the lab frame. Knowing the lab momenta, the electrons' tracks were projected through the magnetic field to see if they go through at least 13.0 radiation lengths of shower counter.

Drift Chambers

Because of the gaps at the top and bottom of the drift chambers (see figure 2.2), the ϕ distribution measured by the detector was dependent not only on the shower counters' positions but also the position of drift chambers. The Monte Carlo assumed that all planes in the drift chambers have an efficiency of 85% and required a least 6 planes to trigger per track.

The probability that a track striking n planes, with an efficiency of p per plane, would trigger i planes was given by the binomial distribution

$$b(i;n,p) = \binom{n}{i} p^i (1-p)^{n-i}$$

The probability that at least m planes were triggered in such a case is

$$B(m;n,p) = \sum_{m=i}^{n} b(i;n,p)$$

The Monte Carlo simply found n, the number of planes the track passed through, and assigned a weight of B(6;n,0.85) for that track. The weight of the event, if it was accepted, was then scaled by the product of the weights for the two electron tracks.

4.1.3 Leakage, Smearing and Energy Cuts

Since the shower counters were not infinitely thick, some of the shower from the electrons would leak out the back of the counters. The energy contained in the counters was therefore less than the initial energy of the electron. The average longitudinal shape of electron and photon shower is [18] [19] given by

$$\frac{dE}{dt} = E_0 \frac{b^{\alpha(E_0)+1}}{\Gamma(\alpha(E_0)+1)} t^{\alpha}(E_0) e^{-bt} \tag{4.11}$$

where t is the depth in the shower counter given radiation lengths, E_0 is the initial energy of the electron, dE the energy deposited in the counters between the depth t and $t+dt$ and Γ the usual gamma function. α is related to the position of the shower maximum and therefore is energy dependent: The dependence of α on the energy in GeV was given by

$$\alpha(E) = bt_{\max} \simeq b(t_{\text{med}} - 1.5) = b[ln(E/\epsilon) + a - 1.5] \tag{4.12}$$

wh

fro

wh

cha

was

wh

len

By
ele
by

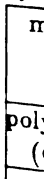

dep

wh

4 G

where $b \simeq 0.5$, $a \simeq 0.4$ for electrons, $\epsilon \simeq \frac{0.55 \text{ GeV}}{Z_{eq}}$ and E is in GeV . Z_{eq} can be found from

$$Z_{eq} = \sum_i f_i Z_i \tag{4.13}$$

where f_i is the fraction of element i by weight and Z_i is its nuclear charge.

The composition of the shower counters is given in table 4.1 with the density, charge of the nucleus and the fraction of the given element. From this table the Z_{eq} was calculated to be 76.8.

The radiation length for a mixture of elements was approximated by

$$\frac{1}{L_R} \simeq \sum_i \frac{t^i}{L_R^i}$$

where t^i is the relative thickness of the element i. Using table 4.1 again, the radiation length for the shower counters is 1.0 cm. To get the total energy deposited up to a

Table 4.1: Composition of shower counters
By knowing the thickness and density of the material, and the molecular weight of the elements, the fraction by weight of each element in the shower counters was found and used to calculate Z_{eq}.

material	thickness (cm)	L_{rad} (cm)	density (g/cm^3)	element	Molecular Weight (g/mole)	total mass (g/cm^2)	Z	fraction by weight
polystyrene $(CH)^2$	0.4	42.4	1.03	H	1.01	0.032	1	0.005
				C	12.01	0.381	6	0.063
lead	0.5	0.561	11.35	Pb	238.03	5.675	82	0.932

depth t, the equation 4.11 is integrated from 0 to t giving

$$E = E_0 \frac{\gamma(\alpha(E_0), t)}{\Gamma(\alpha(E_0))} \tag{4.14}$$

where γ is the incomplete gamma function.

Since the shower counters were calibrated to read 4 GeV for an electron with 4 GeV of energy and a normal angle of incidence, other energies will be read as

$$E = E_0 \frac{\gamma(\alpha(E_0), t)}{\gamma(\alpha(4 \text{ GeV}), t_0)} \frac{\Gamma(\alpha(4 \text{ GeV}))}{\Gamma(\alpha(E_0))} \tag{4.15}$$

Th
das
and
at

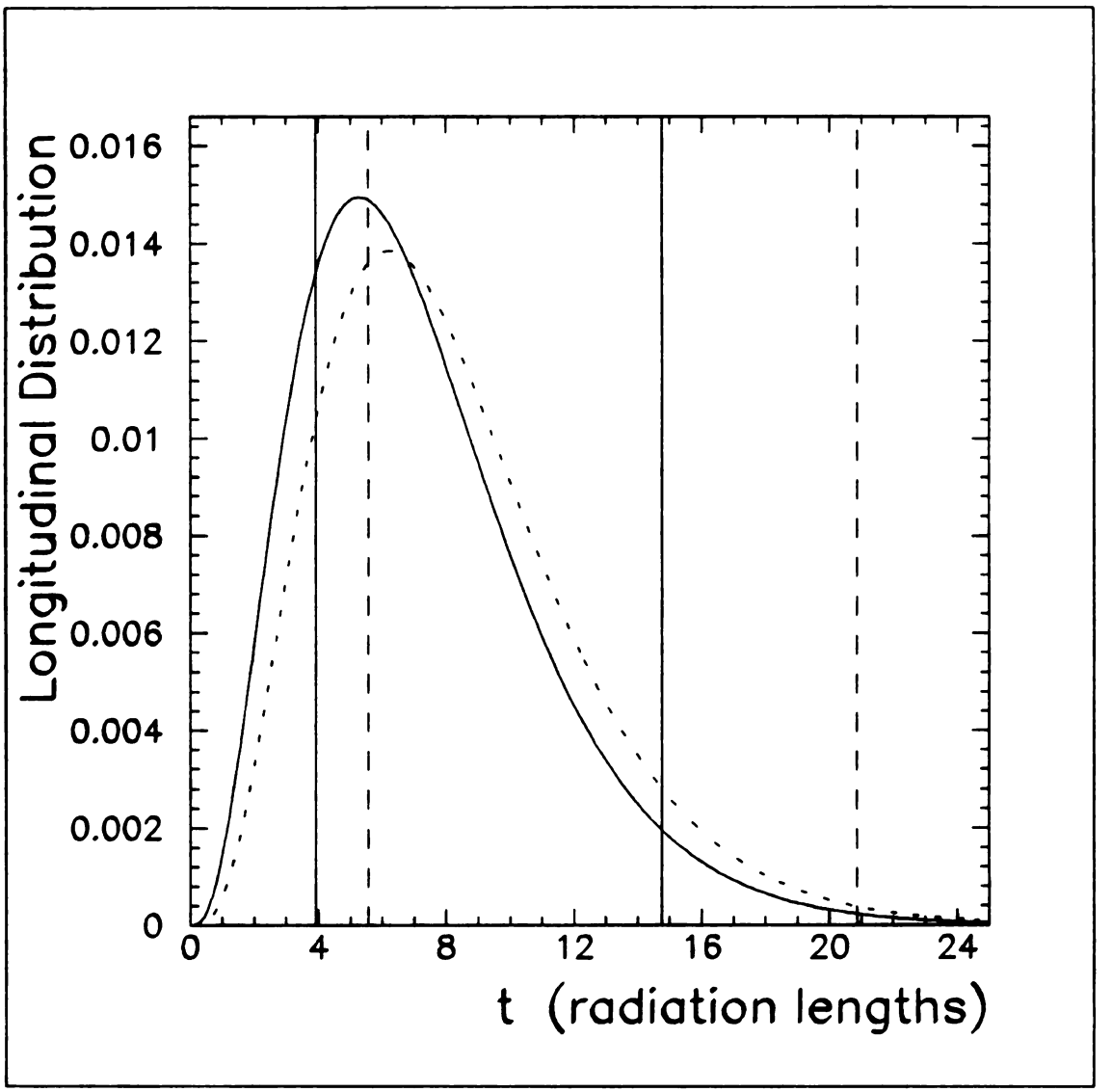

Figure 4.2: The longitudinal shower distribution

The longitudinal energy deposition for a 4 GeV electron is shown as a solid curve. The dashed curve corresponds to a 10 GeV electron. The solid vertical lines mark the back of C and D counters for a normally incident electron, and dashed lines for an electron entering at 45°.

Aft
sm

Usi
mo
the
Dre

4.1

The
the
in t
of t

ters
in t
dep
min
app
one
|y|
in t
of t
mu
all
in t

After the amount of energy deposited in the shower was determined, the energy was smeared according to a Gaussian distribution to reflect the shower counter resolution

$$\frac{\Delta E}{E} = 0.004 + \frac{0.15}{\sqrt{E}} \qquad (E \text{ in GeV}) \tag{4.16}$$

Using the smeared energy, the momentum of the electron was rescaled and the 4-momentum of the photon reconstructed. Energy and mass cuts equivalent to those in the analysis, and a cut on the absolute value of rapidity less than 1.2, were applied. Drell-Yan events passing this cut were added to the "Monte Carlo Out" histograms.

4.1.4 Cluster Formation

The Monte Carlo was used to check the track to cluster matching efficiencies from the data. In track to cluster matching, events were lost mostly due to bad z positions in the cluster. This usually resulted from an associated particle overlapping with one of the electrons, and therefore giving a bad time in the D counters.

Clustering was done for each electron. The counter struck and the adjacent counters were filled using an energy sharing curve that was measured for 4 GeV electrons in the shower counters at the PS (see figure 2.9). Each counter accumulated energy deposited in it and recorded a z position for each end. The z position was determined by the earliest pulse detected at that end of the counter passing a threshold of approximately 0.6 GeV (see figure 4.3). It was possible for the recoil jet to overlap one of the electrons. A jet distribution with $p_{T_J} = -p_{T\gamma}$ and flat in y in the region $|y| < 2.0$ was used. Only the neutral particles in the jet deposited enough energy in the shower counters to have any effect. The measured multiplicity distribution of the neutrals with enough energy to affect the z position was used for the neutral multiplicity of the jet. To measure this distribution, the electron pair data set with all cuts but the p_J cut was used. In each event, the energy a neutral would deposit in the D counters was found using the longitudinal shower distribution. Knowing the

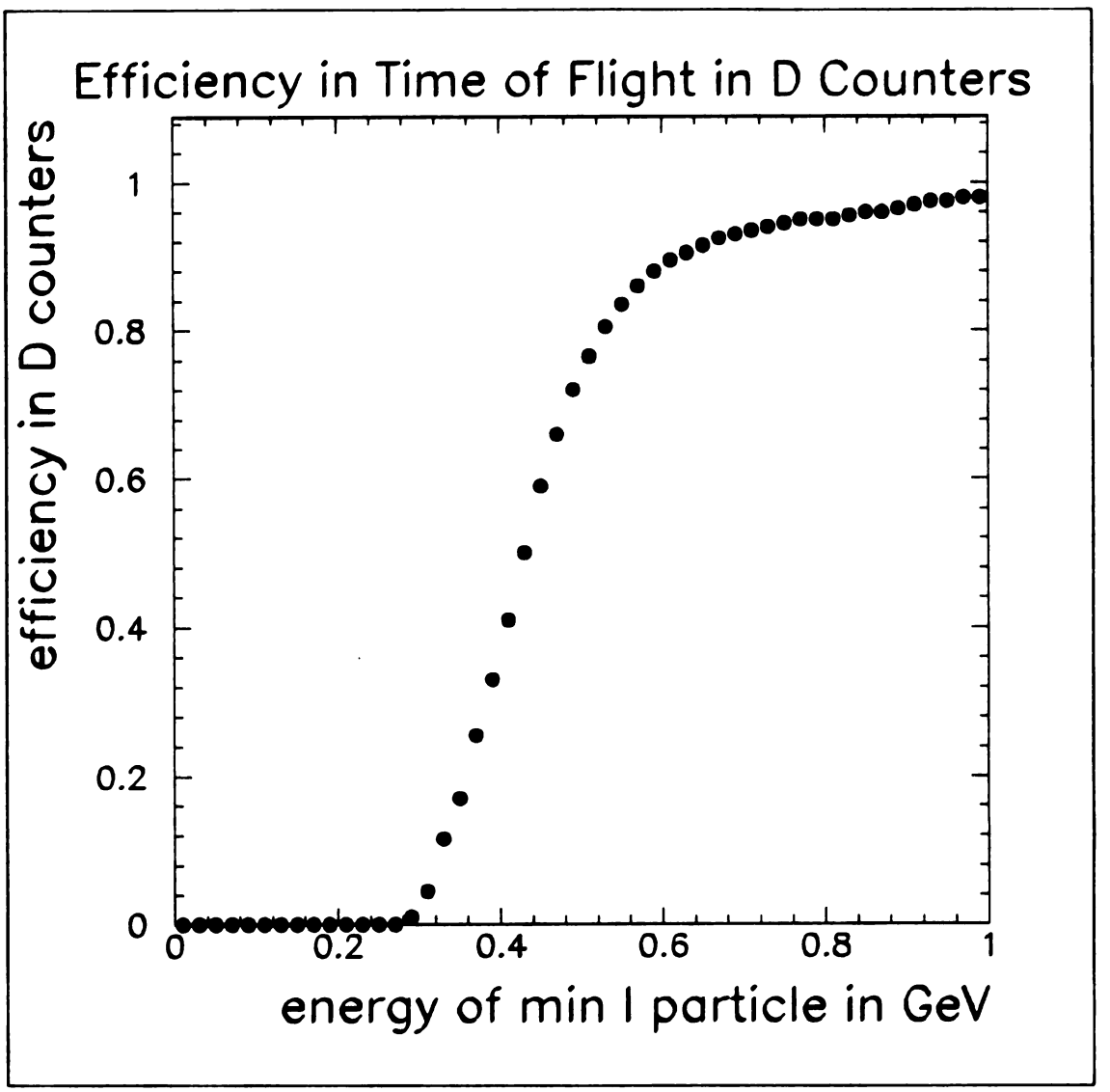

Figure 4.3: Triggering efficiency of TOF in D counters
The probability of a particle triggering the TOF in the D counters as a function of energy[10].

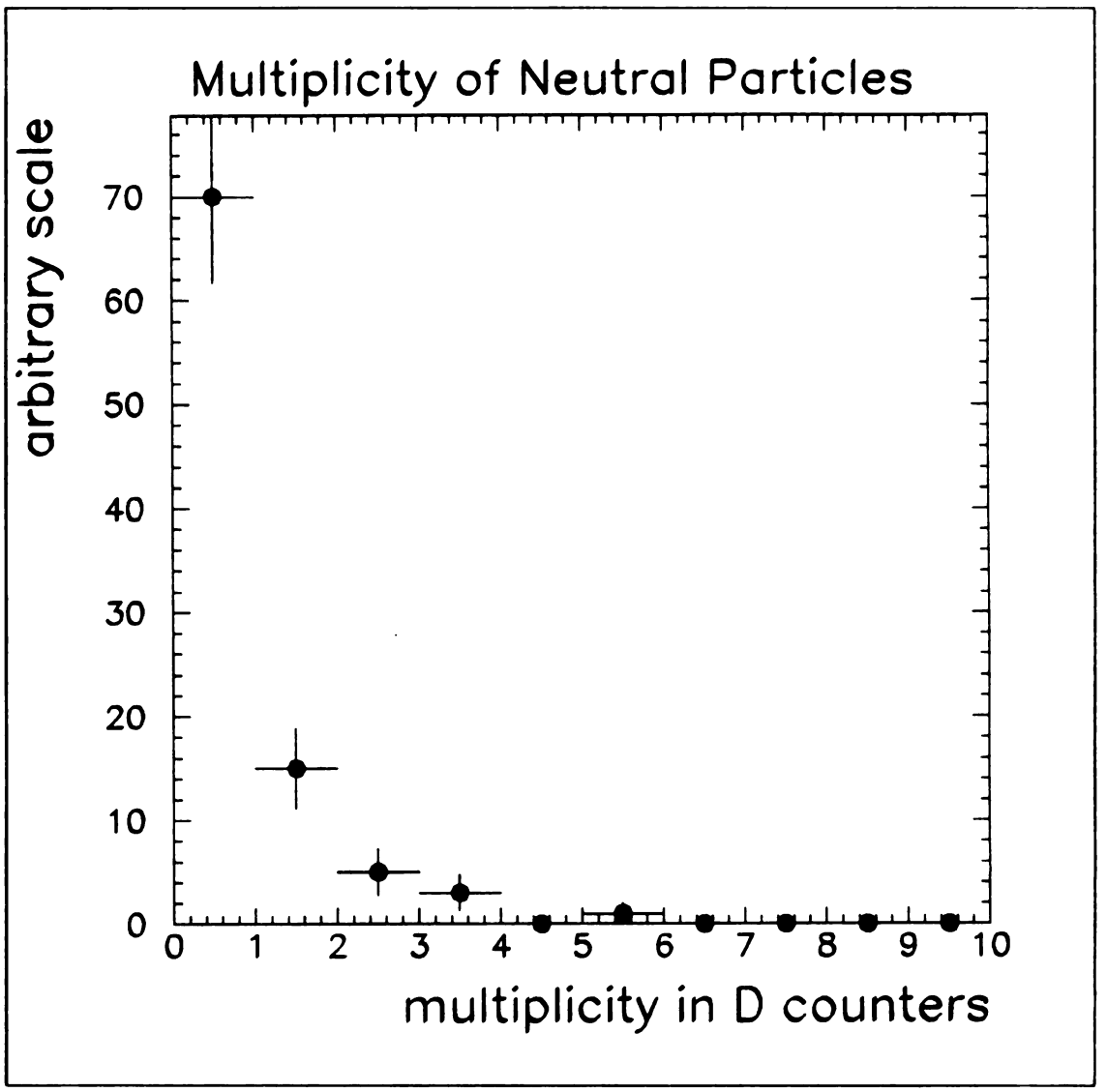

Figure 4.4: Multiplicity distribution in D counters

Multiplicity distribution of neutrals with enough energy to trigger the D time of flight counters.

energy deposited in the D counters, the probability that the particle triggered the time of flight was found from the DTOF efficiency curve (see figure 4.3). Summing the efficiencies for each neutral particle gave the expected number of neutral particles capable of triggering the time of flight in the event (see figure 4.4). The direction of the neutral particles was picked flat in ϕ_n about the jet axis. The variable θ_n, the angle between the jet axis and the neutral particle, was selected from a distribution of θ_n based on a jet analysis [20] by this experiment.

Two cuts made during the formation of the cluster were the ϕ and z matching of the cluster and track. The ϕ of the cluster was calculated as the energy weighted average, as in the analysis program. The z of the cluster was the energy weighted average from counters with more than 1 GeV. The ϕ and z for the track were taken at its intercept with a cylinder of radius 60 cm . While the estimated efficiency of the ϕ cut from the Monte Carlo was over 99%, the z cut was significantly less. The z cut efficiencies are given in table 4.2.

Table 4.2: Efficiencies for z track to cluster matching cuts

Cuts	Efficiency of electrons from Monte Carlo
$\lvert z_{\text{track}} - z_{\text{seed}} \rvert < 20.0$ cm	0.980
$\lvert z_{\text{track}} - z_{\text{cluster}} \rvert < 15.0$ cm	0.924

4.2 Acceptance Correction to the Data

Acceptance corrected cross sections were found using the equation

$$\frac{d\sigma(x)}{dx} = \frac{Data(x) - Back(x)}{\mathcal{L}\epsilon_{p_J}\epsilon_{\alpha}\epsilon(x)}$$

where x might be the p_T, m, p_L, etc. of the virtual photon or the electrons. The $Data(x)$ were the number of opposite sign events and $Back(x)$ the estimated background in the opposite sign events. The distribution of the background because of

low statistics was taken from the same sign events with two good tracks and matching clusters. The normalization for the background was found from the number of positive same sign events, n_{++}, and negative same sign events, n_{--}, passing all cuts, and using equation 3.5. $\mathcal{L}$ was the luminosity as discussed in section 2.1.1. In the Monte Carlo, two sets of histograms $MC_{in}(x)$ and $MC_{out}(x)$ were filled. $MC_{in}(x)$ accepted all of the generated Drell-Yan events with mass greater than $11GeV$ and an absolute value of rapidity less than 1.2. The efficiency $\epsilon(x)$ was

$$\epsilon(x) = \frac{MC_{out}(x)}{MC_{in}(x)}.$$

ϵ_α and ϵ_{p_J} were the estimated efficiencies for the α and p_J cuts respectively (see section 3.2.8). These efficiencies were found from the ratio of the signal in the data with the cut applied divided by the signal without the cut (see table 4.3). All other cuts were left in.

Table 4.3: α and p_J efficiencies
The efficiencies ϵ_α and ϵ_{p_J} are found from the data by taking the ratio of the signal when the cut was applied to the signal without the cut. All other were applied for both cases.

Cuts	(+−)	(++)	(−−)	Signal	Efficiency
all cuts	105	9	1	99±13	
no α cut	131	23	3	114±16	0.87±0.06
no p_J cut	189	63	15	127±24	0.78±0.08

4.3 Cross Sections

The cross section $d^2\sigma/dmdy|_{y=0}$ for $m > 11$ GeV is shown in figure 4.5 and table 4.4. The data are in good agreement with other $pp \rightarrow e^+e^-$ results [21] [22] obtained at the ISR. Results for the R209 experiment are based on their $d\sigma/dm$ cross section [12] and converted by multiplying by the ratio

$$\left.\frac{d^2\sigma}{dmdy}\right|_{y=0} \Big/ \frac{d\sigma}{dm}$$

found from the Monte Carlo input distributions (see section 4.1.1). At Fermilab the CFS Collaboration [16] obtained the values of $d^2\sigma/dmdy|_{y=0}$ for a $\sqrt{s}$ = 27 GeV. The cross section of the Fermilab experiment at the lower $\sqrt{s}$ is lower than the data presented here by about a factor of 20 at m = 12 GeV/c and a factor of 1000 at m = 20 GeV/c. It is of interest to note that while the collider experiments at the ISR enjoy a higher cross section, the fixed target Fermilab experiment is compensated by higher interactions rates, so that both run out of events around 20 GeV.

Table 4.4: Cross section $d^2\sigma/dmdy|_{y=0}$

m in GeV/c^2	Cross Section pb c^2/GeV
11.5	1.82 ± 0.28
13.0	0.56 ± 0.11
15.0	0.33 ± 0.08
17.0	0.13 ± 0.05
19.5	0.13 ± 0.05

Figure 4.6 compares the data of this experiment with the theoretical predictions of reference [8]. These predictions were obtained by calculating in QCD all terms up to and including order $\alpha_s(Q^2)$ that give rise to the so-called K factor. Comparing the total cross section above 11 GeV/c^2 with the lowest order predictions, a K factor of 1.75 ± 0.60 is found. The K factor as a function of mass is shown in figure 4.7 together with a line representing the integral K factor. The quantity $sd^2\sigma/d\sqrt{\tau}dy|_{y=0}$ in the simple Drell-Yan model is a function of $\tau = (m^2/s)$ only rather than a function of m and s separately. The validity of this scaling prediction is demonstrated in figure 4.8, where the scaled cross sections from this experiment and from CFS are seen to agree in spite of the large differences observed in $d^2\sigma/dmdy|_{y=0}$. The values for the points for this experiment are given in table 4.5. The quantities $d\sigma/dy$ in figure 4.9 and $d\sigma/dx_F$ (In center of mass frame $x_F = 2p_z/\sqrt{s}$) in figure 4.10 are shown with comparisons between the data and the Monte Carlo input, where the Monte Carlo

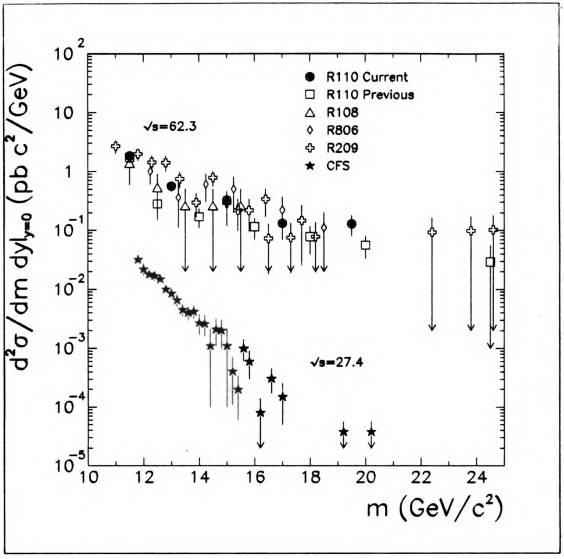

Figure 4.5: Invariant mass dependence of cross section (comparison with experiments) The cross section $d^2\sigma/dmdy|_{y=0}$ in this experiment and others (R110 Previous [23], R108[22], R806[21], R209[12]) at $\sqrt{s}$ = 62.3 GeV and by CFS [16] at $\sqrt{s}$ = 27.4 GeV. (The data of R209 have converted from their original form of $d\sigma/dm$.)

Table 4.5: The scaling-invariant mass cross section

m in GeV/c²	Cross Section pb GeV²
0.18	479977 ± 67281
0.22	105505 ± 19961
0.26	66581 ± 15719
0.30	22449 ± 9174
0.34	7995 ± 5654

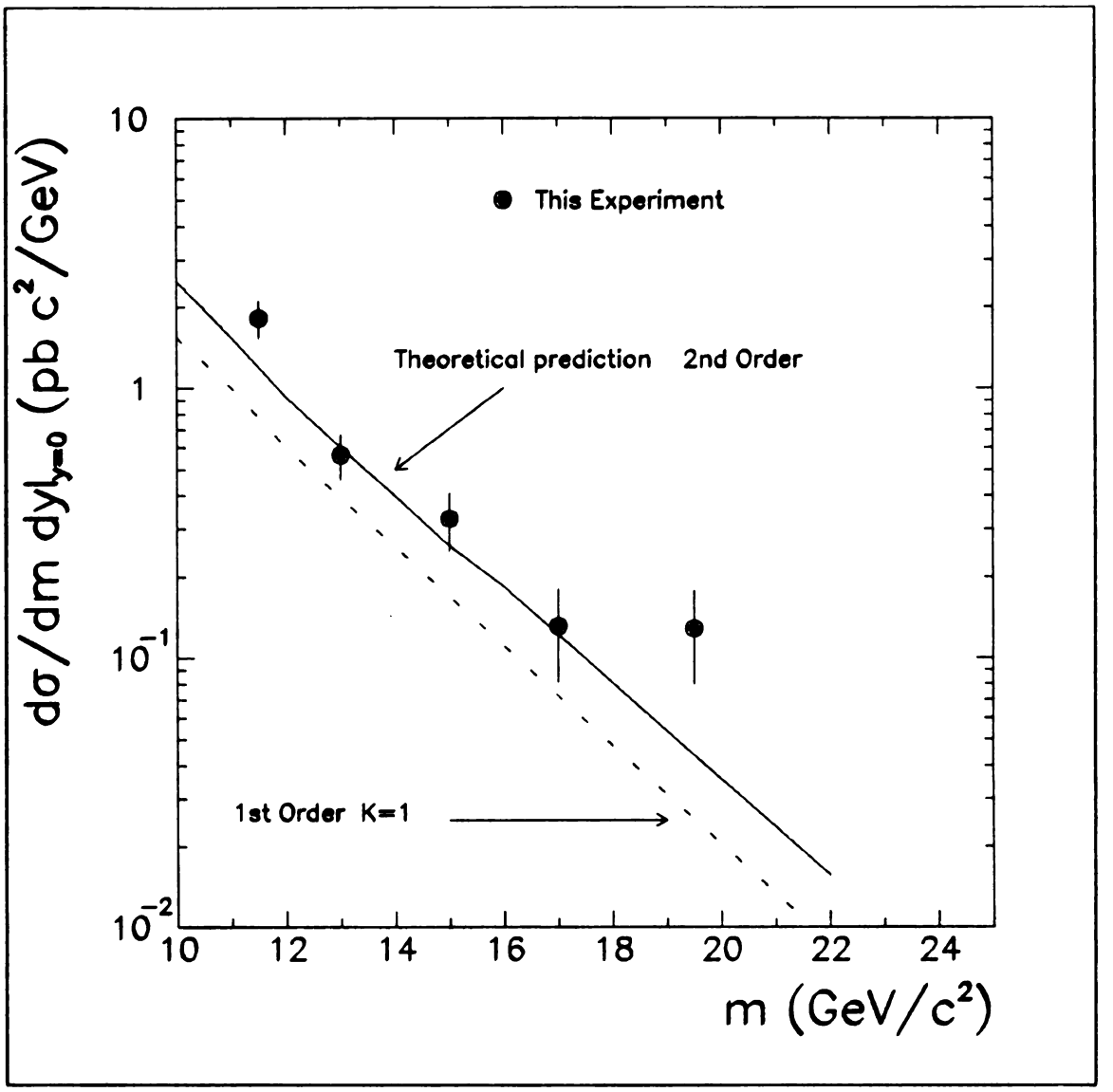

Figure 4.6: Invariant mass dependence of cross section (comparison with theory) The cross section $d^2\sigma/dmdy|_{y=0}$ is shown with the theoretical predictions[8].

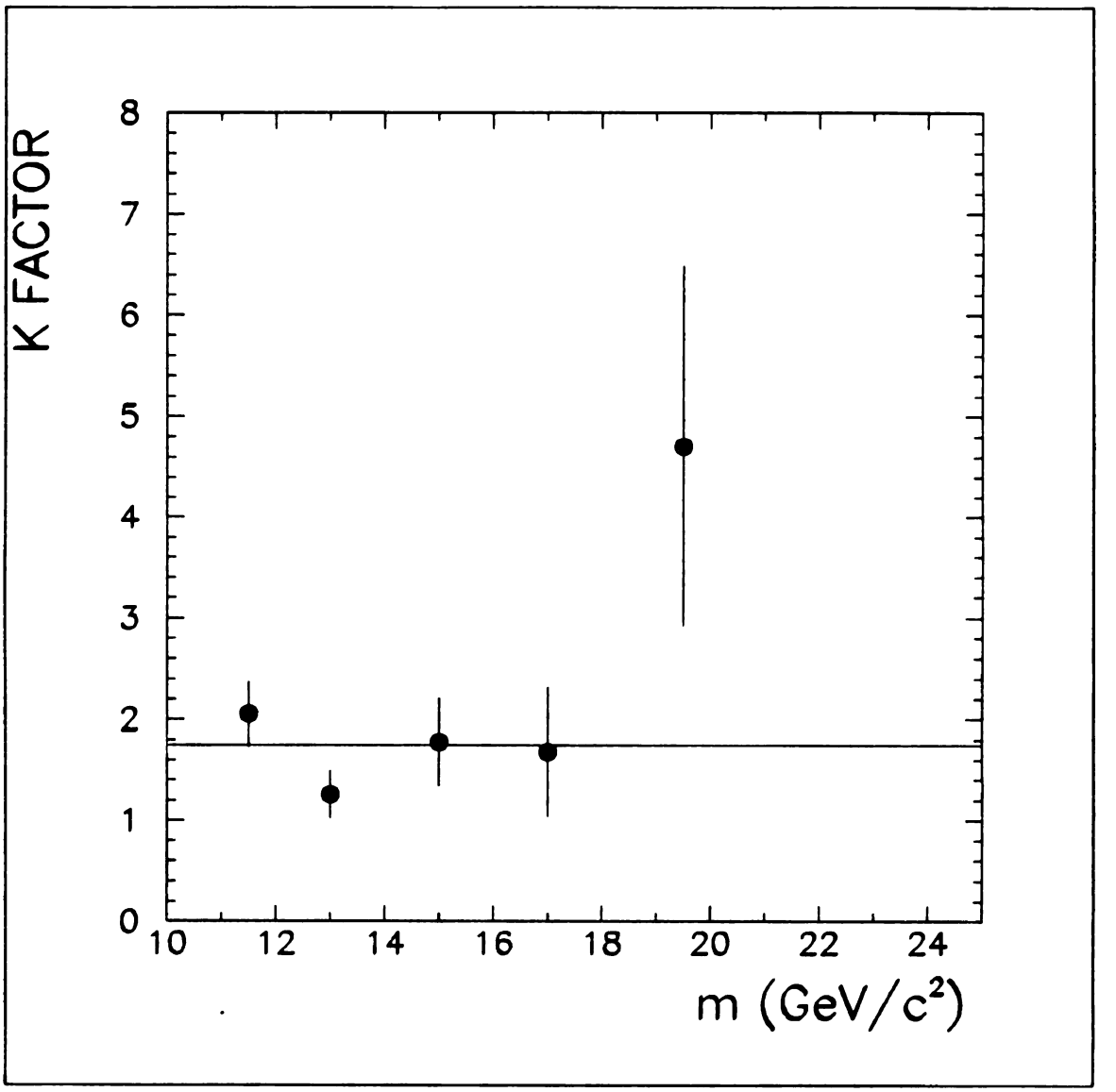

Figure 4.7: The K factor plotted as a function of mass.

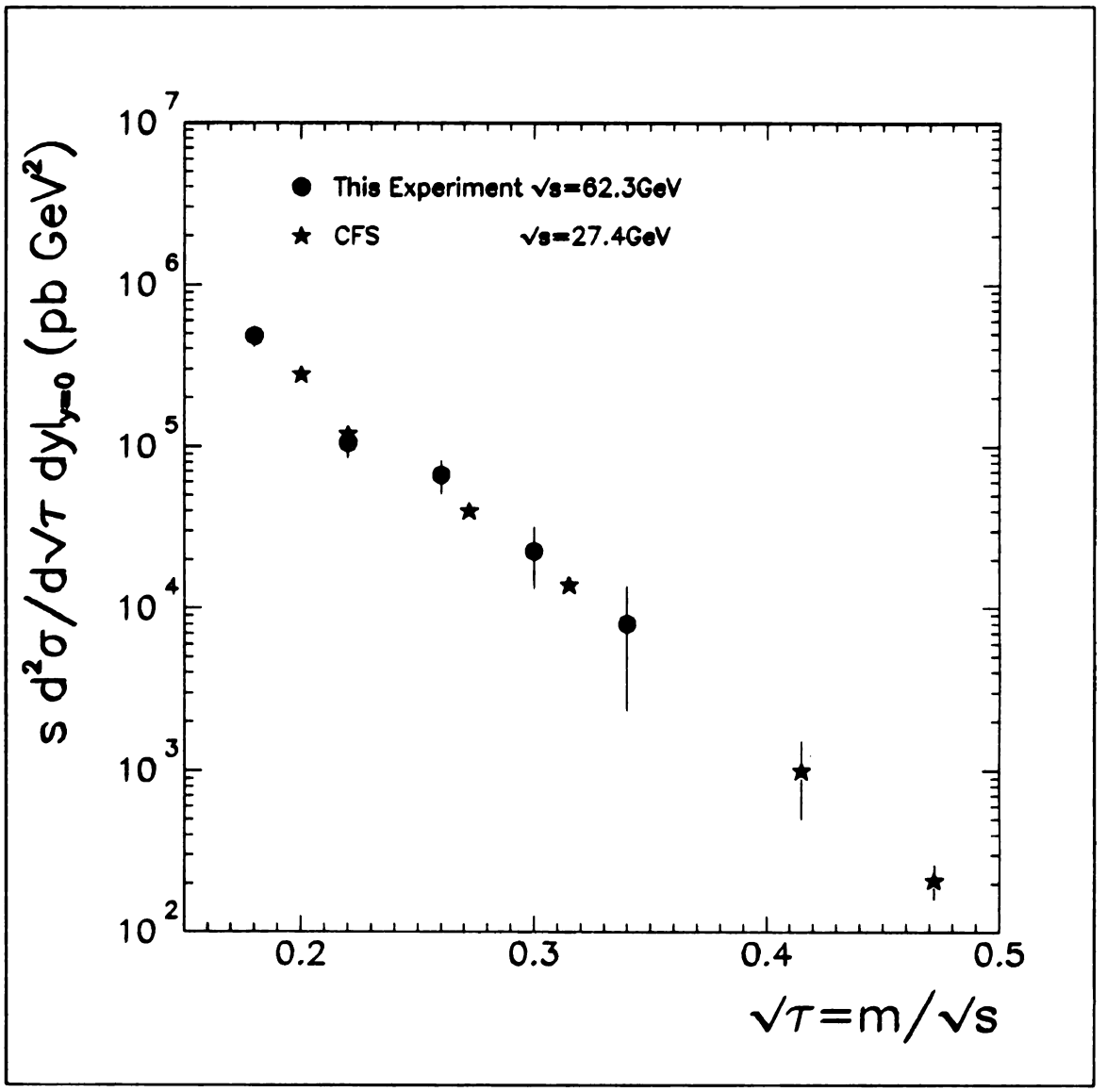

Figure 4.8: The scaling-invariant cross section
The scaling quantity $sd^2\sigma/d\sqrt{\tau}dy|_{y=0}$ obtained in this experiment at $\sqrt{s}$ = 62.3 GeV and at $\sqrt{s}$ = 27.4 GeV by the CFS collaboration[16].

input is defined in section 4.1. The mean transverse momentum of the electron pair, $\langle p_T \rangle$, was found by varying the $\langle p_T \rangle$ parameter in the Monte Carlo until the output distribution best represented the data. In this way $\langle p_T \rangle$ was found to be 2.2 ± 0.2 GeV/c . The transverse momentum distribution, corrected for acceptance, is shown in figure 4.11 along the theoretical curve of reference [8]. The acceptance corrected data is also shown in table 4.6.

Table 4.6: The transverse momentum distribution

p_T GeV/c	Cross Section pb c/GeV
0.5	1.11 ± 0.20
1.5	1.25 ± 0.22
2.5	0.89 ± 0.19
3.5	0.42 ± 0.13
4.5	0.28 ± 0.13
5.5	0.13 ± 0.10
6.5	0.02 ± 0.02
7.5	0.13 ± 0.09

In contrast to the naive parton model, QCD predicts that the mean transverse momentum will increase as a function of $\sqrt{s}$ for fixed values of τ. The value of $\langle p_T \rangle$ obtained in this experiment compared with data obtained at lower $\sqrt{s}$ [16] [12] [24] are shown in figure 4.12. A linear increase with $\sqrt{s}$ is clearly seen. The form of the cross section in a region where second-order effect dominates is expected to be:

$$d^3\sigma/dp_T^2 dy dm^2 = (1/s^2 p_T^2) H(x_T, y, \tau)$$

where m, p_T, and y are, respectively, the mass, transverse momentum, and rapidity of the electron pair, $\tau = m^2/s$ and $x_T = 2p_T/\sqrt{s}$. At a given τ and y the quantity $s^2 p_T^2 (d^3\sigma/dp_T^2 dy dm^2)$ is then expected to be a function of x_T only, irrespective of $\sqrt{s}$. A plot of this quantity is shown in figure 4.13 for the events in the range $11 < m < 15$ GeV/c^2 (mean τ of 0.19). The data of the CFS Collaboration [16] in the mass interval 5 to 6 GeV/c^2 and at $\sqrt{s} = 27.4$ GeV are shown in the figure. Note

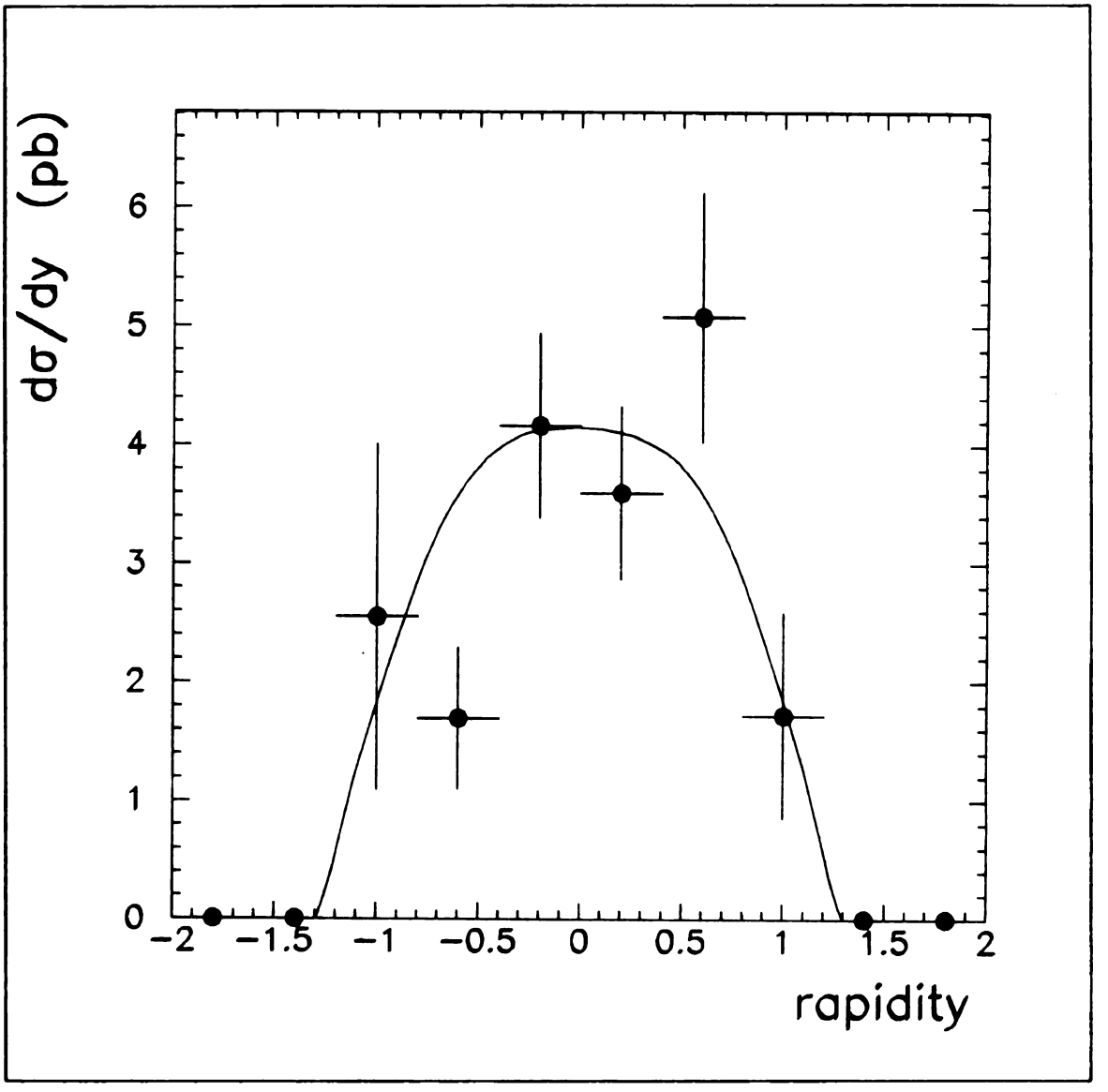

Figure 4.9: The rapidity distribution
The quantity $d\sigma/dy$ from the Monte Carlo is shown as a smooth curve. The data for this experiment is shown with error bars.

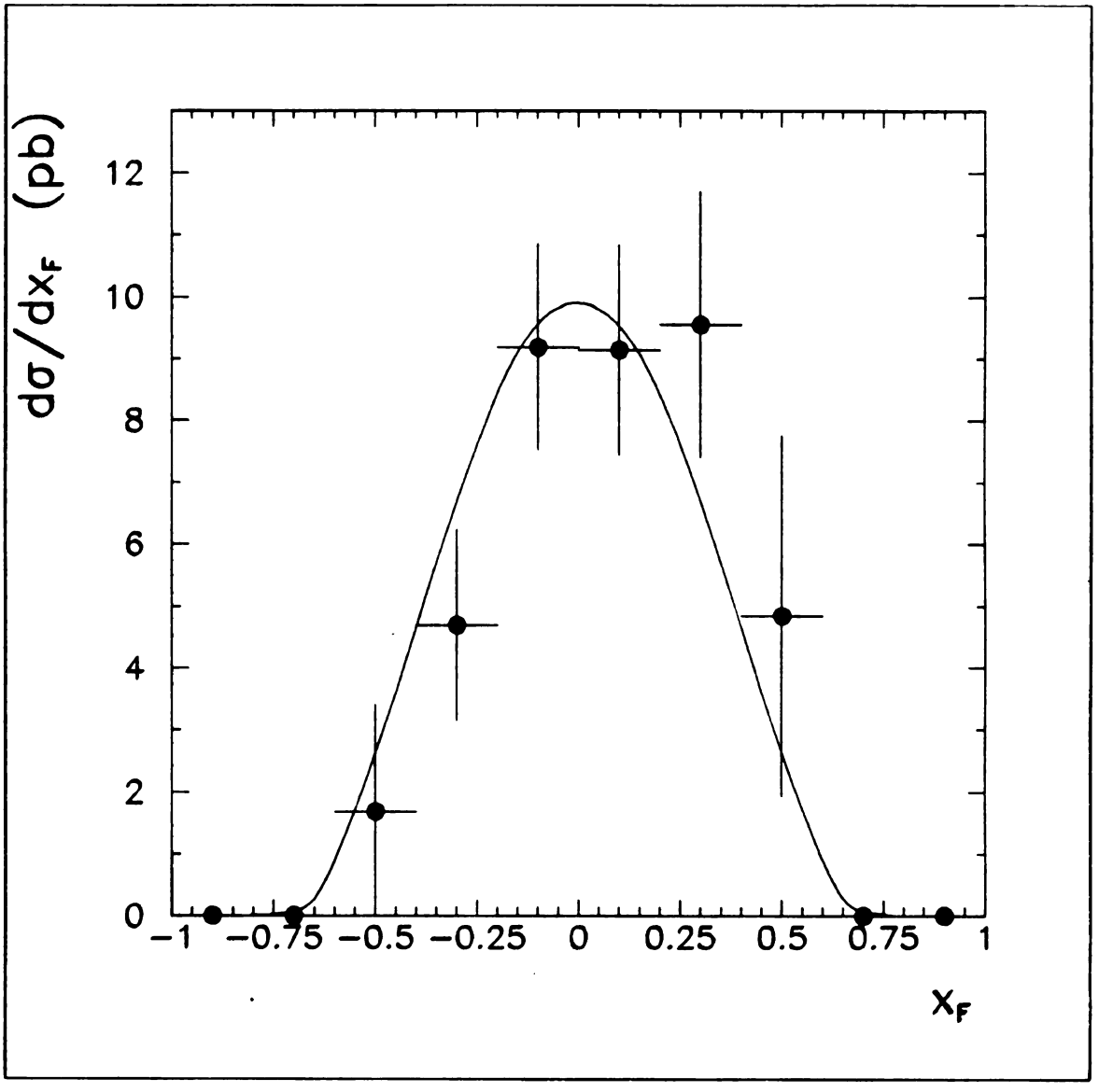

Figure 4.10: The Feynman x Distribution

The quantity $d\sigma/dx_F$ from the Monte Carlo is shown as a smooth curve. The data for this experiment is shown with error bars.

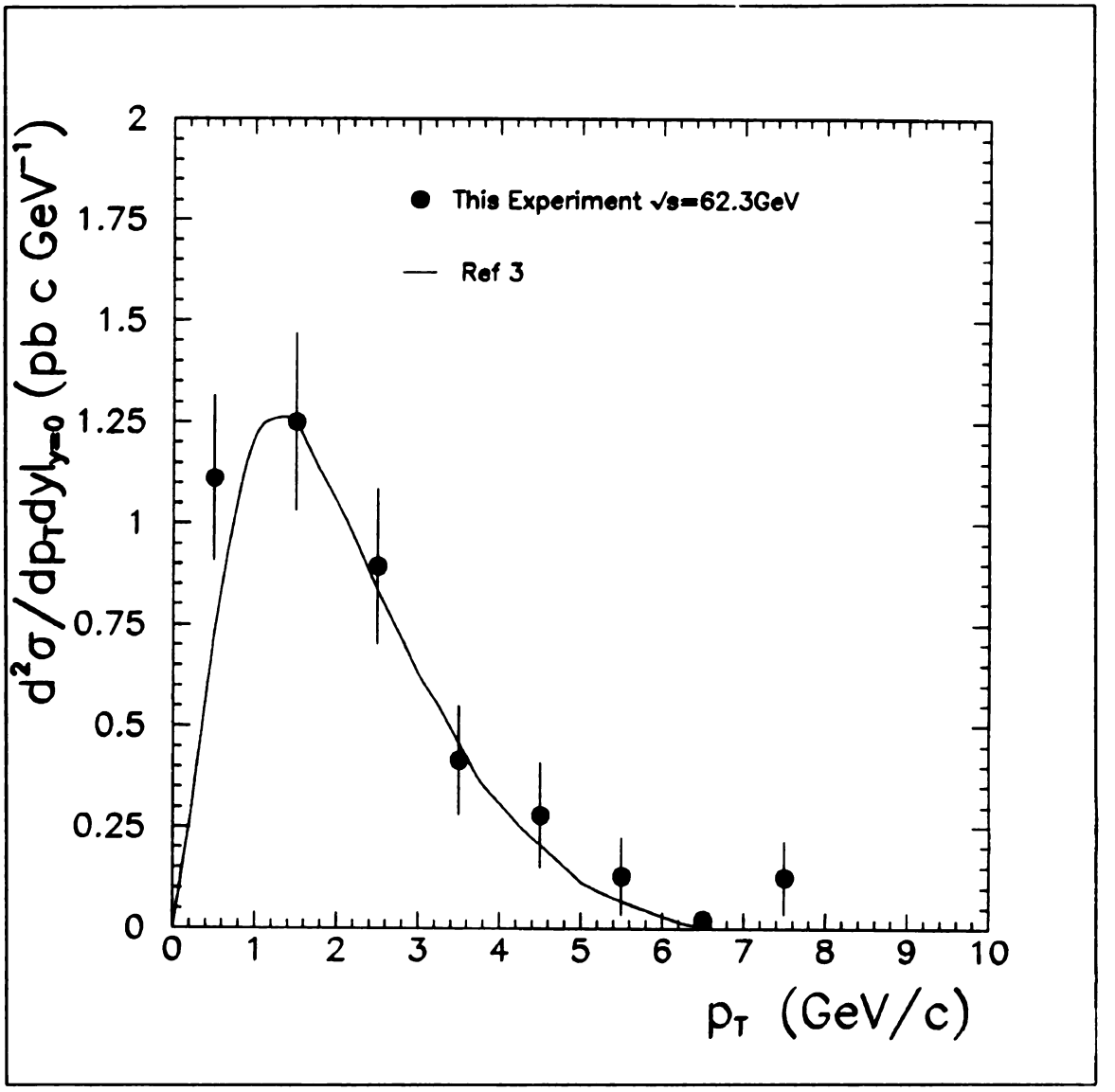

Figure 4.11: The transverse momentum distribution
The cross section $d^2\sigma/dp_T dy|_{y=0}$ is shown with the theoretical predictions[8]

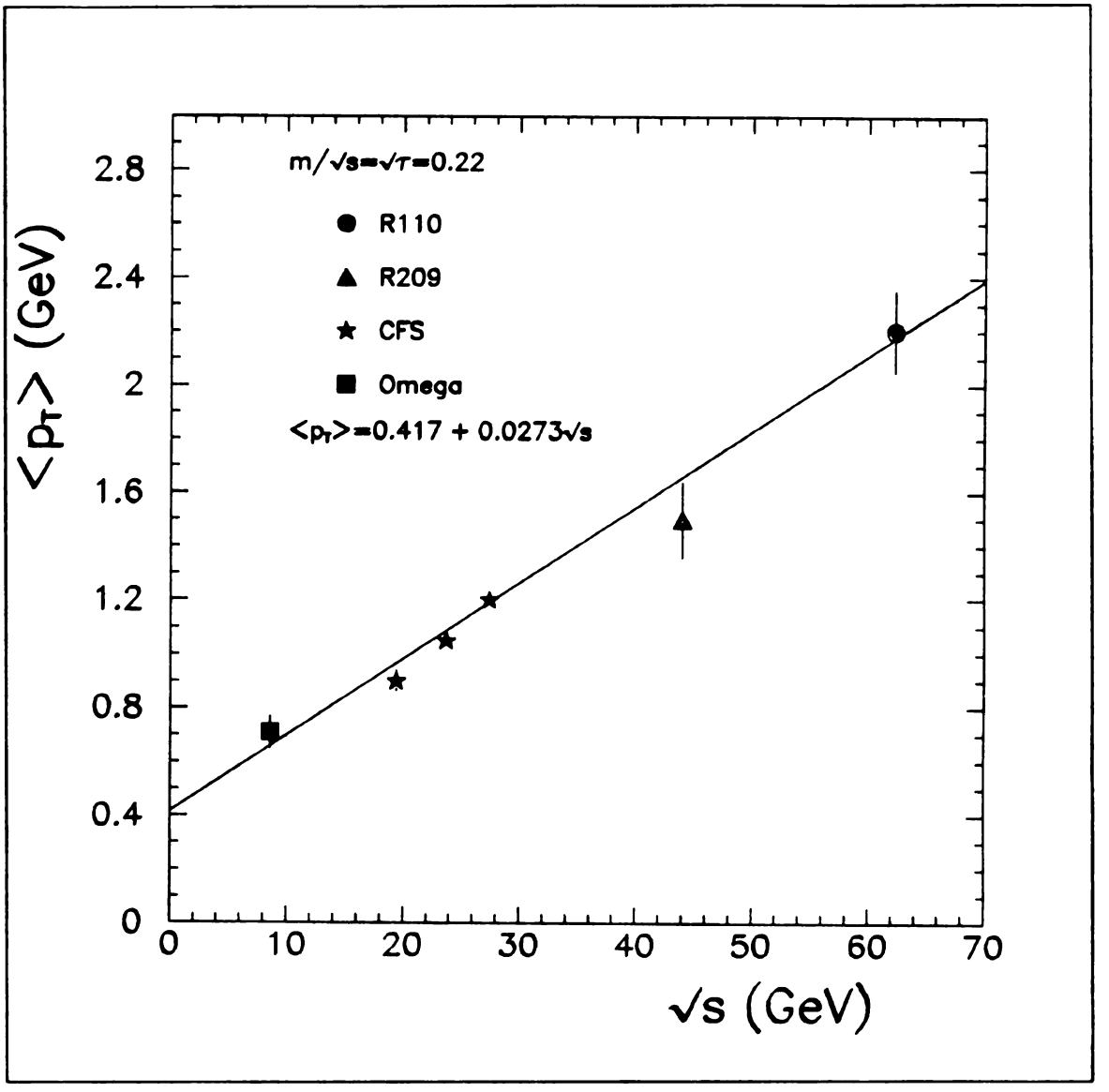

Figure 4.12: $\langle p_T \rangle$ as a function of $\sqrt{s}$

The mean transverse momentum of lepton pairs produced in pp collisions plotted as a function of $\sqrt{s}$. results are shown from CFS[16], R209[12] and the Omega collaboration[24]

that such a scaling form is incompatible with figure 4.12 having $\langle p_T \rangle = \alpha + \beta\sqrt{s}$ with a non-zero intercept.

4.3.1 Single Electron Distributions

The energy, transverse momentum, ϕ, and rapidity distributions of single electrons as measured in the center of mass of the initial protons are shown for the data corrected for efficiencies and Monte Carlo In. The Monte Carlo In comes from events with virtual photons of mass greater than 11 GeV/c^2 and rapidity between -1.2 and 1.2. Also shown are the distributions for the efficiency with arbitrary scale. The distribution for efficiency corrected data and Monte Carlo agree reasonably well except where the efficiency drops off too low for observations to be made in the data. See figures 4.14-4.16.

4.4 Systematic Errors

The Monte Carlo was written in such a way that a number of parameters and distributions could be changed without recompiling and relinking. This helped insure that the correct version of the Monte Carlo was used. This was particularly useful for doing systematic error studies, where only a single parameter needed to be changed.

K Factor

The calculations of the cross section for Drell-Yan pairs from structure functions have always had a problem with normalization. This is due in large part to higher order diagrams involving strong interactions which are difficult to calculate.

Our standard Monte Carlo uses a K factor of 1.70. Since only the lowest order diagram was used in the Monte Carlo, varying the K factor only changed the ratio of the Drell-Yan continuum to the Υ resonances. Using Monte Carlo efficiencies derived assuming K factors of 0.85 and 3.40 changed our measured cross section by only 6%.

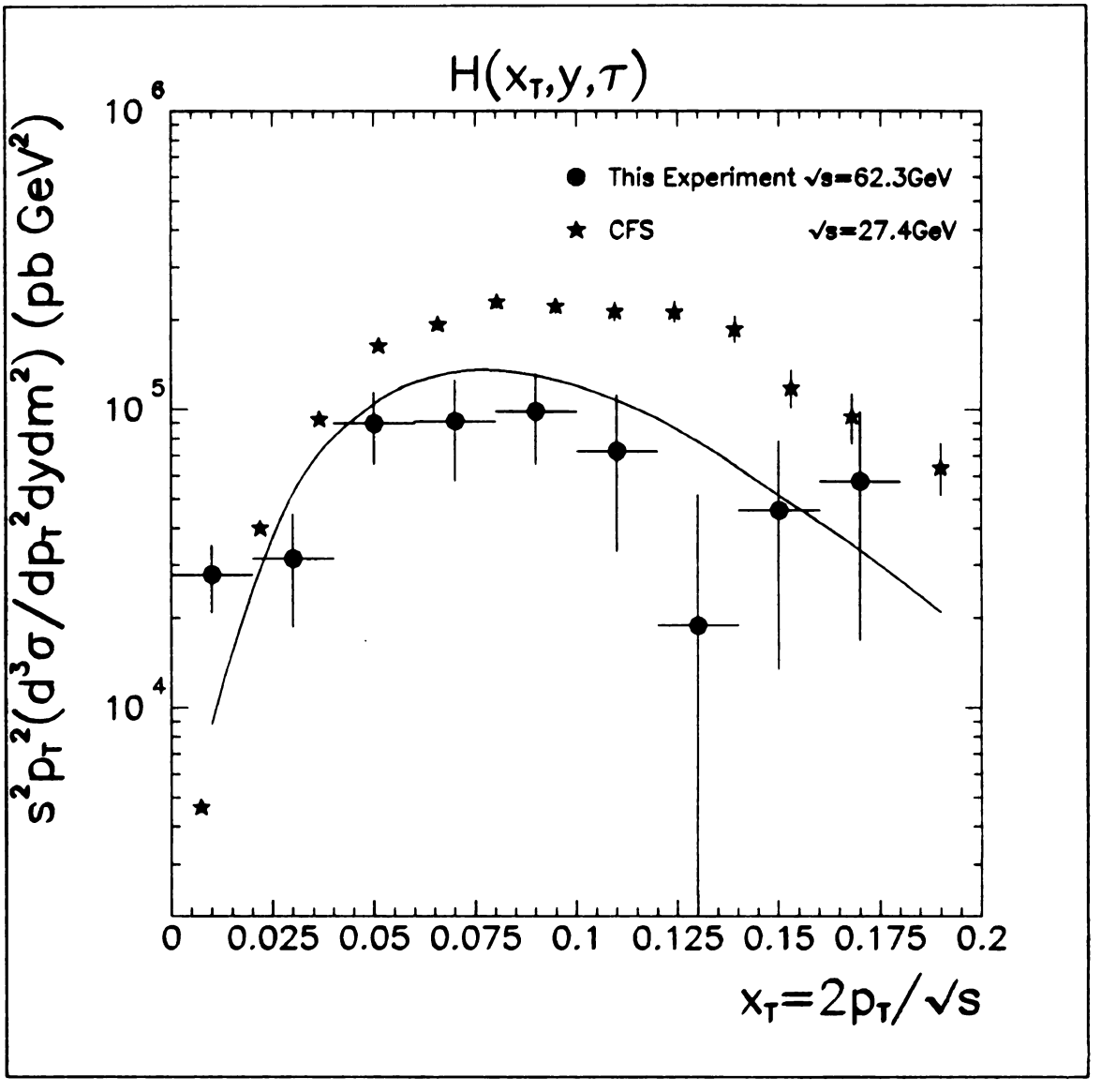

Figure 4.13: $H(x_T, y, \tau)$
The quantity $s^2 p_T^2 (d^3\sigma/dp_T^2 dy dm^2)|_{y=0}$ as a function of $x_T (= 2p_T/\sqrt{s})$

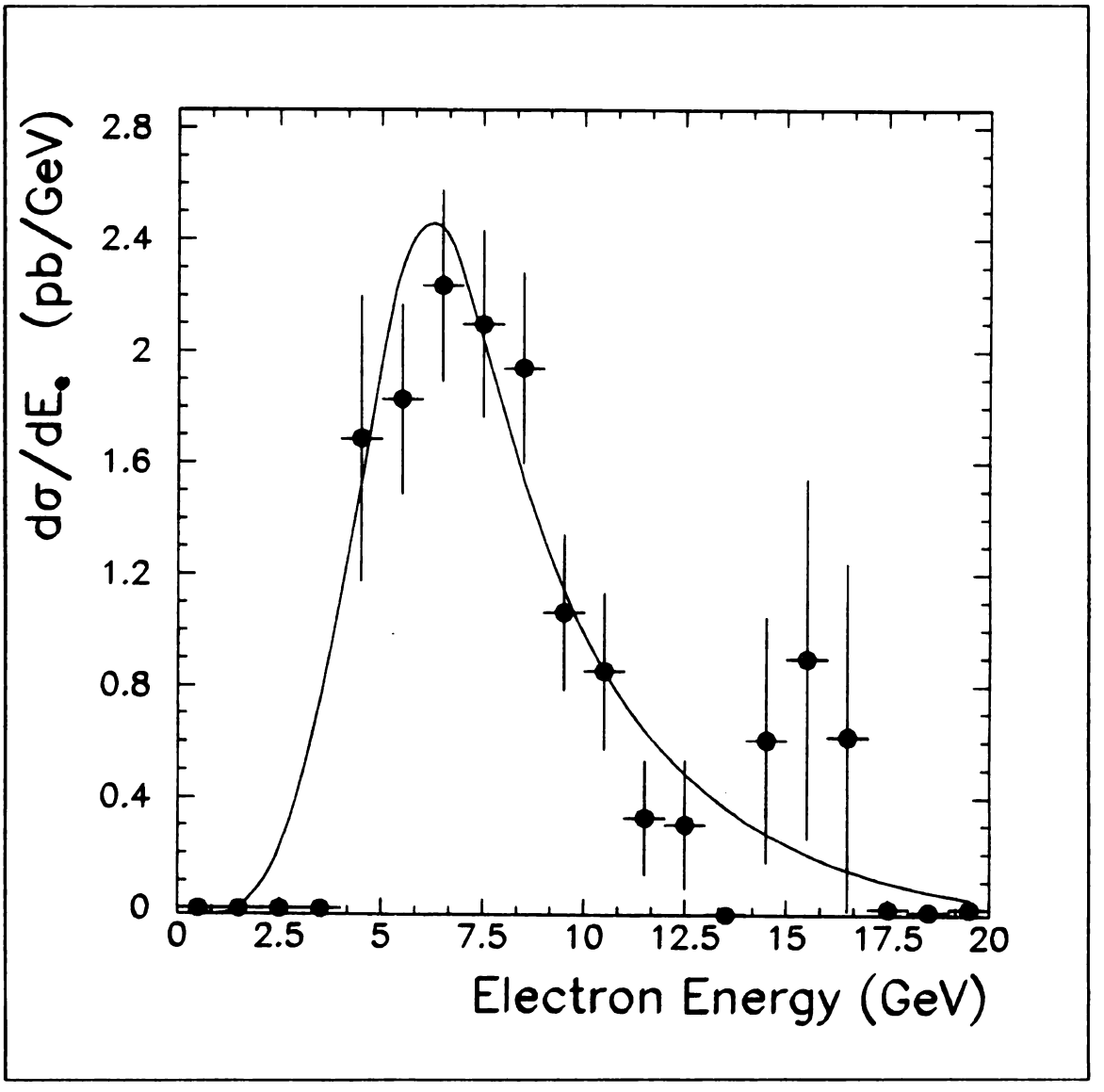

Figure 4.14: The energy distribution of the electrons
The energy distribution for electrons shown for the data with error bars and Monte Carlo In as a curve.

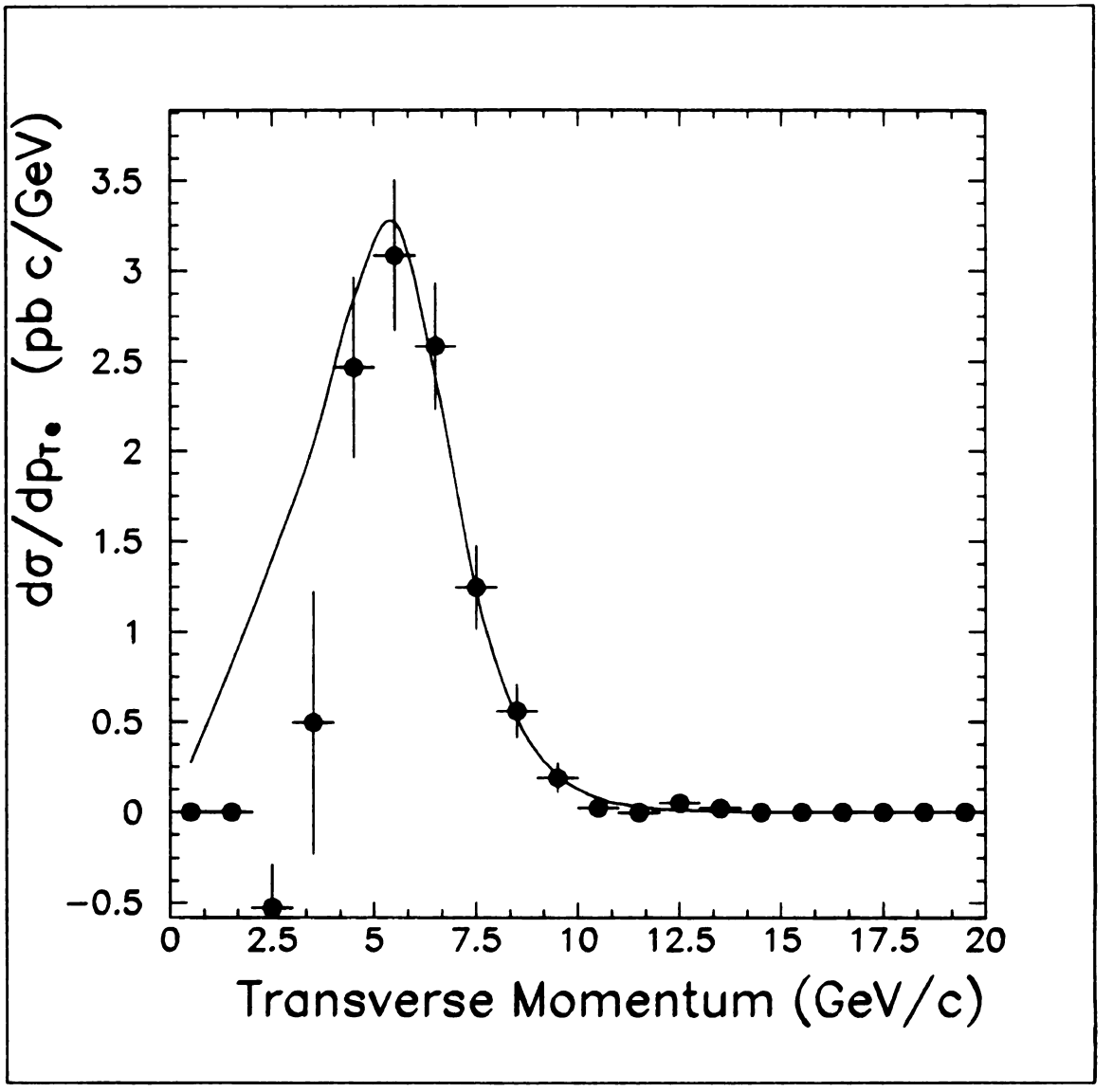

Figure 4.15: The transverse momentum distribution of the electrons
The p_T distribution for electrons shown for the data with error bars and Monte Carlo In as a curve.

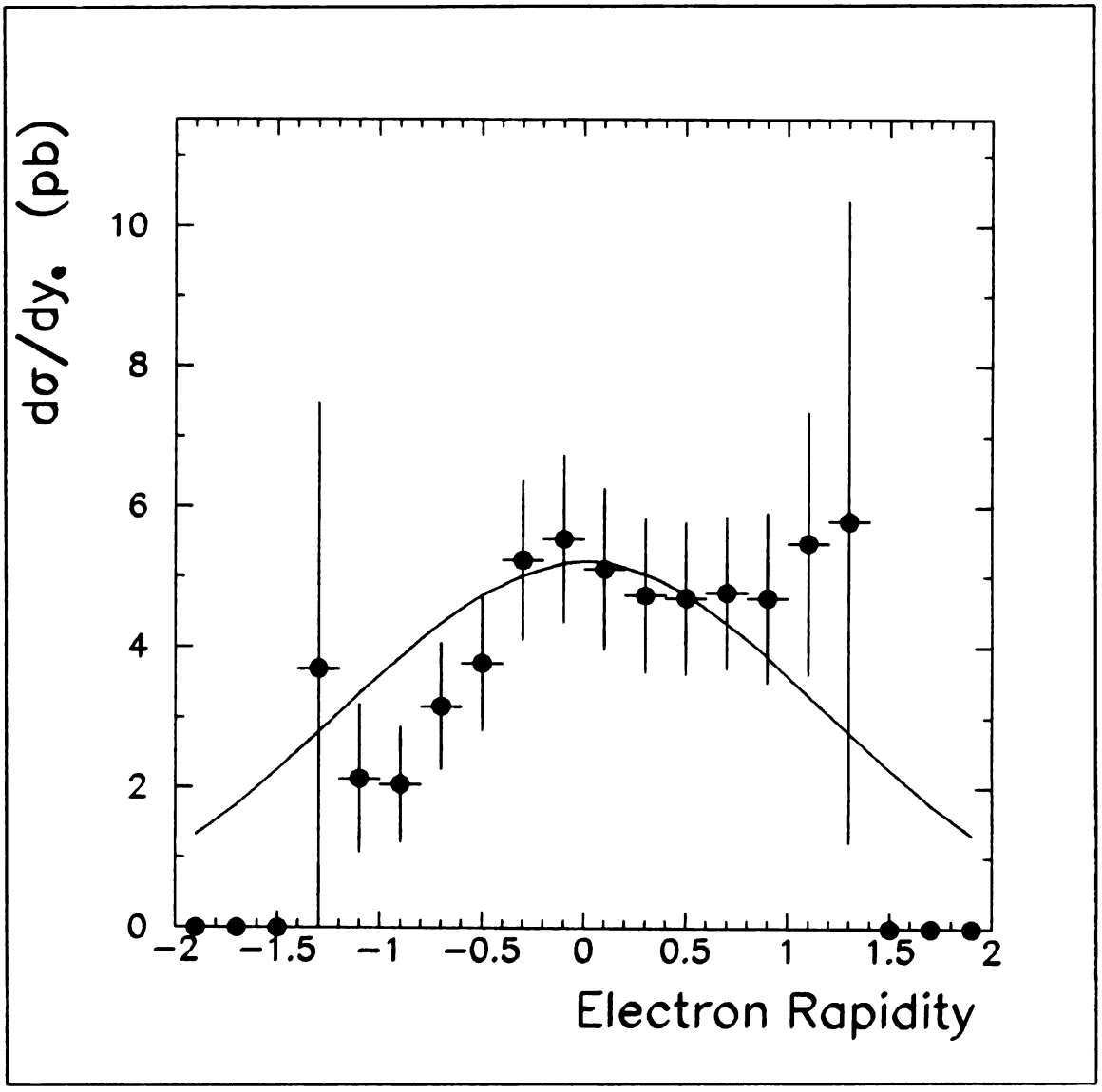

Figure 4.16: The rapidity distribution of the electrons
The rapidity distribution for electrons shown for the data with error bars and Monte Carlo In as a curve.

Parton Densities

The parton distributions in the Monte Carlo were the Duke and Owens set 1 parton distributions. To test for sensitivity to this choice of parton distributions the Monte Carlo was run with Duke and Owens set 2 parton distributions. So that errors due to the K factor were not double counted here the K factor was adjusted so that MC_{in} remains unchanged from the standard. The largest change to the measured cross section came from the Duke and Owens set 2 parton distributions with a difference of 2%.

Energy Resolution

Because the Drell-Yan cross section falls off rapidly as a function of mass, a detector with poor resolution would have observed more events by having allowed low mass events to pass the mass threshold. A change in the resolution in the Monte Carlo of 25% yielded only a 2% change in the measured cross section.

Transverse Momentum Distribution

The average transverse momentum for the electron pairs used in the Monte Carlo was 2.3 GeV/c . When the Monte Carlo was run with an average transverse momentum of 2.0 GeV/c and 2.6 GeV/c, the change in the measured cross section was 3%.

Decay Angle Distribution

A distribution for the decay angle of the virtual photon is of the form

$$1 + \alpha \cos^2 \theta$$

In the Drell-Yan model $\alpha = 1$, and the decay angle is between the lepton and the beam axis. This view is somewhat complicated with the introduction of p_T. Typically, in this case an axis is chosen half way between the beam and target axes [17]. The

Collins-Soper angle, θ_{CS} is the angle between this axis and the electron. With these QCD corrections α is no longer restricted to 1. Since our detector has no coverage at $\cos\theta$ near 1, we can expect acceptance to rise for small α and decrease for large α. Results from the Monte Carlo show a drop of 16% [1] of the cross section for $\alpha = 0$. A rise in the cross section of 13% is seen for $\alpha = 2$.

Geometric Boundaries

The shower counters consisted of 4 sextants with 8 counters in each sextant. Each sextant had edges at some ϕ_1 and ϕ_2, and at z=−75 cm and +75 cm. To confidently determine the acceptance of an event for an electron near the edge was difficult and would have required detailed simulation of the shower shape for a generated event. The Monte Carlo modeled only the average shower shape. As a check, cuts were made in both the data and Monte Carlo far enough away from the edges that the showers were well contained.

For edges in z, electrons' tracks projected to the back of the shower counters were required to have an absolute value in z less than 75 cm (The standard requirement was that for a track to pass through at least 13 cm of the shower counters). This resulted in the signal from the data being reduced by 3%, the efficiency falling by 10% and the cross section rising by 8%.

Edge effects in ϕ were removed by accepting only electrons more than one counter from the edge. The signal from the data was reduced by 15%, the efficiency by 26% and the cross section rose 14%.

Drift Chamber Efficiencies

Earlier versions of the Monte Carlo did not model the drift chambers. Instead an overall track efficiency was used for acceptance correction. It was later discovered

[1] If the acceptance increases, the acceptance corrected cross section from the data drops.

that the *Data* and MC_{out} distributions in ϕ did not match (see figure 4.17). This difference was most evident for the counters nearest the x=0 plane ($\phi = \pm\pi/2$). The reason for the lower acceptance of these counters was that particles may strike them without passing through all 8 planes of the drift chambers, (as can be seen from figure 2.3), and therefore have a low track efficiency. For this reason it was necessary to include the drift chambers in the Monte Carlo. The ϕ distribution of MC_{out} with drift chamber modeling along with *Data* are shown in figure 4.18 and show agreement within errors.

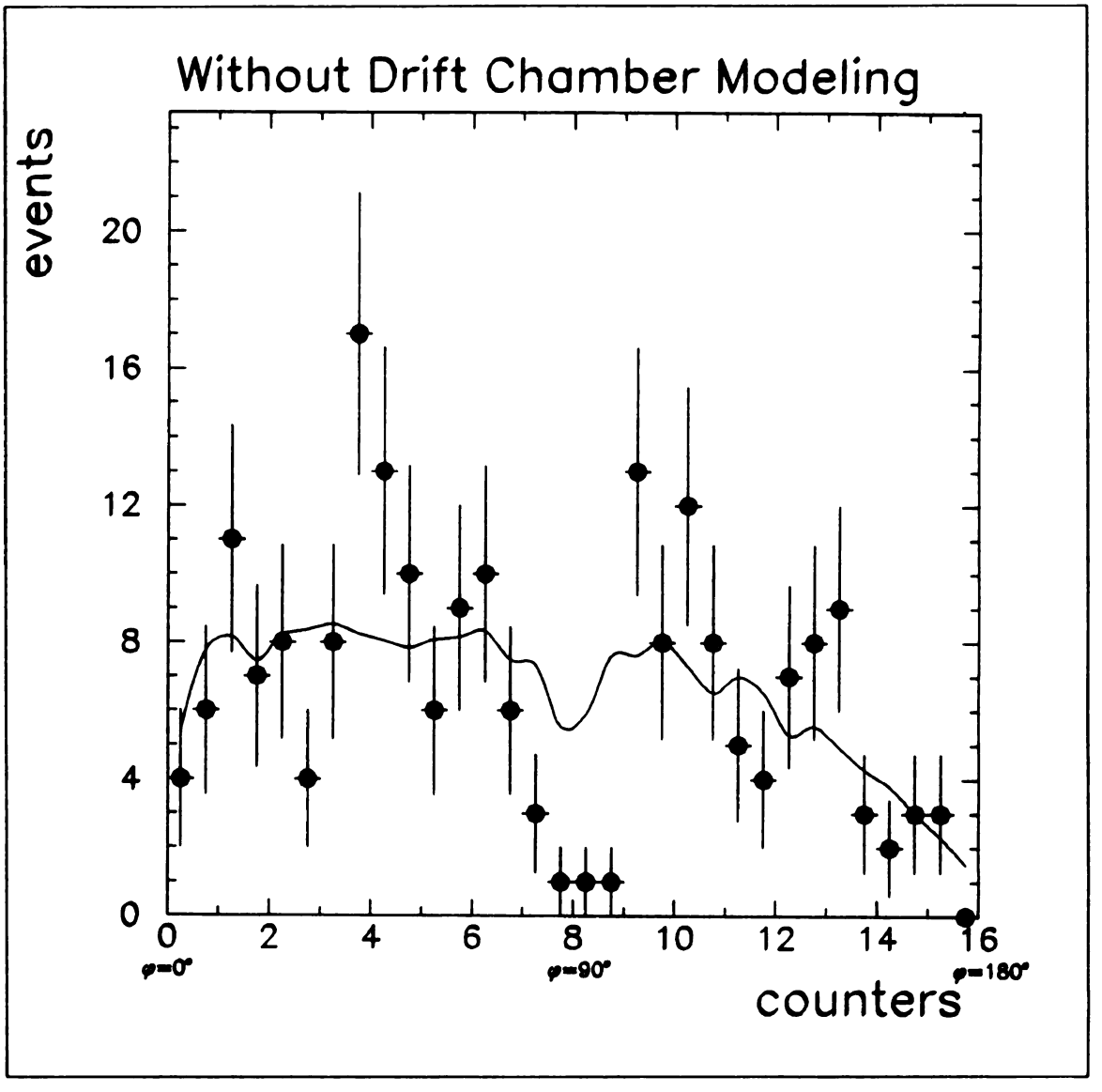

Figure 4.17: Azimuthal angle distributions (before correction)
The distribution in ϕ of the *Data* and MC_{out} without modeling of the drift chambers are shown above. The distribution was folded over at ϕ=0 and has bin size of half a counter. The difference between *Data* and MC_{out} was greatest near $\phi=\pi/2$.

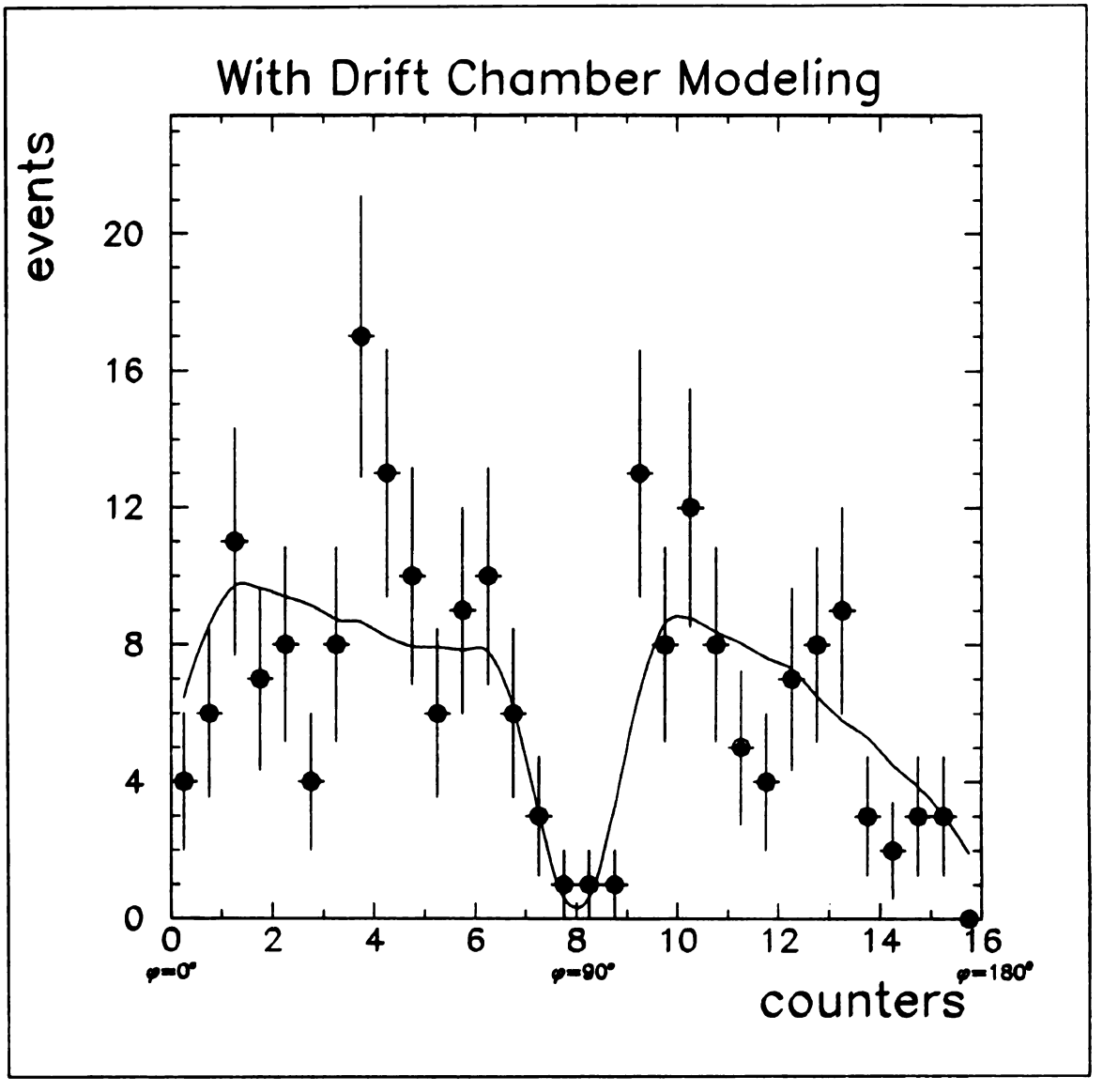

Figure 4.18: Azimuthal angle distributions (after correction)
The distribution in ϕ of the *Data* and MC_{out} are shown above, this time with drift chamber modeling. The distribution was again folded over at ϕ=0 but now has a bin size of a drift chamber cell in the DC1 module. The difference between *Data* and MC_{out} was greatly reduced.

In section 4.1.2 it was stated that the drift chambers were modeled assuming an efficiency of 85% per plane. The value of 85% comes from a study done on minimum ionizing (min-I) particles [10]. The energy in the C compartment, E_C and D compartment, E_D, of the trigger counter of these min-I events was constrained so that

$$36 \text{ MeV} < E_C < 71 \text{ MeV} \quad \text{and} \quad 120 \text{ MeV} < E_D < 200 \text{ MeV}.$$

Furthermore, the adjacent counters were required to have less than 5 MeV (therefore counters at the edge of a sextant were excluded and tracks passed through all 8 planes of the drift chambers). It was determined from these events that the efficiency per track of the drift chambers was 89%±7%. By using equations 4.1.2 and 4.1.2 it can be shown that tracks passing through 8 planes with an efficiency of 85%±4% per plane have an 89%±7% efficiency of activating 6 planes. The limits on the systematic errors from the uncertainty in the efficiency of the drift chambers was found by running the Monte Carlo with the drift chambers plane efficiencies of 90% and 81%.

C and D Counter Balancing

The calibration of the shower counters was done in a 4 GeV electron beam at normal incidence. The counters were scaled so that the total energy observed in the C and D counters equaled 4 GeV. But, since there were two compartments, calibration requires knowing the correct value for $< C/(C+D) >$ as well as the total energy. Unfortunately the value of $< C/(C+D) >$ varied depending on how it was found. The $< C/(C+D) >$ in the first line of table 4.8 were the values used in the calibration. Values from the second line of the table were found using the EGS Monte Carlo [2] [25], and gave the largest values of $< C/(C+D) >$. Data taken by Jakeway and Calder [26], and by Müller [27] measured the shower shape in pure lead. Unlike the shower counter, there were no scintillator or air gaps between layers. Fits were made

[2]The EGS Monte Carlo is a computer program for modeling electromagnetic showers.

with equation 4.11 to their data with $\chi^2/dof = 1.5$ for Jakeway and Calder data, and $\chi^2/dof = 1.8$ for the Müller data. Based on the composition of the shower counters, values for parameters b and Z were found. These values along with the corresponding $< C/(C+D) >$ values are shown in the last line of table 4.8. The first

Table 4.7: Radiation lengths of material

A particle must pass through the beam pipe, the A counters and their support plus an the iron support for the C and D counters before striking the shower counters. Very little energy is deposited in this material because it is at the beginning of the shower, however it does tend to shift the shower so that more energy is deposited in the C counters. Therefore in the Monte Carlo the thickness of the C counters is taken to be 3.87 radiation lengths for the upper counters and 4.04 radiation lengths for the lower counters.

Description	Material	Thickness		
		cm	Radiation Lengths	Interaction Lengths
A counters	polystyrene	0.6	0.014	0.008
Support of A counters	Al	0.2	0.023	0.005
Beam pipes	Titanium	0.1	0.028	0.004
Lower support of shower counters	Fe	0.3	0.170	0.018
Upper support of shower counters	Fe	0.6	0.341	0.036
C counters		3.6	3.609	0.140
	polystyrene	1.6	0.038	0.020
	Pb	2.0	3.571	0.119
D counters		10.8	10.827	0.418
	polystyrene	4.8	0.113	0.060
	Pb	6.0	10.714	0.358

method used in this experiment for calibrating the shower counters took advantage of the fluctuations in the longitudinal shower shape and selected the $\langle C/(C+D) \rangle$ that minimized the energy resolution. The other values came from the EGS Monte Carlo and the parameterization of the longitudinal shower shape (see section 4.1.3). How an incorrect value of $< C/(C+D) >$ would affect the cross section was explored with the Monte Carlo using the equation for the longitudinal shower distribution. The true energy deposited in shower counters was assumed to be that determined from

Table 4.8: Energy balancing in the C and D counters
The upper shower counter were supported by an iron plate 6 mm thick. This plate was only 3 mm thick for the lower shower counter so that the lower shower counters had lower $< C/(C+D) >$. All values of $< C/(C+D) >$ are for normal incidence 4 GeV electrons. The values of b and Z were chosen so that $< C/(C+D) >$ match calibration values in the first line and results of an EGS Monte Carlo in line two. For the next three lines the values for b and Z are the result of a fit to data by Jakeway and Calder [26], and Müller [27]. In the final line b and Z are found based on the composition of the shower counters (see section 4.1.3).

Description	b	Z	3 mm Fe $< C/(C+D) >$	6 mm Fe $< C/(C+D) >$
Calibration	0.4	30.5	0.275	0.295
Jakeway	0.426	52.6	0.230	0.248
Müller	0.465	57.2	0.221	0.241
From Material Composition	0.5	76.8	0.195	0.214

equation 4.11. Coefficients for the C and D counters were chosen to match calibration requirements (C and D counters sum to 4 GeV, and $< C/(C+D) >$ equal 0.295 for upper counters and 0.275 for lower counters for a 4 GeV beam at normal incidence). These constants were then used to find the energy observed in the detector. Using different sets of values for parameters b and Z, taken from table 4.8, different shower shapes were tested. (see Table 4.9).

4.4.1 Summary of Systematic Errors

An estimate of the total systematic error is found from the sum of the squares of the percentage change for each parameter varied in table 4.9. Therefore

$$\Delta_T^2 = 5^2 + 2^2 + 3^2 + 8^2 + 14^2 + 16^2 + 24^2 + 9.5^2$$

or

$$\Delta_T = 35\%.$$

Including statistical error the total cross section is therefore found to be $7.25 \pm 0.73 \pm 2.5$ pb.

Table 4.9: Systematic Errors

Systematic Errors	Monte Carlo In pb	Monte Carlo Out pb	Signal Number of Events	Total Cross Section pb	% Change From Standard
Standard	7.27	0.589	99	7.25	0
K factor = 1.50 in the Monte Carlo	6.41	0.523	99	7.21	-5
K factor = 1.90 in the Monte Carlo	8.12	0.657	99	7.28	3
Duke and Owens parton distributions set 2	7.27	0.594	99	7.41	2
$\Delta E_e = 0.0\sqrt{E}$	7.26	0.569	99	7.51	3
$\Delta E_e = 0.075\sqrt{E}$	7.26	0.578	99	7.30	2
$\Delta E_e = 0.20\sqrt{E}$	7.26	0.600	99	7.12	-2
Υ Off	7.27	0.567	99	7.54	4
$\langle p_T = 2.0 \rangle$	7.26	0.609	99	7.01	3
$\langle p_T = 3.0 \rangle$	7.27	0.545	99	7.84	8
projection of electron tracks must be within 75 cm at back of shower counters	7.27	0.528	94	7.86	8
remove outer shower counters in each sextant	7.27	0.437	82	8.26	14
α= 0 in $\cos\theta$ distribution	7.27	0.704	99	6.07	-16
α= 2 in $\cos\theta$ distribution	7.27	0.523	99	8.18	13
Drift Chamber Efficiencies of 96%	7.27	0.711	99	6.02	-17
Drift Chamber Efficiencies of 82%	7.27	0.475	99	8.99	24
Shower Balancing Jakeway and Calder	7.27	0.603	99	7.12	-2.1
Shower Balancing Müller	7.27	0.607	99	7.11	-2.1
Shower Balancing Calibration	7.27	0.561	99	7.96	9.5

Chapter 5

Associated Particles

5.1 Associated Particle Acceptance

A search was made for evidence of an associated jet by studying particles produced in the same event as the electron pair. Clusters of neutral energy observed in the lead glass and shower counters were assumed to be π^0's, and charged particles in the drift chambers were assumed to be charged pions. Only particles with energy greater than 0.2 GeV were considered. Charged particles were required to project back to the electron-pair vertex. The acceptance in rapidity, y, for charged particles was $-1.2 < y < +1.2$ over the full azimuth, ϕ. The acceptance for π^0's was $-0.6 < y < +0.6$ over the lead-glass acceptance ($\delta\phi = 114°$) and $-1.1 < y < +1.1$ over the shower counter acceptance ($\delta\phi = 200°$). The multiplicity of an event was defined as the number of charged and neutral particles satisfying the above requirements, excluding the two electrons. These multiplicities were not corrected for apparatus effects.

5.2 Associated Particle Distributions

Over a third of the events in this sample are expected to arise from higher order diagrams (see figure1.2) and thus be accompanied by associated particles. The virtual gamma in these events should have higher transverse momentum since it will be recoiling off either the gluon or quark. Simple Drell-Yan is expected to contribute only at low transverse momentum. Therefore as p_T of the virtual photon increases

one should see

1. an increase in the number of particles in the event
2. an increase in the number of particles in the opposite transverse direction of the gamma
3. an increase in the transverse momentum of the vector sum of the associated particle.

These effects will be diluted due to the finite rapidity acceptance of the detector.

In figure 5.1 indeed the multiplicity of the associated particles can be seen to rise with transverse momentum of the electron pair, in agreement with earlier observations at the ISR in conjunction with muon pairs [28]. This may be interpreted as evidence that low values of transverse momentum are less likely to be associated with a recoil jet. The mean multiplicity shows no strong dependence as a function of mass (see figure 5.2).

The difference in azimuth, Φ, between momenta of the associated particle and the electron pair was found. The distribution of Φ is shown in figure 5.3 with the data split between electron pairs with transverse momentum less than 2 GeV/c and those with more. There is no strong variation in the Φ distribution for $p_T < 2$ GeV/c, but for $p_T > 2$ GeV/c associated particles are produced predominantly at large Φ, that is back-to-back with the electron pair. Events with electron pair transverse momentum less than 2 GeV/c show little or no variation with Φ, whereas for $p_T > 2$ GeV/c the distribution show a rise at large Φ. The data presented in figures 5.1 and 5.3 imply that low transverse momentum electron pairs are produced by the basic Drell-Yan process with associated particles arising only from spectator jets. As the transverse momentum of the electron pairs increases, more associated particles are seen concentrated in the central region and furthermore they tend to recoil against the electron pair. This is consistent with the increasing importance of second order diagrams involving a recoil jet in the production of lepton pairs of increasing transverse momentum.

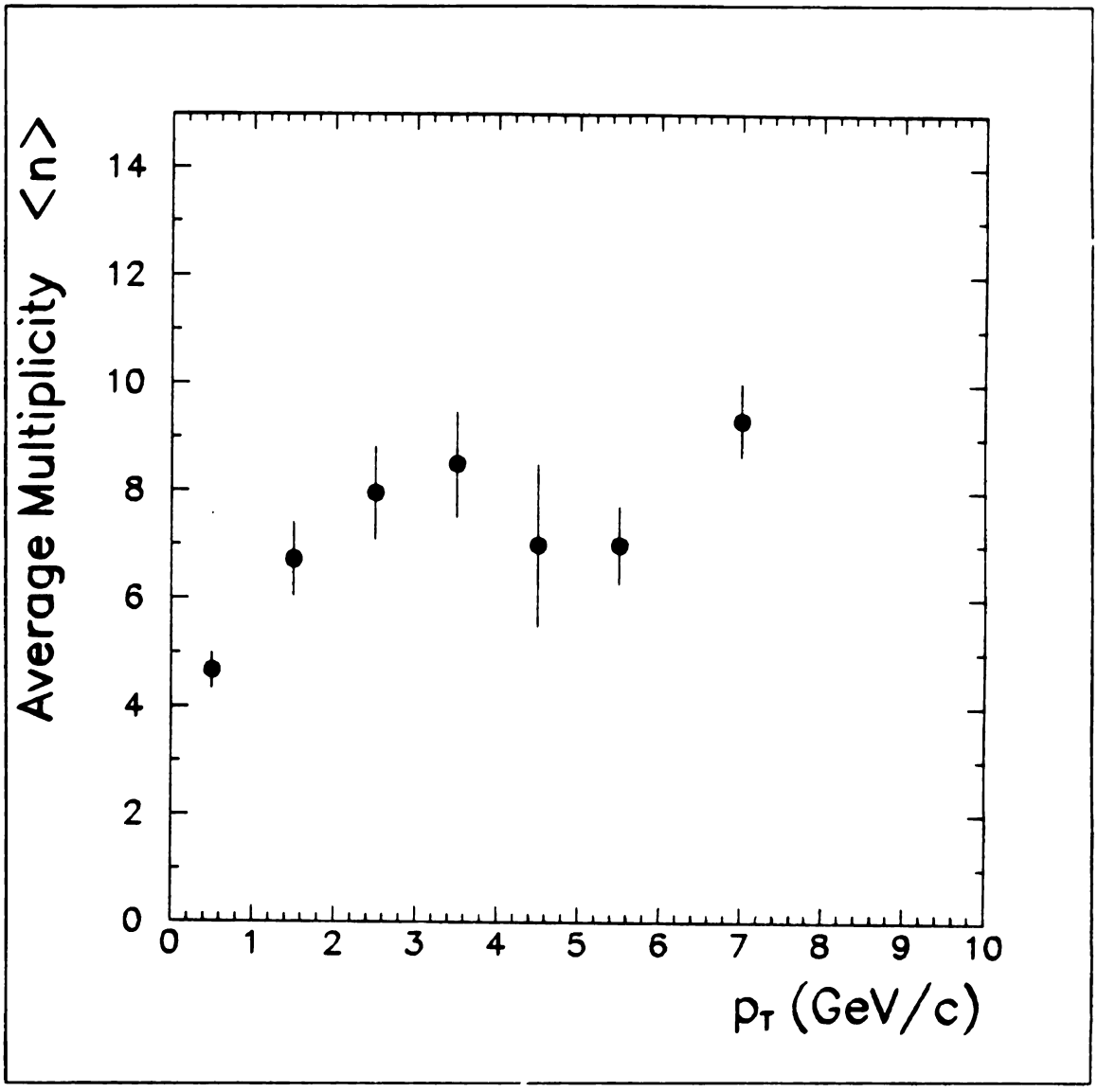

Figure 5.1: The mean multiplicity as a function of the transverse momentum The mean multiplicity increases as a function of p_T of the electrons pair.

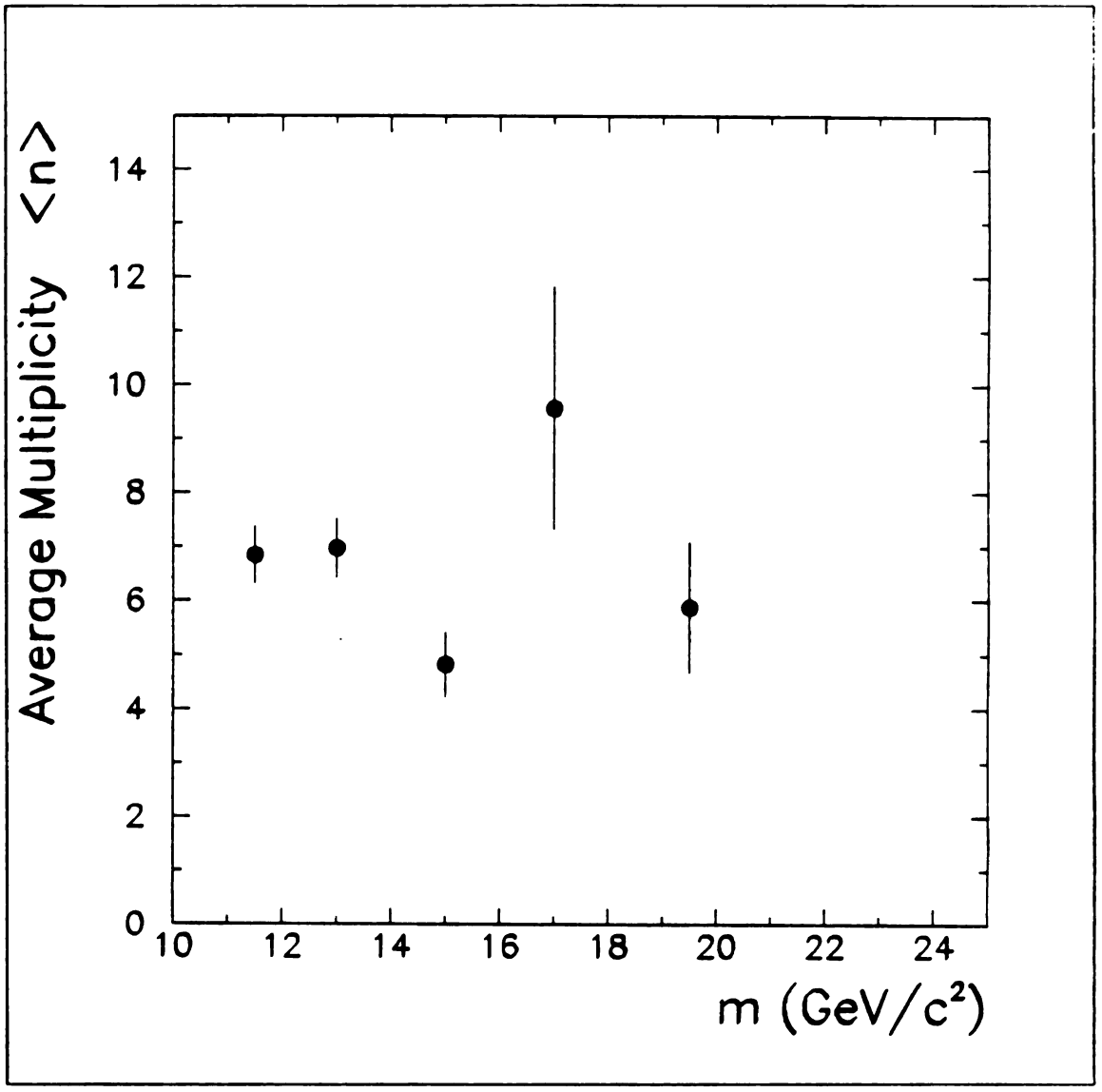

Figure 5.2: The mean multiplicity as a function of the invariant mass
No dependence of the multiplicity is seen as a function of mass.

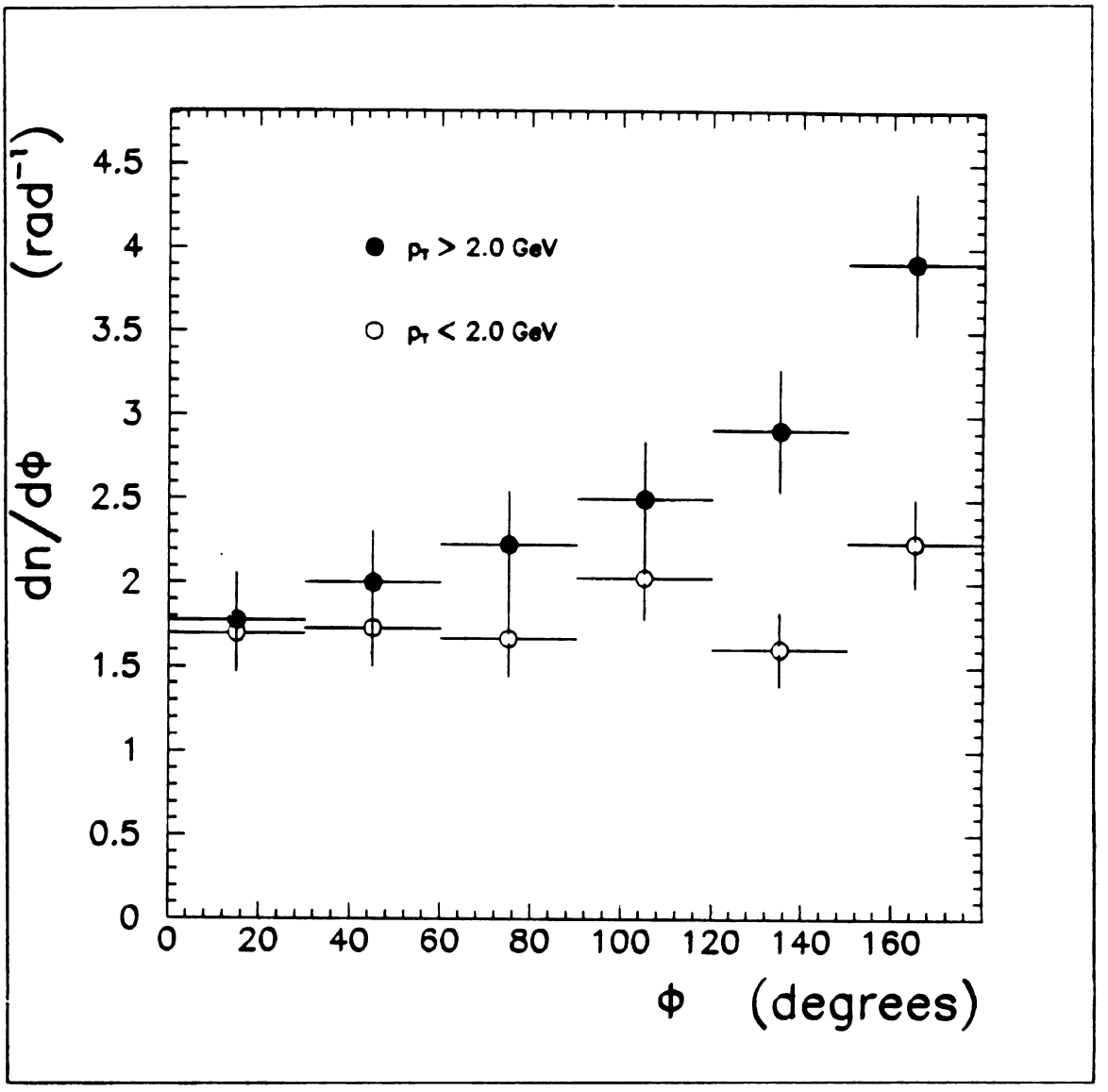

Figure 5.3: $dn/d\Phi$

The distribution for Φ, the difference in azimuth between the transverse momentum of an associated particle, and the momentum of the electron pair, is shown above a) for electron pairs with p_T < 2 GeV and b) for electron pairs with p_T > 2 GeV.

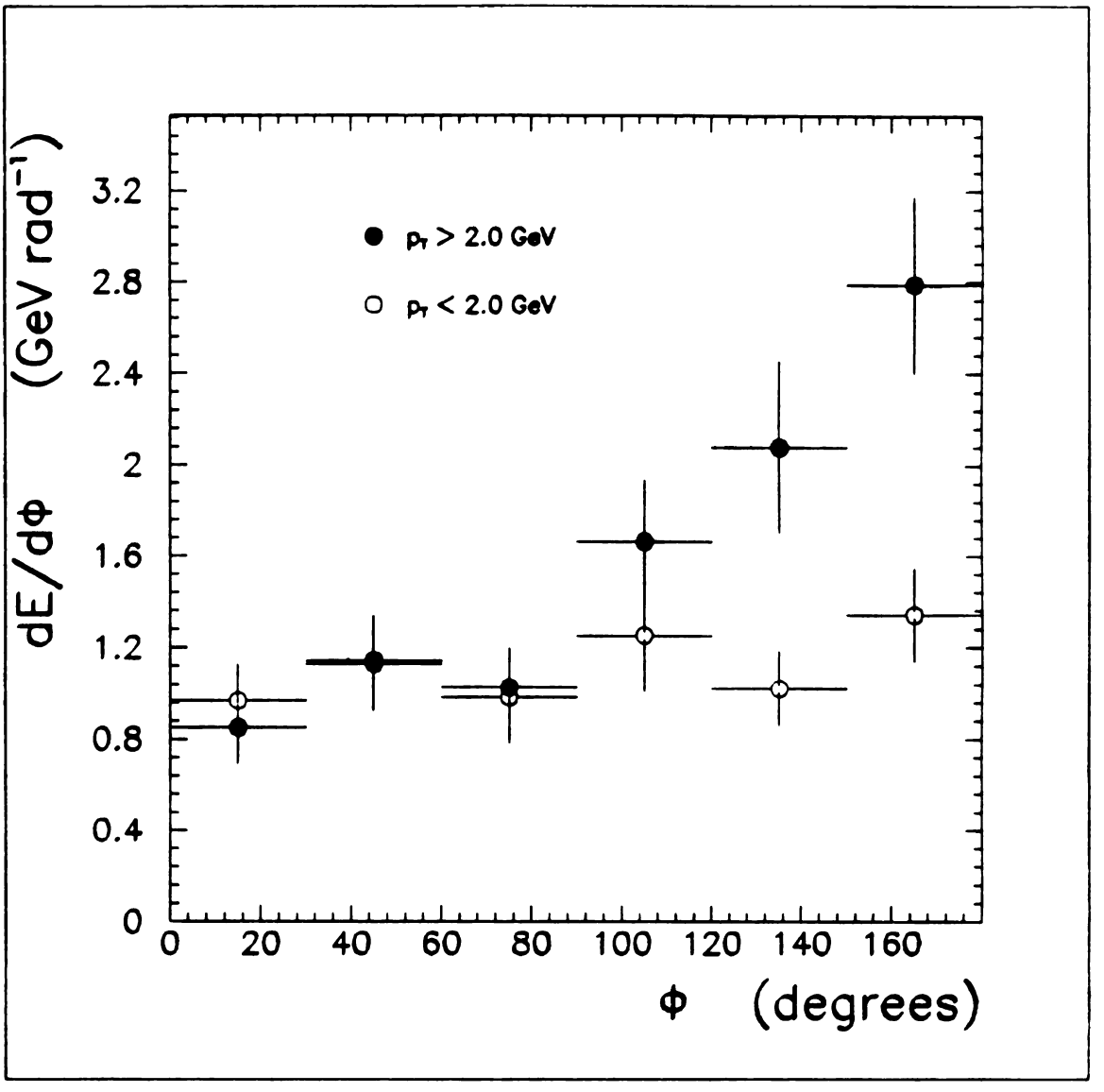

Figure 5.4: $dE/d\Phi$

The energy distribution of the associated particles as a function Φ is shown above a) for electron pairs with $p_T < 2$ GeV and b) for electron pairs with $p_T > 2$ GeV.

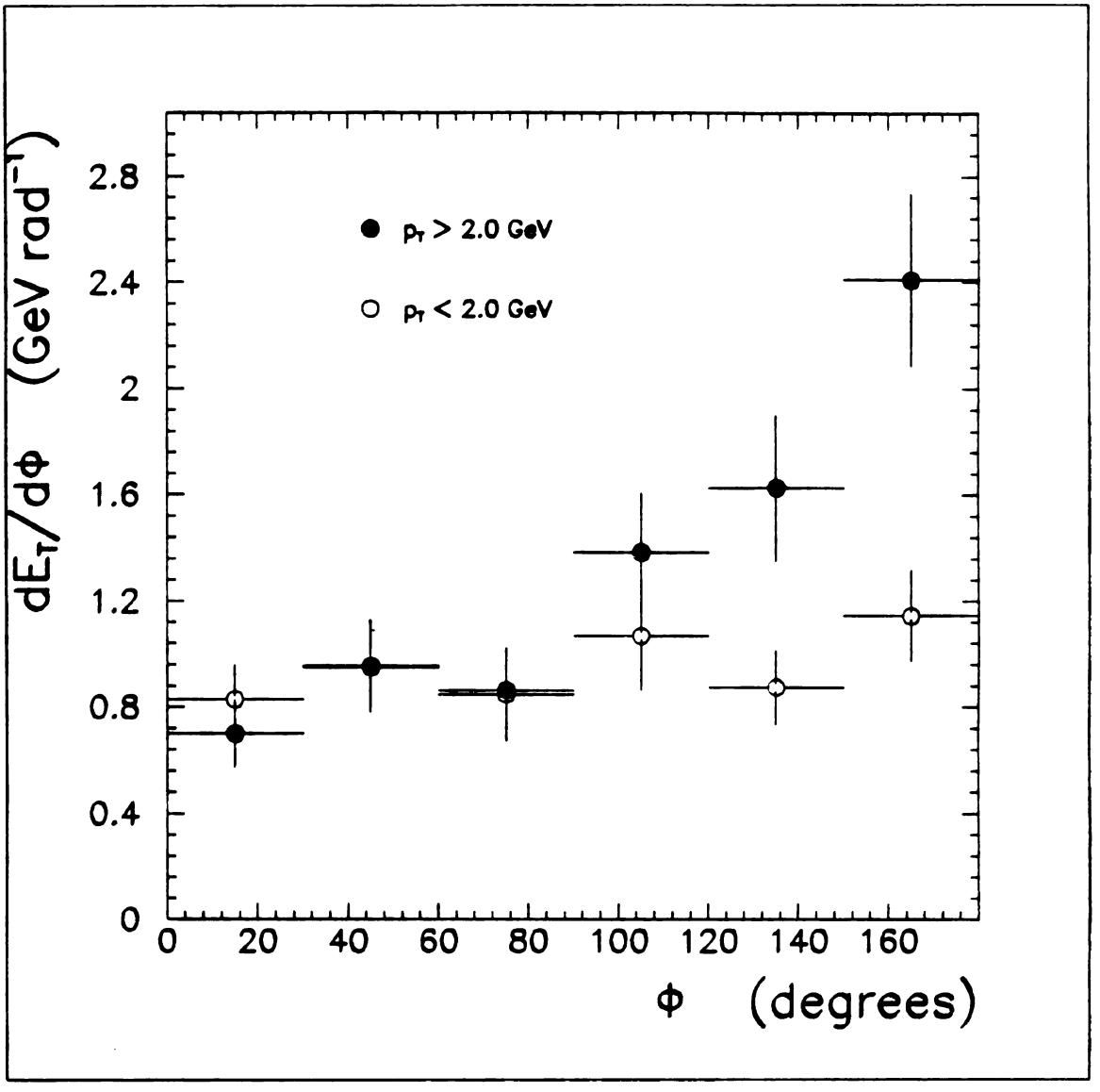

Figure 5.5: $dE_T/d\Phi$

The transverse energy distribution of the associated particles as a function Φ is shown above a) for electron pairs with $p_T < 2$ GeV and b) for electron pairs with $p_T > 2$ GeV.

Energy (figure 5.4) and transverse momentum (figure 5.5) weighted Φ distributions show similar results.

The vector $\vec{p_j}$ of an event was formed by summing the momenta of the associated particles. The difference in azimuth, Φ_j, between the transverse momentum of the electron pair and $\vec{p_T j}$ was found. The distribution of Φ_j, again with data split between electron pairs with transverse momentum above and below 2 GeV/c. Since there only 105 opposite sign events the statistical error is fairly large. The distributions for $p_T <$ 2.0 GeV/c whether plotted with a weight of one, the energy sum or the transverse energy sum show no dependence in Φ_j (figure 5.6, 5.7 and 5.5). Distributions with $p_T > 2$ GeV/c show an increase at large Φ_j.

The transverse momentum correlations between the electron pair and the associated particles were examined in the two-dimensional plot of p_{Tj}, the transverse momentum of the vector sum of the associated particles, versus p_T of the electron pair(figure 5.9). The value for the sample correlation coefficient [1] was found to be 0.38. The correlation observed between the two variables is what might be expected if a recoil jet were present. This correlation can be seen in figure 5.10, where the mean transverse momentum of the system of associated particles, $\langle p_{T_j} \rangle$, is plotted as a function of p_T and again in figure 5.11 where the mean transverse momentum of the electron pair is plotted as a function of $\langle p_{T_j} \rangle$. A completely contained jet with perfect resolution might be expected to have $\langle p_{T_j} \rangle$ equal to p_T, while imperfect jet containment would result in lower slope. Figure 5.10 clearly departs from the idealized situation, especially at low p_T where the presence of spectator particles would dilute the effect of the jet. In an attempt to combine the azimuthal correlation and momentum balancing information, we constructed $-p_{T_j} \cos \Phi_j$. The two-dimensional plot of this variable versus p_T of the electron pair is shown in figure 5.12. The value for the sample correlation coefficient for this plot was found to 0.46. For the vari-

[1] An anti-correlated sample would have a value of -1. An uncorrelated sample would have a value of 0. And a correlated sample would have a value of 1.

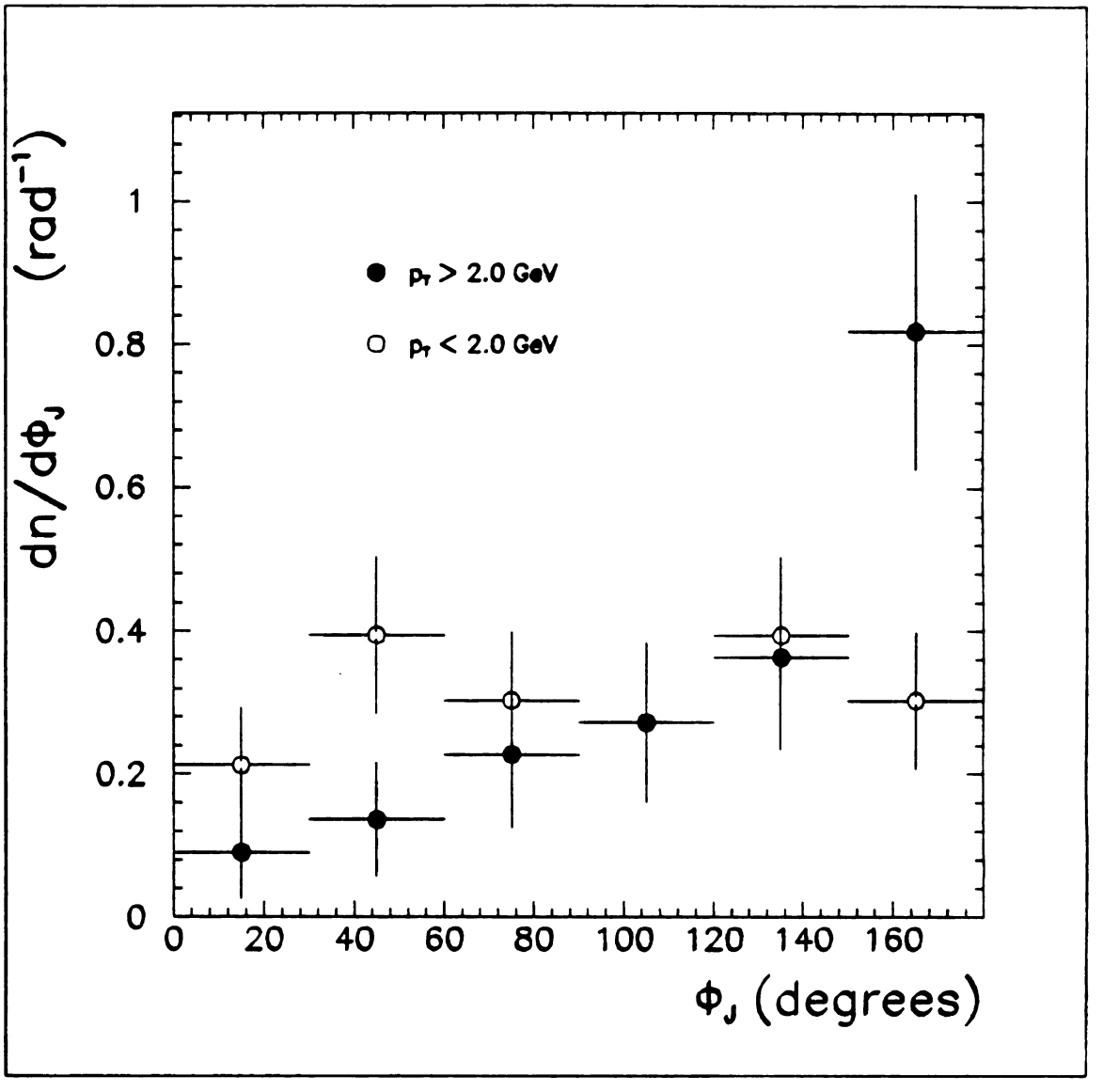

Figure 5.6: $dn/d\Phi_j$

The distribution for Φ_j, the difference in azimuth between the vector sum of the momentum of an associated particle, and the momentum of the electron pair, is shown above a) for electron pairs with $p_T < 2$ GeV and b) for electron pairs with $p_T > 2$ GeV.

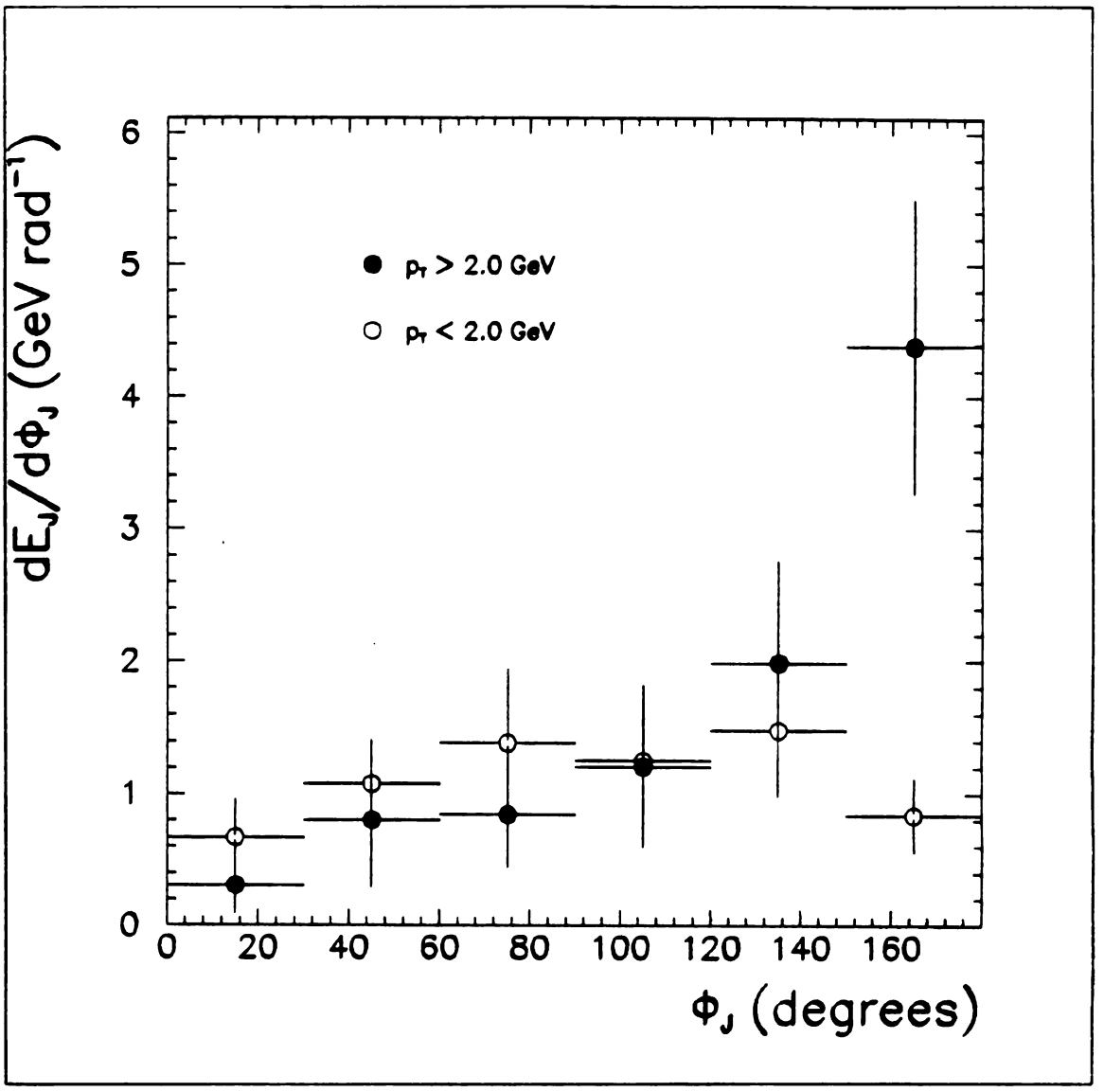

Figure 5.7: $dE_j/d\Phi_j$

The energy distribution of the associated particles as a function Φ_j is shown above a) for electron pairs with $p_T < 2$ GeV and b) for electron pairs with $p_T > 2$ GeV.

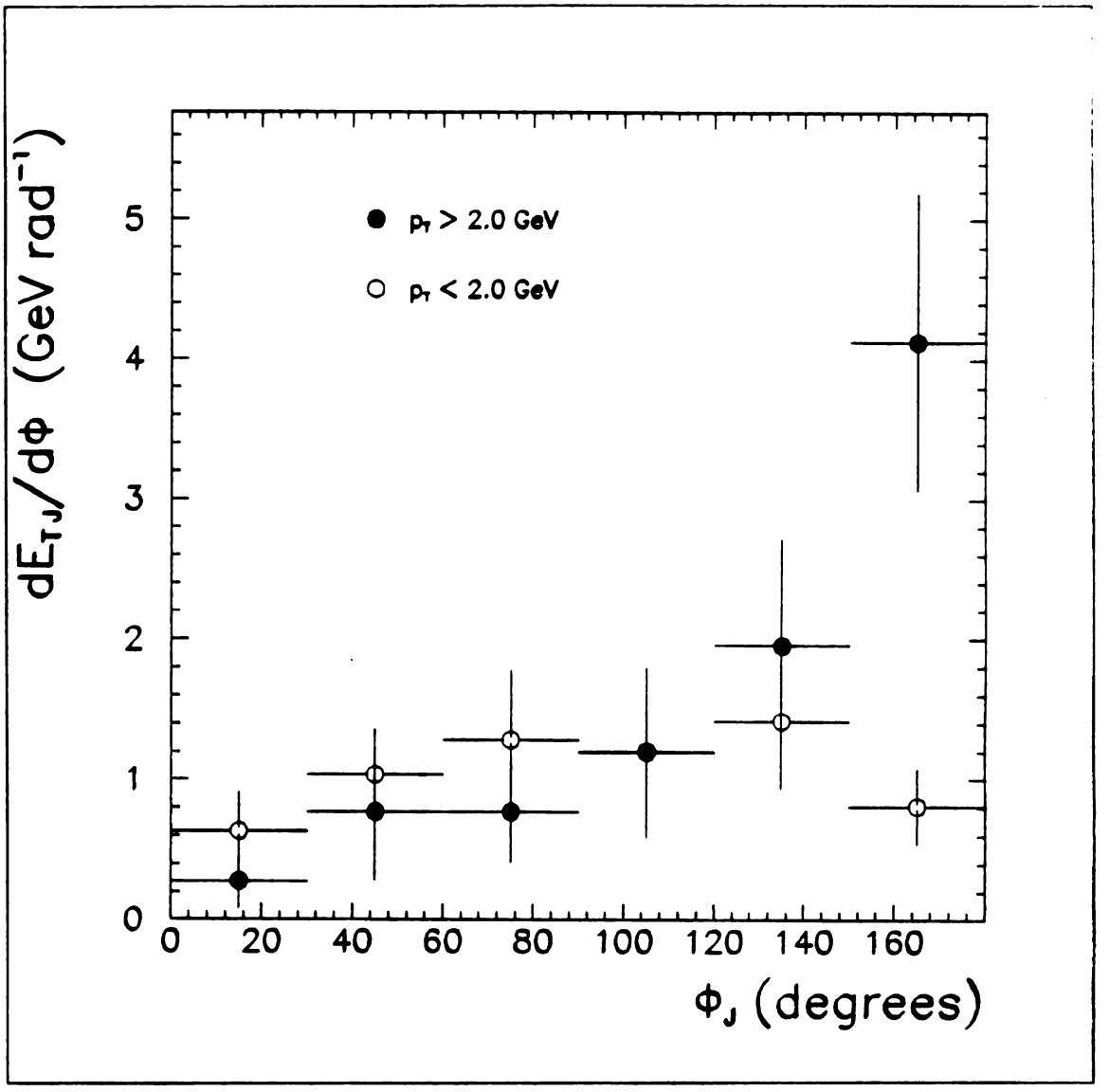

Figure 5.8: $dE_{Tj}/d\Phi_j$

The transverse energy distribution of the associated particles as a function Φ_j is shown above a) for electron pairs with $p_T < 2$ GeV and b) for electron pairs with $p_T > 2$ GeV.

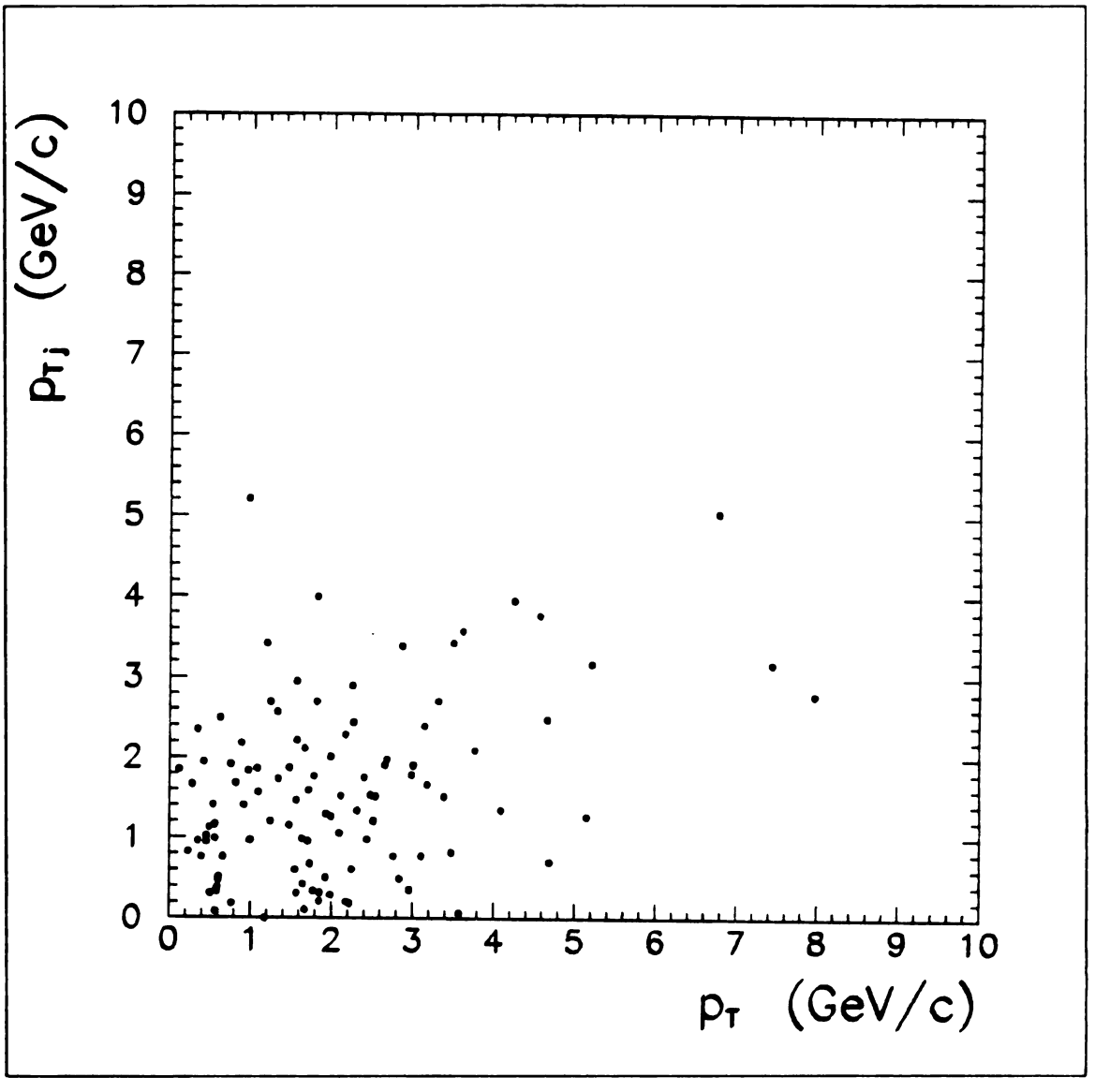

Figure 5.9: p_{Tj} versus p_T

The net transverse momentum of the associated particles versus the the transverse momentum of the electron pair.

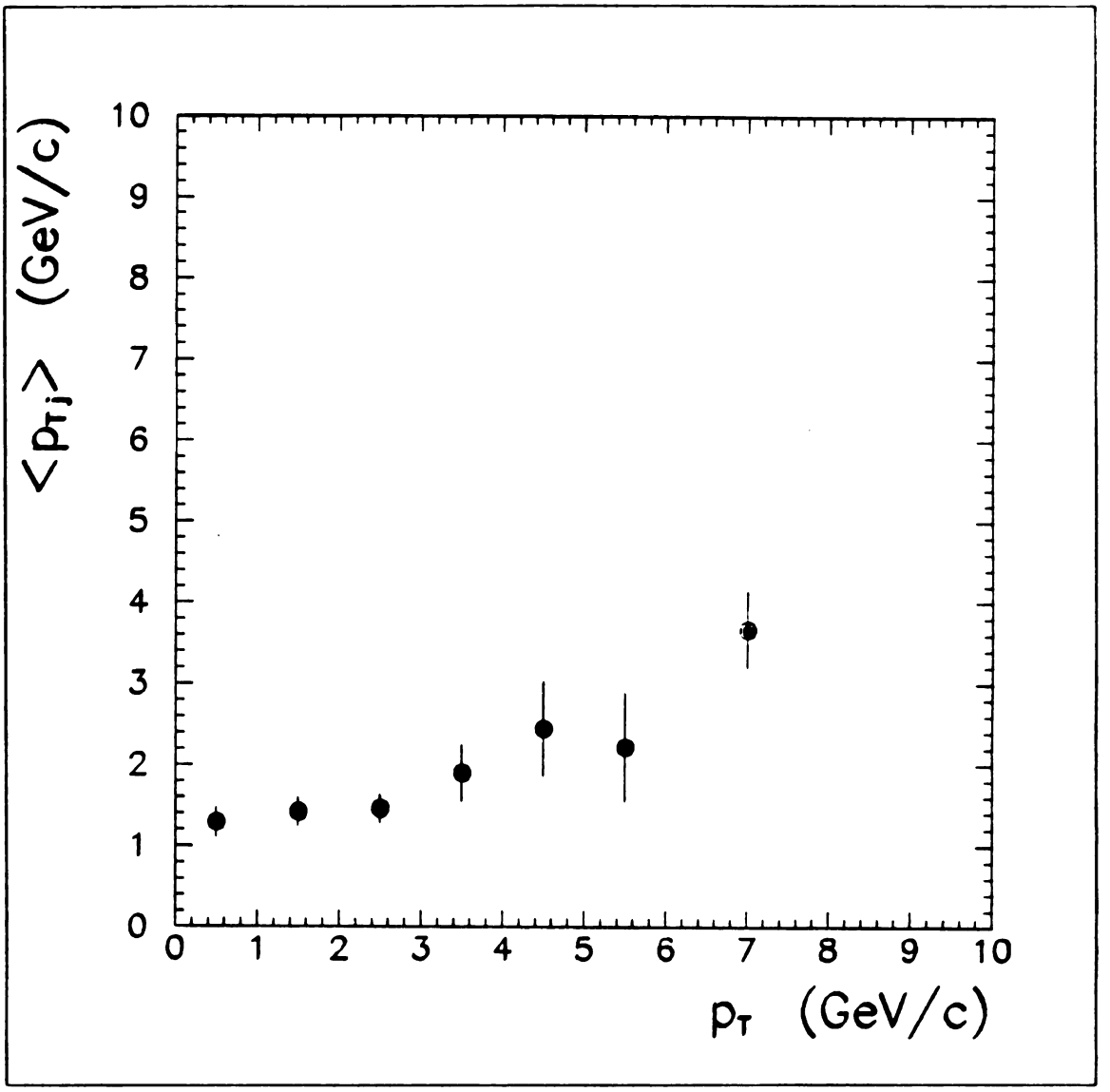

Figure 5.10: $\langle p_{Tj} \rangle$ as a function of p_T

The mean transverse momentum of the associated particles as a function of the transverse momentum of the electron pair.

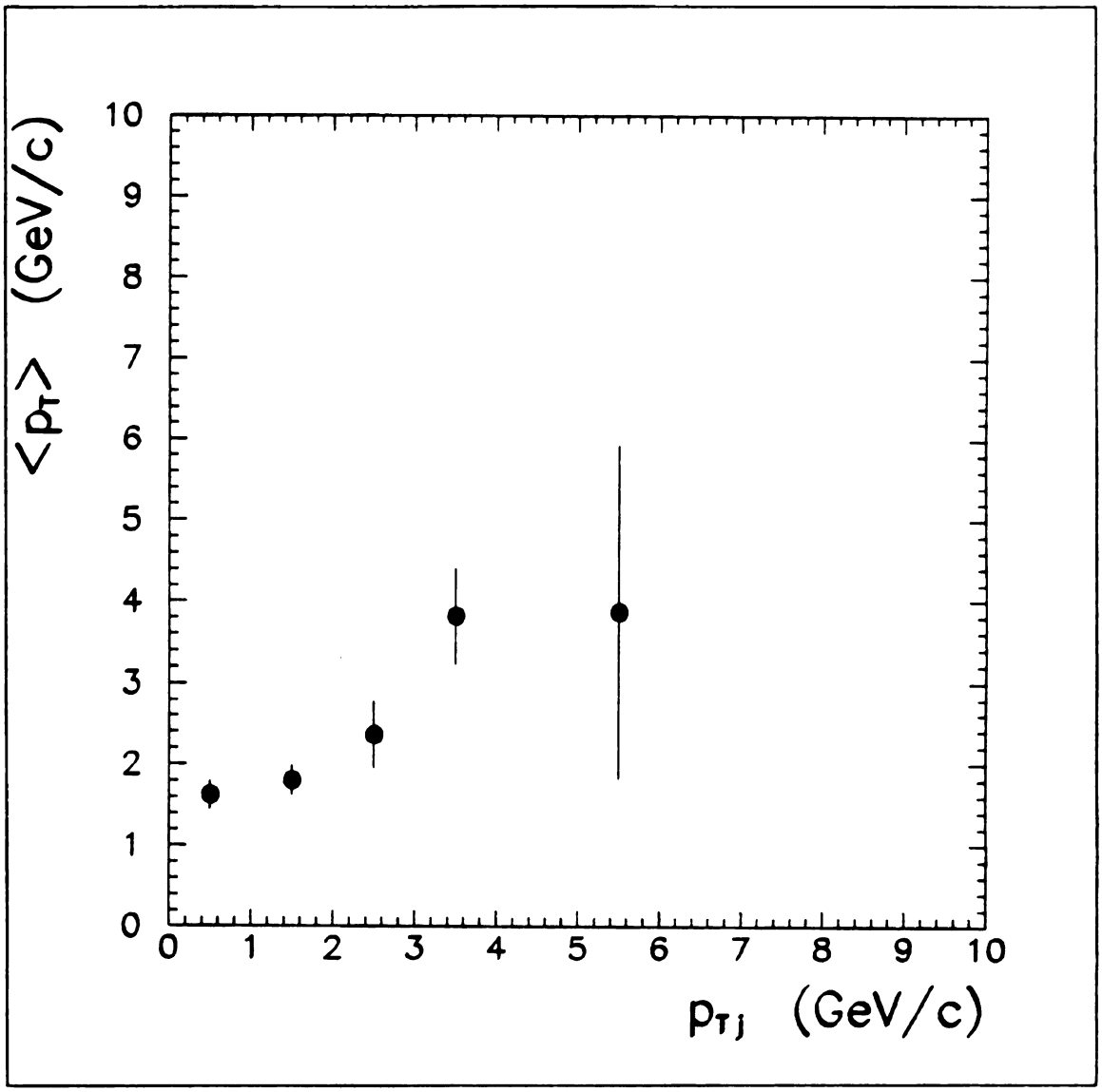

Figure 5.11: $\langle p_T \rangle$ as a function of $p_T j$

The mean transverse momentum of the electron pair as a function of the transverse momentum of the associated particles.

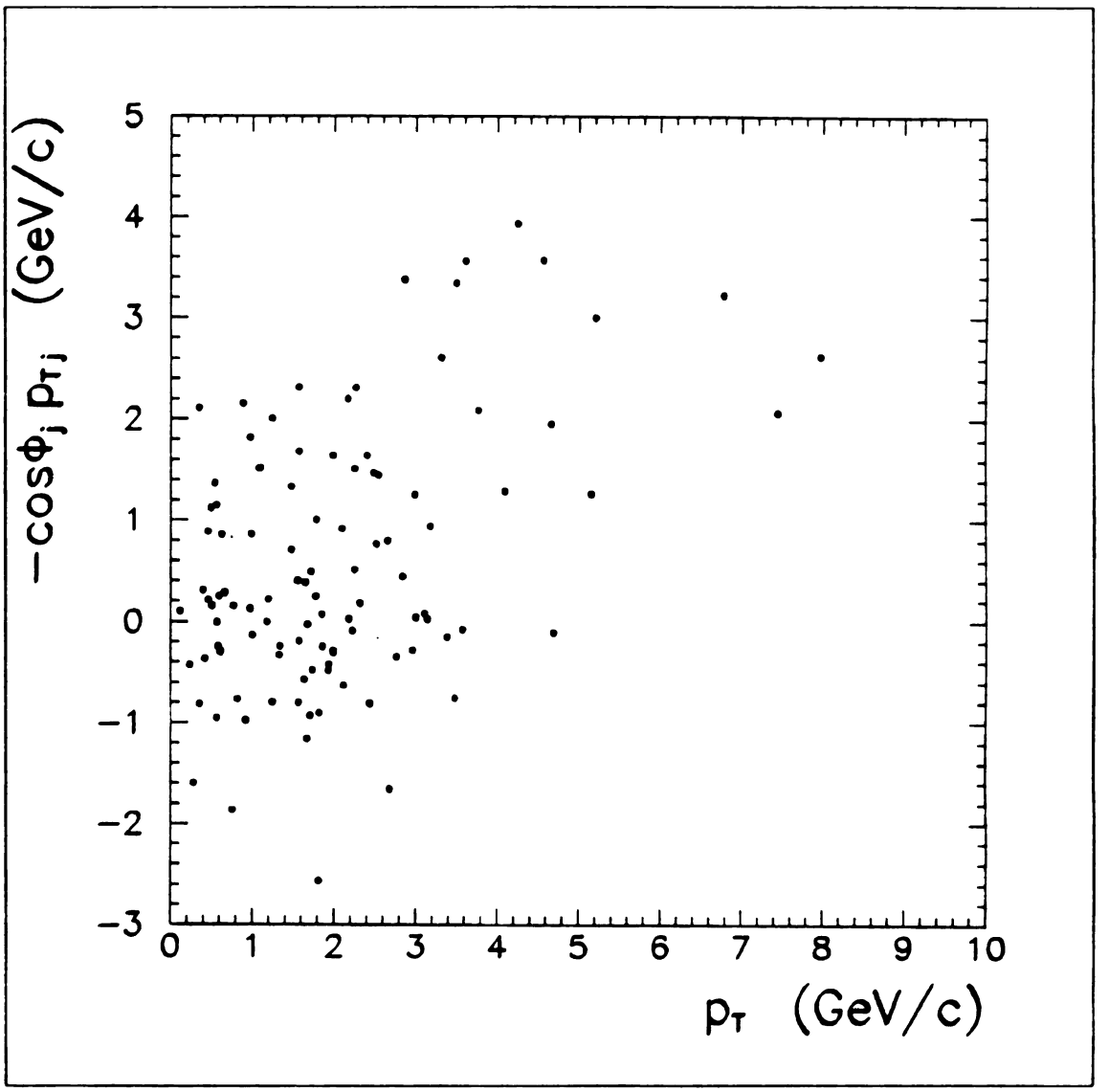

Figure 5.12: $-p_{Tj}\cos\Phi$ versus p_T

The momentum of the associated particles projected onto the transverse momentum of the electron pair versus the the transverse momentum of the electron pair.

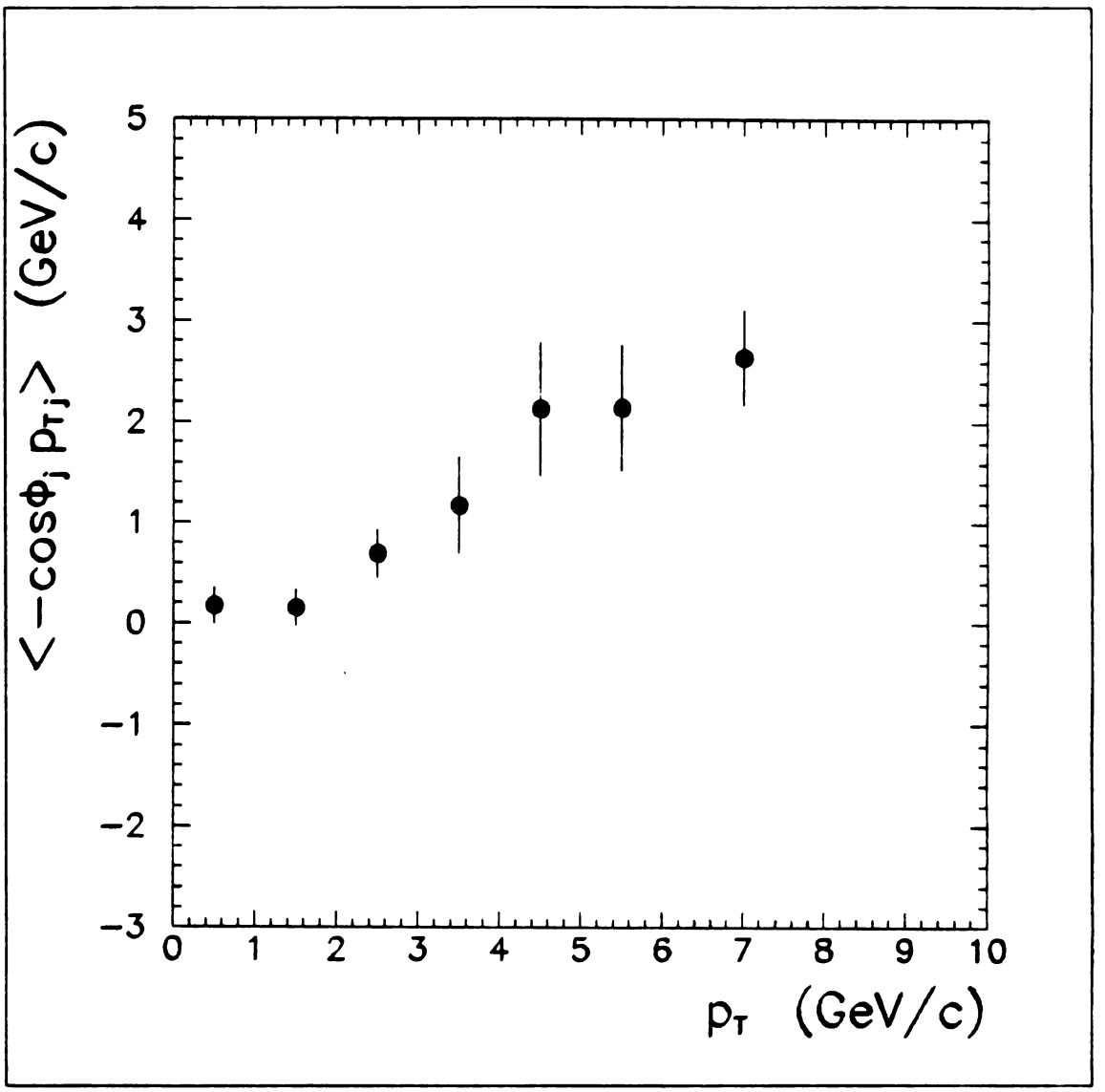

Figure 5.13: $\langle -p_{Tj} \cos\Phi \rangle$ as a function of p_T

The mean of the momentum of the associated particles projected onto the transverse momentum of the electron pair as a function of the transverse momentum of the electron pair.

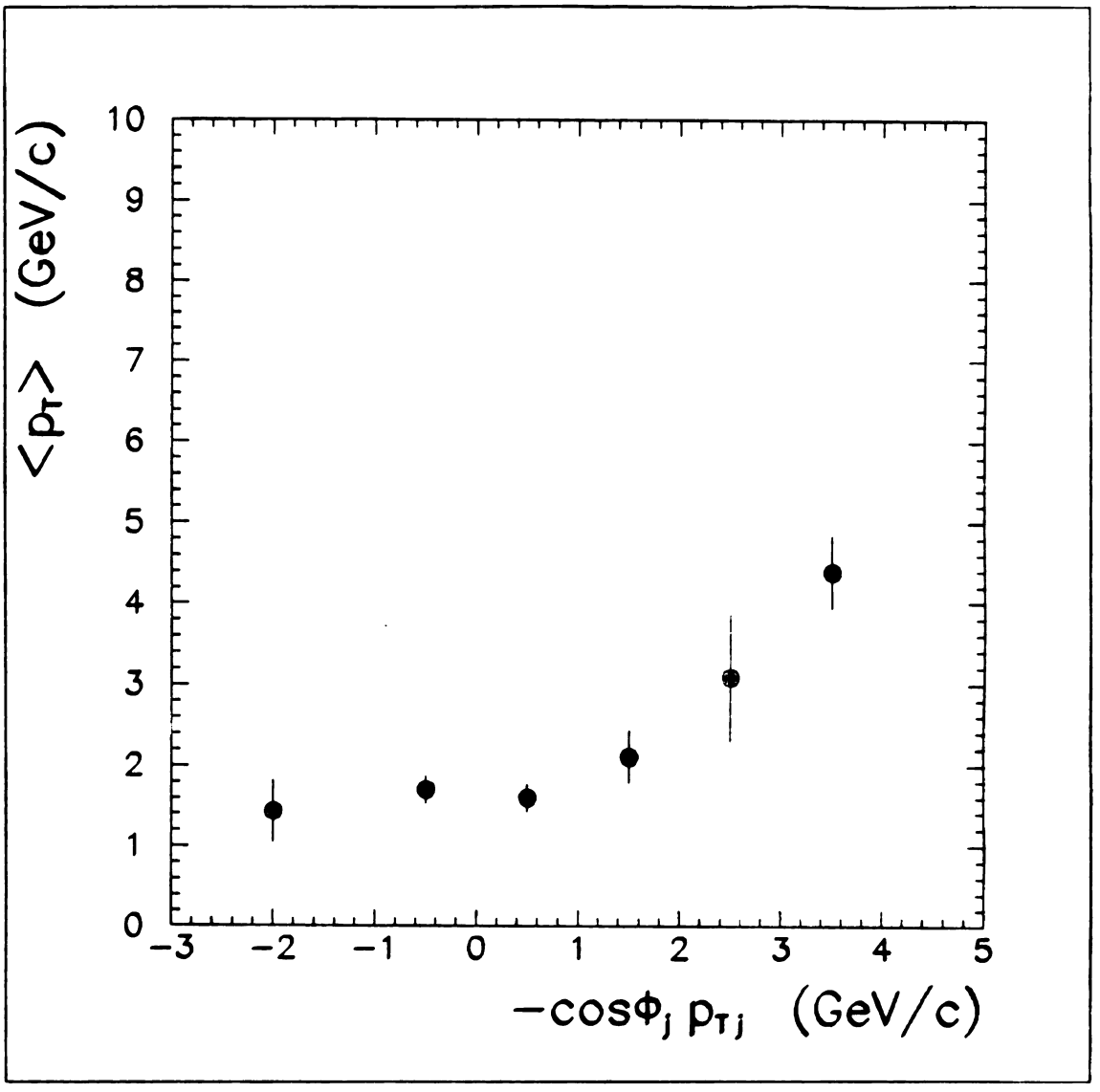

Figure 5.14: $\langle p_T \rangle$ as a function of $-p_{Tj} \cos \Phi$

The mean transverse momentum of the electron pair as a function of the transverse momentum of the associated particles.

able $\langle -p_{Tj} \cos \Phi_j \rangle$ the contribution from the spectator particles should sum to zero. Figure 5.13 shows this variable, the projection of the "jet" transverse momentum in the direction opposite to that of the electron pair, as a function of p_T and, indeed, more convincing evidence of a recoil jet is exhibited. Figure 5.14 shows the mean transverse momentum of the electron pair as a function of $-p_{T_j} \cos \Phi_j$. It can be seen that for values of $-p_{T_j} \cos \Phi_j$ below zero, little or no correlation exits. But above zero a strong correlation can be seen.

5.3 Charge Ratio

There is some question as to which of the two higher order diagrams (figure 1.2) contribute most. An answer to this question could be provided with an accurate measurement of the charge ratio of particles in the away side jet. Events arising through figure 1.2)b would be initiated by a gluon. The charge ratio of particles from a gluon jet is expected to be one.

For the figure 1.2)c the jet would be initiated by a quark. The rate at which this quark is a u quark compared to a d quark, for proton-proton collisions, will be approximately

$$\frac{N_u(q_u\alpha)^2}{N_d(q_d\alpha)^2} = 2\frac{(2/3)^2}{(1/3)^2} = 8.$$

For this quark jet one might naively expect this same ratio in the positive to negative hadrons on the away side. But since u quarks can give rise to negative hadrons and d quarks to positive hadrons the ratio can be much less. One could hope that the ratio of leading hadrons, which might remember the charge of the parent proton, would approach this ratio.

Figure 5.15 shows the ratio of positive to negative hadrons as a function of z, where

$$z = \left| \frac{p_{track} \cdot p_\gamma}{p_\gamma^2} \right|$$

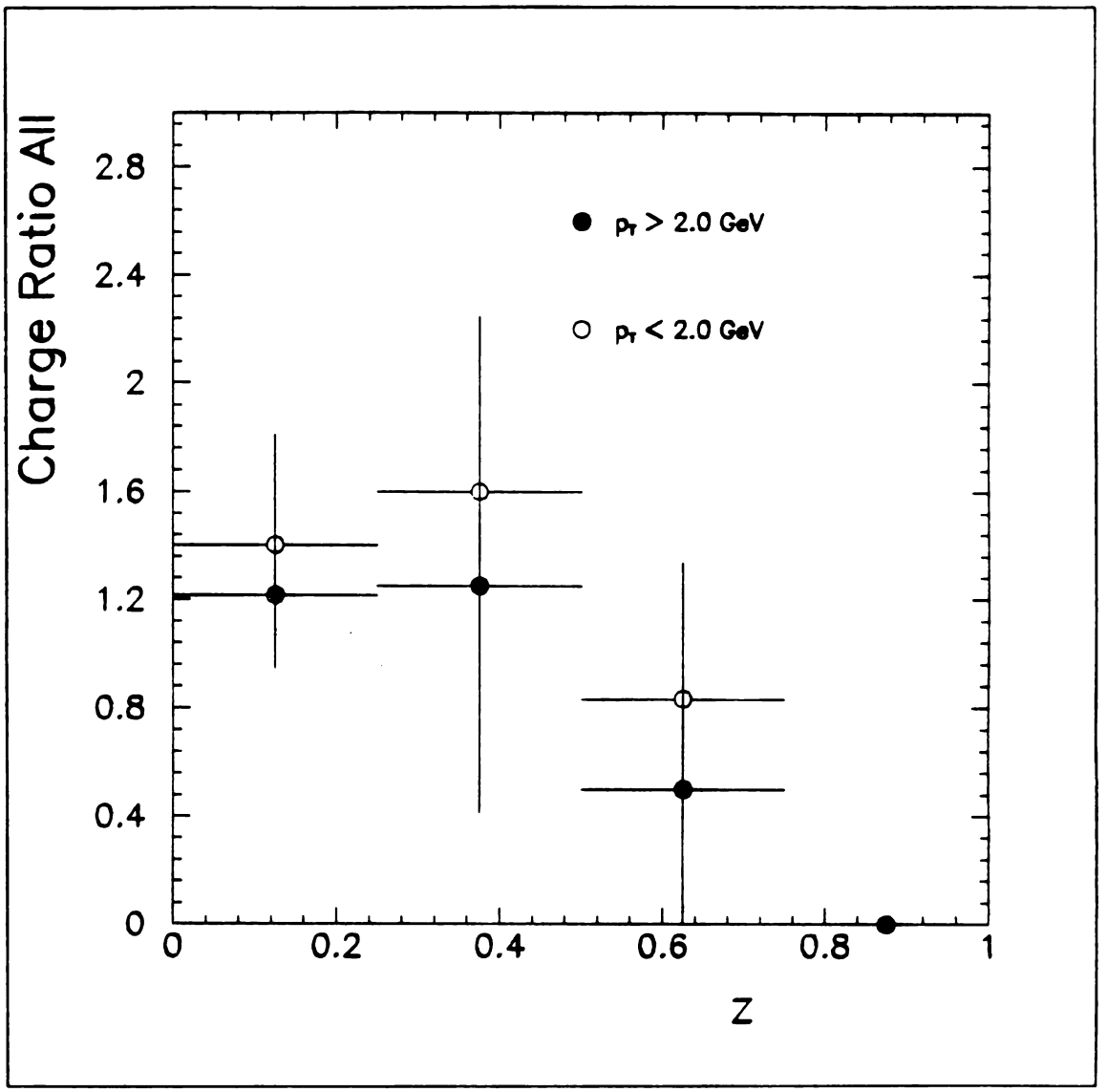

Figure 5.15: Charge Ratio
The charge ratio of the associated particles is shown as a function z.

Another source of hadrons in an event were the beam jets. Since the charge ratio of these hadrons should be near one it is difficult to distinguish whether the charge ratio of one is due to the gluon initiated jet or merely the result of spectator particles.

APPENDIX

Appendix A

Changes

A number of changes have been made that affect the cross section in this analysis since this experiment's last publications [23] [29] [1]. concerning electron pairs. A list of these changes is given below. Since most of these changes occurred in the Monte Carlo, the estimate of the efficiency of the detector as a function of mass is shown for the earlier publication along with the current estimate of the efficiency.

- Changes that affect the cross-section

    1. The Monte Carlo now includes the resonances from the Υ which raise the efficiency of the lowest mass bin and thus lower the cross section. For details see sections 4.1 and 4.1.1.

    2. The distribution thrown for the virtual photon in the Monte Carlo of the previous publication was flat in rapidity and had a mass distribution proportional to m^{-5}. The distribution is now thrown according to Duke and Owens structure functions as described in section 4.1.1. Because the structure functions restrict the rapidity range of the photons as the mass increases, the efficiency of detection increases.

    3. In both the previous and the current Monte Carlo the decay of the photon into the lepton pair was according to an angular distribution in θ of $1 +$

[1] These two papers were published based on the data included in the first two columns of tables 3.1 and 3.2

$\cos^2\theta$. But the previous definition of θ was the angle between the γ and the electron in the beam-beam center-of-mass. The current (and conventional) definition of θ or θ_{CS} is the angle between z_{CS} axis and the electron in the rest frame of the γ where z_{CS} is half way between the two beam axes. See section 4.1.1 for more detail.

4. The previous Monte Carlo required the track of an electron to extend out the back of the shower counters and not out the sides. The current Monte Carlo requires only that the electron track pass through at least $13cm$ of the shower counter. This condition has been added to the data. The results in a cross section that is 8% lower.

5. No corrections were made for energy leakage from the shower counters in the previous Monte Carlo. The current Monte Carlo takes into this leakage during calibration and running. Since there was overall more leakage during the calibration of the shower counters than when collecting data [2] the resulting cross section was lower.

6. Previously there was no modeling of the drift chambers in the Monte Carlo. Instead a correction was made based on the efficiency of two tracks passing through 8 planes in the drift chambers. It was later discovered that tracks at the ϕ edge of sextants, particularly sextant edges at the top and bottom of the detector, had low efficiencies because they passed through less than 8 planes [3]. The current Monte Carlo finds the probability of a track being accepted by determining how many planes of the chamber it passed through. For greater detail see section 4.1.2.

7. No account was taken of the efficiency for matching the track to the cluster in z position. It was known that the efficiency of the signal plus background

[2] Calibration was done in a beam at normal incidence, the shortest path through the counters.
[3] At least 6 hits were required per track.

in the data was $\sim$ 70%. But it was not known what the efficiency of the signal alone was. Modeling of cluster formation in the Monte Carlo showed a similar efficiency of $\sim$ 70%. See section 4.1.4 for details.

8. Previously the estimate of opposite sign background events was taken as the sum of plus-plus events, n_{++}, and minus-minus events, n_{--}. But if the charge of a track in a background event did not depend on the charge of the other member in the pair the best estimate of the plus-minus background should have been

$$2\sqrt{n_{++}n_{--}}$$

(see section 3.2.7). This change had little significance in estimating the background of the data set after all cuts were made since the background is small. But it did change the estimates of the efficiency of the α and the p_J cut. A description of these cuts can be found in section 3.2.8 and section 3.2.8 with values of efficiencies found in table 3.3.

9. Since the cross section is no longer assumed to be flat in y, the cross section

$$\left.\frac{d\sigma}{dmdy}\right|_{\Delta y=2.4}^{y=0}$$

has to be corrected by the Monte Carlo to give the value of

$$\left.\frac{d\sigma}{dmdy}\right|_{\Delta y\to 0}^{y=0}$$

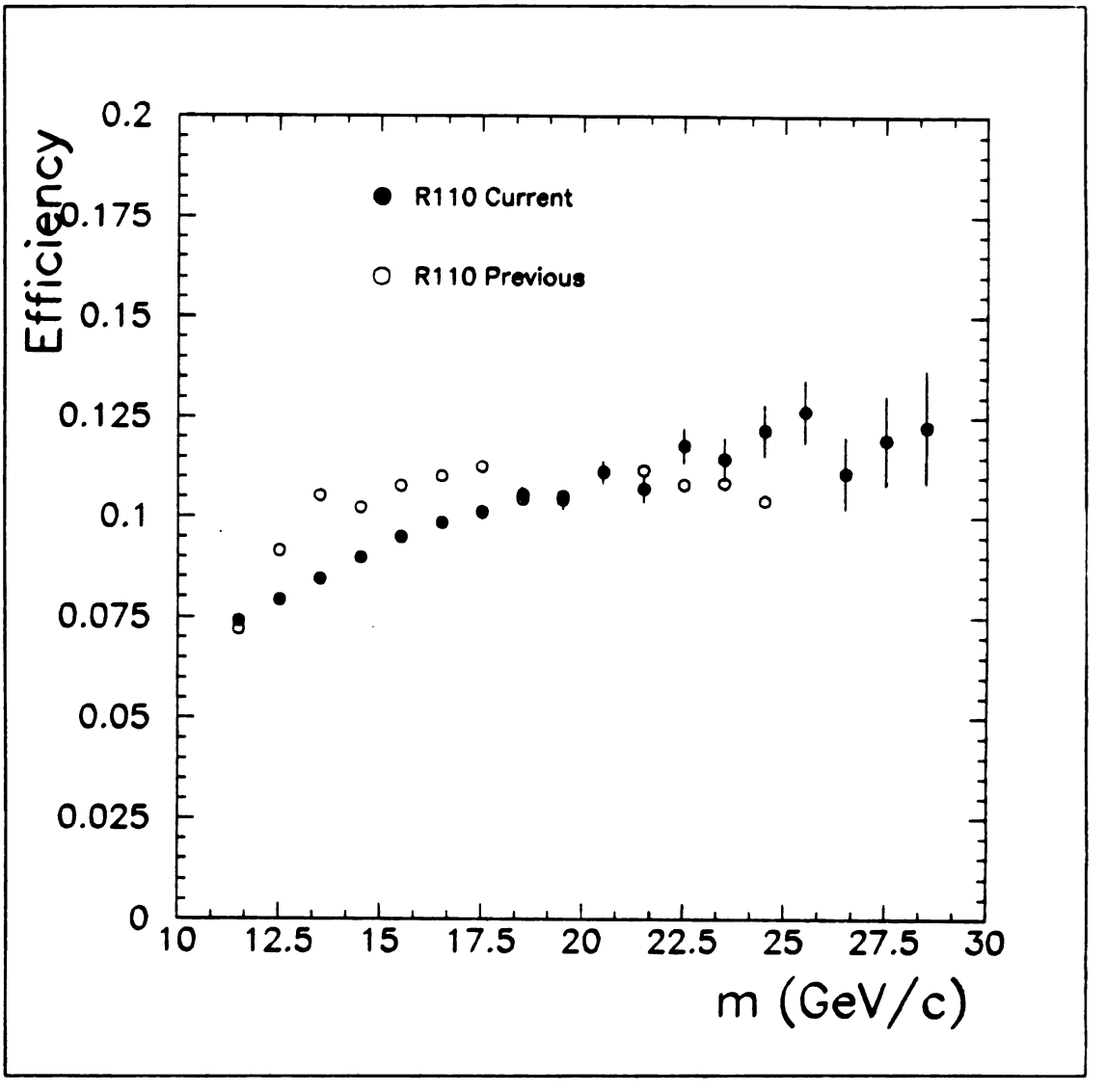

Figure A.1: Efficiency Changes

The distribution of the efficiency as a function of mass is shown for the previous publication and the current.

BIBLIOGRAPHY

Bibliography

[1] M. Gell-Mann. A Schematic Model of Baryons and Mesons . *Physics Letters*, 8:214, 1964.

[2] J. D. Bjorken. Asymptotic Sum Rules At Infinite Momentum . *Physical Review*, 179:1547, 1969.

[3] S. D. Drell and T. M. Yan. Massive Lepton-Pair Production in Hadron-Hadron Collisions at High Energies . *Physical Review Letters*, 25:316, 1970.

[4] J. H. Christenson et al. Observation of Muon Pairs in High-Energy Hadron Collisions . *Physical Review D*, 8:2016, 1973.

[5] J. C. Collins, D. E. Soper, and G. Sternman. All-Order Factorization for Drell-Yan Cross Sections . *Physics Letters*, 134B:263, 1984.

[6] G. Altarelli, R. K. Ellis, and G. Martinelli. Large Perturbative Corrctions to the Drell-Yan Process in QCD . *Nuclear Physics*, 157B:461, 1979.

[7] G. Altarelli, R. K. Ellis, M. Greco, and G. Martinelli. Vector Boson Production at Colliders: A Theoretical Reappraisal . *Nuclear Physics*, 246B:12, 1984.

[8] G. Altarelli, R. K. Ellis, and G. Martinelli. Lepton Pair Production at ISR Energies and QCD . *Physics Letters*, 151B:457, 1985.

[9] S. Van der Meer. Calibration of the Effective Beam Height in the ISR . *CERN Divisional Report ISR-PO/68-31*, 1968.

[10] Richard B. Nickerson. *A Shower Counter Study of Neutral Pair Events at the ISR* . PhD thesis, Oxford University, 1982.

[11] Carlos Walter Salgado-Galeazzi. *A Study of Direct Photon Production at the CERN Intersecting Storage Rings* . PhD thesis, Michigan State University, 1988.

[12] D. Antreasyan et al. Measurement of Dimuon Production at $s^{1/2} = 62$GeV . *Physical Review Letters*, 45:863, 1980.

[13] D. Antreasyan et al. Production Dynamics of High-Mass Muon Pairs . *Physical Review Letters*, 47:12, 1981.

[14] C. Kourkoumelis et al. Characteristics of J/Ψ and Υ Production at the CERN Intersecting Storage Rings . *Physics Letters*, 91B:481, 1980.

[15] D. W. Duke and J. F. Owens. Q^2-dependence Parameterizations of Parton Distribution Functions . *Physical Review*, 30:49, 1984.

[16] A. S. Ito. Measurement of the Continuum of Dimuons Produced in High-Energy Proton-Nucleus Collisions . *Physical Review D*, 23:604, 1981.

[17] J. C. Collins and D. E. Soper. Angular Distribution of Dileptons in High-Energy Hadron Collisions . *Physical Review D*, 16:2219, 1977.

[18] U. Amaldi. Fluctuations in Calorimetry Measurements . *Physica Scripta*, 23:409, 1981.

[19] E. Longo and I. Sestili. Monte Carlo Calculation of Photon-Initiated Electromagnetic Showers in Lead Glass . *Nuclear Instruments and Methods*, 128:283, 1975.

[20] A. L. S. Angelis et al. Jets in High Transverse Energy Events at the CERN Intersecting Storage Rings . *Nuclear Physics*, 244B:1, 1984.

[21] C. Kourkoumelis et al. Study of Massive Electron Pair Production at the CERN Intersecting Storage Rings . *Physics Letters*, 91B:475, 1980.

[22] A. L. S. Angelis et al. A Measurement of the Production of Massive e^+e^- Pairs in Proton-Proton Collisions at $\sqrt{s} = 62.4$GeV . *Physics Letters*, 87B:398, 1979.

[23] A. L. S. Angelis. A Study of e^+e^- Pairs in the Mass Range 11 to 25 GeV/c^2 at the CERN Intersecting Storage Rings . *Physics Letters*, 147B:472, 1984.

[24] *Transverse momentum behavior of dimuons produced by 39.5 GeV/c hadrons incident on a tungsten target and comparsion with higher energy results*, July 1981. Paper submitted to Intern. Conf. on High energy physics at Lisbon.

[25] R. L. Ford and W. R. Nelson. The EGS Code System: Computer Programs for the Monte Carlo Simulation of Electromagnetic Cascade Showers . Technical report, Stanford Linear Accelerator Center, June 1978.

[26] R. Jakeways and I. R. Calder. An Experimental Study of the Longitudinal Developement of Electron Initiated Cascades in Lead in the Energy Range. *Nuclear Instruments and Methods*, 84:79, 1970.

[27] D. Müller. Electron Showers of High Primary Energy in Lead . *Physical Review*, 5:2677, 1972.

[28] D. Antreasyan et al. Associated Hadronic Production in μ-Pair Events at the CERN Intersecting Storage Rings . *Nuclear Physics*, 199B:365, 1982.

[29] A. L. S. Angelis et al. A Study of Associated Particles and Second-Order Processes in Electron-Pair Production at the CERN Intersecting Storage. *Physics Letters*, 147B:477, 1984.